FORCE AND THERMAL EFFECTS ON ROTATING ABLATING BODIES

by

RAMIN TABIBZADEH
S.B., Massachusetts Institute of Technology (1987)

Submitted in partial fulfillment
of the requirements of the
degree of

MASTER OF SCIENCE
IN AERONAUTICS AND ASTRONAUTICS

at the

MASSACHUSETTS INSTITUTE OF TECHNOLOGY

January 1988

Signature of Author: _____
Department of Aeronautics and Astronautics, January 1988

Certified by: _____
Prof. Judson R. Baron
Thesis Supervisor, Prof. of Aeronautics and Astronautics

Accepted by: _____
Prof. Harold Y. Wachman
Chairman, Departmental Graduate Committee

Force and Thermal Effects on Rotating Ablating Bodies

by

Ramin Tabibzadeh

Submitted to the Department of Aeronautics
and Astronautics in January 1988
in partial fulfillment of the requirements for the
Degree of Master of
Science in Aeronautics and Astronautics

ABSTRACT

This thesis discusses force and thermal effects on rotating ablating bodies. Models are developed to describe mass ablation from an axi-symmetric body and thermal lag due to its rotation and ablation. These models are compared to data obtained by M.I.T. Lincoln Laboratory using an air bearing balance in the Ames 20-Megawatt Arc Jet tunnel. The method for reducing the data and some of the results are included in this report.

ACKNOWLEDGEMENTS

During my education at M.I.T., many have offered me their support and provided much encouragement. For those special friends too numerous to name individually, I offer this general but special thank you.

I would like to express my gratitude to Professor Judson R. Baron for numerous ideas, guidance, and support throughout the course of this thesis. From him I have learned not only many facts, but ways of thinking as well.

I extend deepest gratitude to both Dr. Charles W. Haldeman and Dr. Michael Judd of M.I.T. Lincoln Laboratory who provided guidance and counseling "beyond the call of duty" while supervising my work both as a summer student and graduate student.

Special thanks goes to past and present members of Lincoln Laboratory's Group 73, Aerospace Engineering, who contributed to this work both directly and indirectly. I would like to acknowledge M.I.T. Lincoln Laboratory for providing me with raw data obtained from their air bearing balance test at the Ames 20-Megawatt Arc Jet Facility. Deepest gratitude is extended to Mrs. Carole Kelly for typing this report.

Finally, I would like to thank my father, mother, and sister for their understanding, encouragement, and sacrifices without which this work would not have been possible.

Table of Contents

List of Figures

List of Figures (Continued)

List of Symbols

A	=	Area of tunnel cross-section
C	=	Capacitor
C_1, C_2	=	Integration constants
C_{mn}	=	Influence coefficient matrix
C_p	=	Specific heat at constant pressure
F_1	=	Normal force
F_2	=	Side force
F_N	=	Sum of normal forces
F_{No}	=	Aerodynamic normal force
F_{NB}	=	Ablation induced normal force, material "B"
F_{Ne}	=	Ablation induced normal force, epoxy
F_{Ng}	=	Ablation induced normal force, graphite
F_R	=	Resultant force
F_S	=	Sum of forces in side direction
F_{So}	=	Aerodynamic side force
F_{SB}	=	Ablation induced side force, material "B"
F_{Se}	=	Ablation induced side force, epoxy
F_{sg}	=	Ablation induced side force, epoxy
G	=	Conductor
H	=	Heat transfer coefficient
h	=	Height
ΔH_f	=	Heat of formation of material
k	=	Thermal conductivity
L	=	Reference length
M	=	Mach number
m	=	Mass loss rate

M_1	=	(in calibration data) = Pitching Moment
M_2	=	(in calibration data) = Yawing moment
M_1	=	(in m term) = constant, units in/s
M_2	=	(in m term) = constant, units 1/°R
m_e	=	Erosion mass loss rate
m_{tc}	=	Thermochemical mass loss rate
P	=	Pressure
P_e	=	Boundary layer edge pressure
P_r	=	Prandtl number
ΔP_n	=	Difference for pressure taps n
Q	=	Heat flux
q	=	Energy flux
Q^*	=	$\frac{k^* T^*}{L}$
Q_1^*	=	$\rho^* u^* A \Delta H_f^*$
Q_o	=	Heat flux at zero angle of attack
Q_{cw}	=	Cold wall heat flux
q_e	=	Erosion energy flux
r	=	Radius
s	=	Surface recession rate
T	=	Temperature
t	=	Time
T_1	=	Temperature due to constant heat flux at zero angle of attack
T_{aw}	=	Adiabatic wall temperature
T_c	=	Temperature of inner surface
T_e	=	Boundary layer edge temperature
T_i	=	Initial temperature
T_o	=	Temperature at x = 0
	=	Stagnation temperature

T_r	=	Recovery temperature
$T_{surface}$	=	Total surface temperature, $T_1(h) + \Delta T_1(x, h)$
T_w	=	Wall temperature
ΔT_1	=	Temperature rise due to sinusoidal heat flux term
ΔT_{1max}	=	Maximum surface temperature perturbation
u	=	Velocity
u^*	=	ωr
u_e	=	Boundary layer edge velocity
Y_1	=	Non-dimensional heating term
Y_2	=	Non-dimensional mass ablation term
Y_3	=	Non-dimensional radiation term.
Z_1	=	See equation (10)
Z_2	=	See equation (11)
α	=	Thermal diffusivity
γ	=	Specific heat ratio
ε	=	Empirical parameter relating to heating distribution to angle of attack Also an error in pressure reading due to leak (equations (64) and 65))
ε_w	=	Surface emissivity
θ	=	Angular coordinate
$\theta_{T.L.}$	=	Thermal lag angle
λ	=	Parameter defined in equation (20)
μ	=	Viscosity
ρ	=	Density
ρ_e	=	Boundary layer edge density
σ	=	Stefan - Boltzman constant
ϕ	=	Angle from windward ray of resultant force
ψ	=	Cone half angle
ω	=	Angular velocity of cone
Ω	=	Nondimensional spin rate parameter, $\frac{\omega r^2}{\alpha}$

Subscripts

abl	=	Ablation term
chem	=	Chemical term
cond	=	Conduction term
conv	=	Convection term
rad	=	Radiation term
∞	=	Free stream condition

Superscript

—	=	Non-dimensional quantity
*	=	Reference quantity
'	=	Derivative with respect to T

Chapter 1

Introduction

For years, aerodynamic forces on bodies in high-speed flight have been a matter of concern. In order to understand, model, and predict the aerodynamics of meteorites and man-made vehicles as they passed through the high-altitude regime, the earliest researchers applied Newtonian methods.[1] The desire for increased accuracy in predicting high-speed flight performance led to the development of more complex techniques, such as applying continuum theory to satellite and hypersonic flight problems.[2,3]

As the scientific/engineering community applauded the success of early unmanned and manned reentry flights, it recognized the emergence of ablation as a means of thermal protection.[4,5,6,7] These successes intensified the research efforts which over the years advanced the analytical tools from the relatively simple "heat of ablation" approach[8] to more sophisticated computer codes which allowed a detailed description of the ablation processes.[9,10,11,12]

Parallel with the ablation investigations, papers were written to study the complex aerodynamic effects caused by ablation both in ground and flight experiments.[13,14,15] These papers on the effects of geometric asymmetry and ablation of the protective skin had been largely concerned with the complex forces measured.

In attempting to resolve these forces, researchers were faced with the problems of finding a solution to the boundary layer of bodies in high-speed atmospheric flight, explaining thermodynamic effects under those conditions and analyzing material ablation and resultant momentum flux off the body. To complicate matters even further, engineering applications required these non-linear problems to be studied for spinning re-entry bodies and rotating rocket nozzles. This research was in large begun due to a flight test involving two English Black Knight re-entry vehicles (R.V.'s), where the first signs of anomaly were present. One of the R.V.'s was painted with an ablative material and, upon flight, experienced a dynamic instability. The second non-ablating R.V. exhibited

no dynamic effects under the same conditions where the first experienced the instabilities. The results could only be described by introducing a Magnus-like term[16] in the equations of motion. This term is a result of the interaction between aerodynamic heating and thermal conduction in the body.[17]

As of today, no one can affirm that they have solved the boundary layer solution to the problem at hand, although progress has been made in developing sophisticated codes to solve the Navier-Stokes equations. This thesis does not examine the boundary layer; however it attempts to model the thermodynamic and ablation effects in a simplified way on a rotating body at high-speed and to investigate the interaction between the aerodynamic heating, ablation, and thermal conduction for a rotating body.

Define the thermal-lag angle as the angle from the windward ray (in the direction of rotation) at which the highest surface temperature is found. As the windward side of an ablating body experiences a temperature sufficient to induce mass loss, a finite period of time is required for the material to respond and eject mass. In the case of a non-spinning body at angle of attack, this mass ejection causes an ablation force in the normal direction[17] which does not displace the thermal-lag angle as the peak rate of ablation occurs at the windward ray. In the case of a spinning vehicle, however, the ablation force is displaced to one side of the plane of symmetry, corresponding to a non-vanishing thermal-lag angle. The side with the higher mass addition has a thicker boundary layer. This boundary layer asymmetry produces a corresponding pressure differential and moment. The problem is to determine their magnitude.

The thermal-lag problem has been examined using both a steady-state simplification of a transient analytical model and a transient computational one. The computational model only includes the effects of the aerodynamic heating and thermal conduction, whereas the analytical model also includes ablation and radiation from the body. Thus the interaction between the spin rate of the body, the thermal diffusivity of the protection skin and the lag may be investigated.

By reducing and analyzing arc jet force data obtained by M.I.T. Lincoln Laboratory for several different ablating materials, an experimental thermal lag is calculated. The result has been compared to those obtained from the analytical and computational models.

In addition the mass loss from the heat shield materials in the arc jet has been compared to a theoretical model. Laminar-flow on a sharp cone undergoing steady-state ablation at the surface was assumed, an assumption which does not correspond well to the experimental conditions.

Chapter 2

Thermal Lag

In past years problems dealing with forces due to ablation and rotation of bodies in high-speed atmospheric flight have been studied extensively. Nevertheless in attempting to resolve these forces, the thermodynamic effects at times have not been included completely. An example of that neglect are those effects that are induced due to the non-uniform heating of a vehicle (Figure 1).

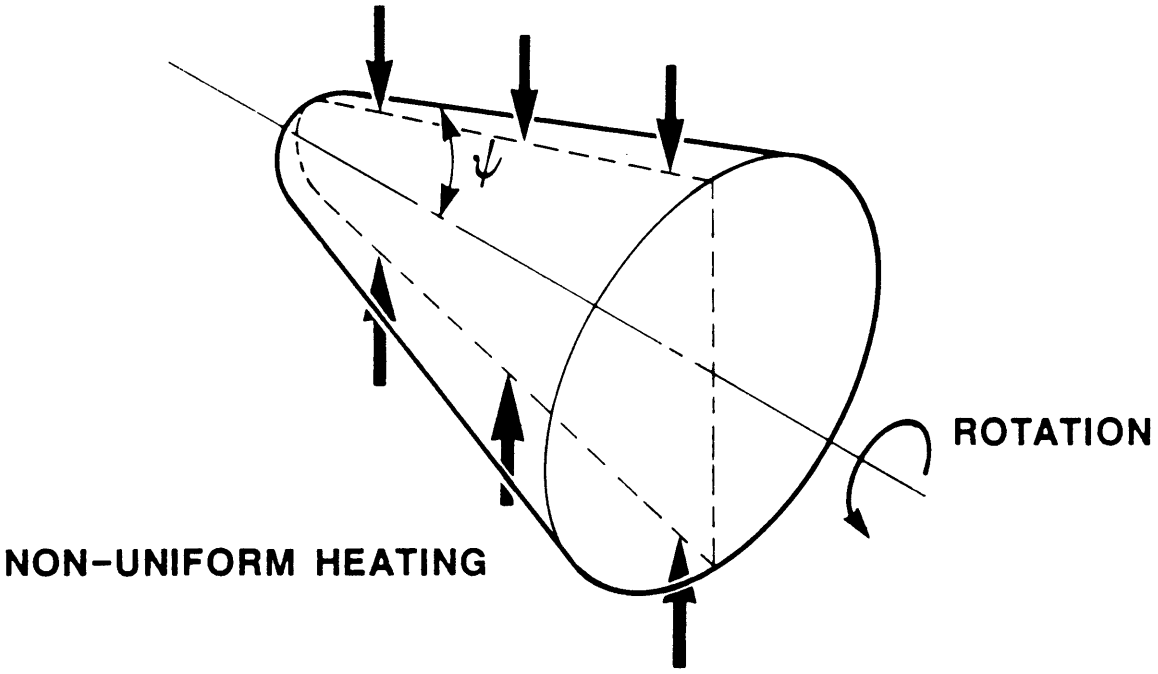

Figure 1. A rotating axi-symmetric body.

As the pitching ablating body is being heated, the windward side experiences a rise in temperature greater than that of the leeward. Consequently the former side undergoes a larger mass loss. For a spinning vehicle, this non-uniform heating rate will cause a similar temperature distribution on the body, but displaced through a lag angle. Define this thermal-lag angle ($\theta_{T.L.}$) as the angle from the windward ray (in the direction of

rotation) at which the highest surface temperature is found; for the non-rotating case $\theta_{T.L.}$ is equal to zero. In the case of a spinning vehicle, the peak rate of ablation (thus the highest surface temperature) is displaced to one side of the body from the plane of asymmetry.

The heating rate on the vehicle was modeled in order to evaluate the thermal-lag angle $\theta_{T.L.}$ for various rotational speeds and thermal properties of the body. Comparing the pressure distribution[17] around the body, a sinusoidal approximation for the heat transfer coefficient was chosen (see Appendix A). Designating Q_0 as the heat flux to a body at zero angle of attack, the heating rate distribution applied to the body was modeled by the equation (Figure 2)

$$Q(\theta) = Q_0(1 + \varepsilon \cos \theta) \quad ,$$

where ε is an empirical parameter relating the heating distribution to the angle of attack ($\varepsilon = 0$, $Q = Q_0$ at zero angle of attack), and θ is an angular coordinate. Appendix A describes how ε is modeled.

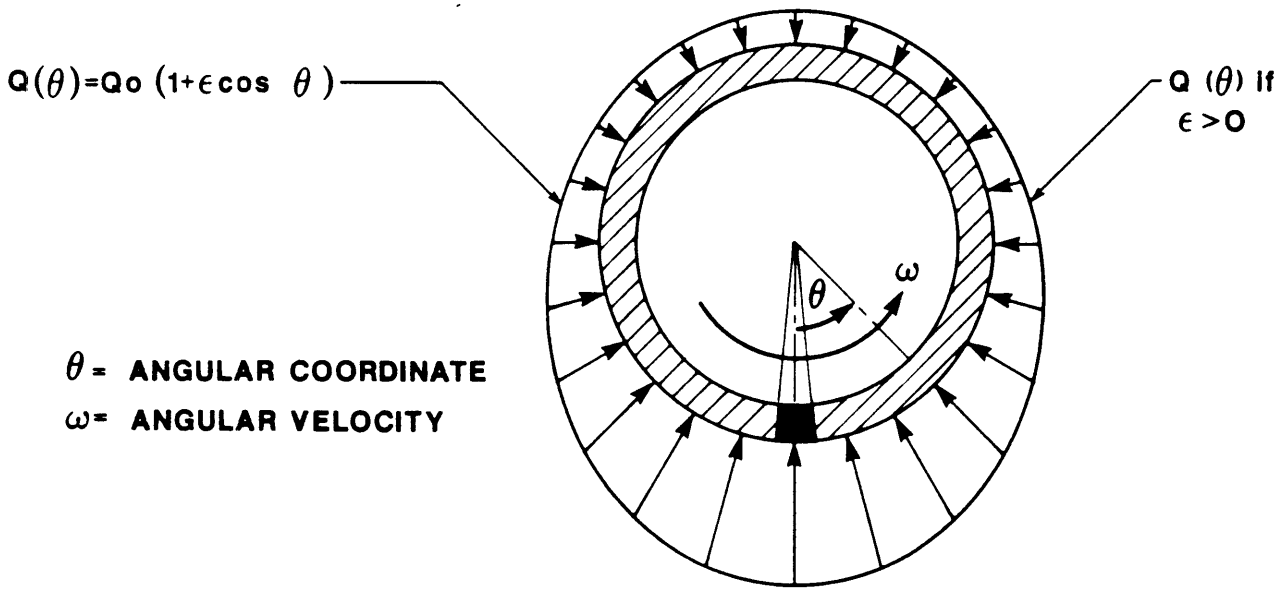

Figure 2. Heating on rotating body section.

In the next three sections this heating rate distribution is used in analytical and computational models to derive the relationship between thermal-lag angle, angular velocity of the body, and thermal properties of the material. The analytical and computational models differ in that the latter describes a transient problem in which all the heat input on the surface is conducted into the solid, whereas the former represents a steady-state simplification of a transient problem in which the heat input contributes to the conduction to, and ablation and radiation from the body.

a) THE ANALYTICAL ABLATION, CONDUCTION, AND RADIATION MODEL

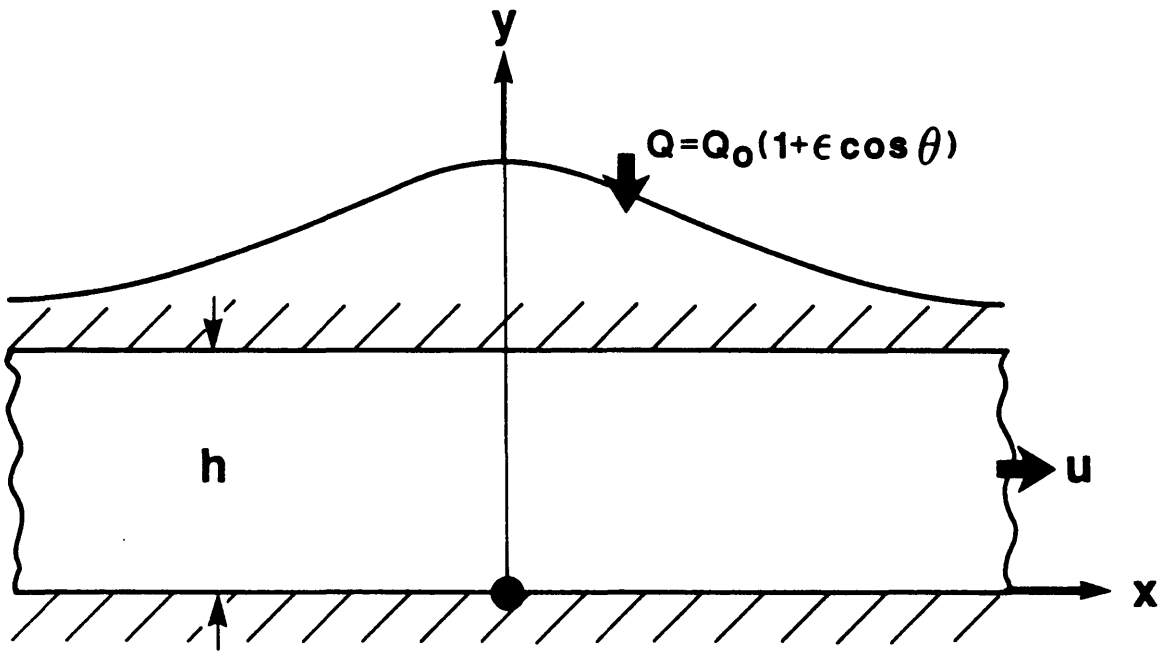

Figure 3. Heating on infinite-length slab of finite thickness.

In order to obtain an analytical solution to the thermal-lag problem, the axi-symmetrix body is unwound from its cylindrical form and modeled as an infinite slab of finite thickness, h, where h << r and r is the radius of the model. The rotation of the cylinder is simulated by allowing the slab to move with a velocity u ($u^* = \omega r$) in the positive x-direction. As the sinusoidal heating rate (Appendix A) on the axi-symmetric body is fixed, the heating on the model is stationary but periodic in x. The non-dimensional differential equation (1) describing the analytical model includes the reference thermal diffusivity ($\alpha^* = k/(\rho c_p)$), and reference velocity of the slab ($u^* = \omega r$) as basis for the normalization.

$$\left(\frac{\partial^2 \bar{T}}{\partial \bar{x}^2} + \frac{\partial^2 \bar{T}}{\partial \bar{y}^2}\right) = \frac{u^* L}{\alpha^*} \frac{\bar{u}}{\bar{\alpha}} \frac{\partial \bar{T}}{\partial \bar{x}} \quad , \tag{1}$$

taking

$$\bar{\alpha} = \frac{\alpha}{\alpha^*}, \ \bar{T} = \frac{T}{T^*}, \ \bar{x} = \frac{x}{L}, \ \bar{y} = \frac{y}{L}, \ \bar{u} = \frac{u}{u^*} \quad ,$$

where L is a reference length, equal to r, the outer radius of the original body. (Appendix B contains numerical values for all reference variables.) This non-dimensionalized equation is a steady-state simplification of the transient problem, as it has been assumed that

$\frac{\partial \bar{T}}{\partial \bar{t}} = 0$, where $\bar{t}$ is a non-dimensionalized time.

The model incorporates the angular velocity of the body, and the material of the heated surface. The boundary conditions in $\bar{y}$ that are applied to this problem consist of a constant temperature inner wall

$$\text{at} \quad \bar{y} = 0: \ \bar{T} = \frac{T_c}{T^*} \tag{2}$$

(T_c = temperature of inner surface), and an energy balance at the surface

$$\bar{y} = \bar{h}: \ \bar{Q}_o\left(1 + \varepsilon e^{i\bar{x}}\right) = \bar{Q}_{cond} + \bar{Q}_{abl} + \bar{Q}_{rad} \tag{3}$$

(the real part of $e^{i\bar{x}}$ is used in the solution). The non-dimensional terms are defined as

$$\bar{Q}_o = \frac{Q_o}{Q^*} = \text{Heat flux on surface at zero angle of attack,}$$

$$\bar{Q}_{cond} = \frac{Q_{cond}}{Q^*} = \text{Heat flux conducted into material,}$$

$$\bar{Q}_{rad} = \frac{Q_{rad}}{Q^*} = \text{Heat flux radiated off surface,}$$

and

$$\bar{Q}_{abl} = \frac{Q_{abl}}{Q^*} = \text{Heat flux used in ablating material,}$$

where the reference heat flux Q* is $\frac{k^* T^*}{L}$. k* is the reference material thermal conductivity and T* is a reference ablation temperature. The two boundary conditions in $\bar{x}$ are inherent in the model as it is assumed that the heat flux on the slab is of a sinusoidal nature and that the effect of this heating is repetitive. Thus the temperature through the slab at a particular $\bar{x}$ is the same as its temperature one "wavelength" away.

Rewriting equation (3),

$$\bar{Q}_o \left(1 + \varepsilon e^{i\bar{x}}\right) = \bar{k} \frac{\partial \bar{T}}{\partial \bar{y}} + \overline{\Delta H_f}\, \bar{m} + \sigma \bar{\varepsilon}_w \left(\bar{T}\right)^4 \quad , \tag{4}$$

where σ is the Stefan-Boltzman constant and the non-dimensionalized terms are defined as

$\bar{k} = \frac{k}{k^*}$ = thermal conductivity of material, non-dimensional,

$\overline{\Delta H_f} = \frac{\Delta H_f}{\Delta H_f}$ = heat of formation of material, non-dimensional,

$\bar{m} = \frac{m}{m^*}$ = ablation rate as a function of temperature, non-dimensional,

$\bar{\varepsilon}_w = \frac{\varepsilon_w}{\varepsilon_w^*}$ = surface emissivity, non-dimensional.

ε_w* is the reference material emissivity at room temperature. The temperature ($\bar{T}$) can be separated into two terms. The first may be considered to be the temperature due to the constant heat flux at zero angle of attack ($\bar{Q}_o$), whereas the second may be the temperature due to the sinusoidal contribution ($\bar{Q}_o \varepsilon e^{i\bar{x}}$).

$$\bar{T} = \bar{T}_1 + \overline{\Delta T_1} \quad . \tag{5}$$

It is assumed in our model that the temperature rise due to the sinusoidal heat flux is small compared to the constant temperature term ($\overline{\Delta T_1} << \overline{T_1}$). $\overline{T_1}$ only varies with $\bar{y}$, while $\overline{\Delta T_1}$ varies both along the length and thickness of the slab.

$$\bar{T} = \bar{T}_1(\bar{y}) + \Delta \bar{T}_1(\bar{x}, \bar{y}) \quad . \tag{6}$$

Using equation (6) and solving for the temperature at zero angle of attack ($\varepsilon = 0$),

$$\frac{\partial^2 \bar{T}_1}{\partial \bar{y}^2} = 0, \quad \frac{\partial \bar{T}_1}{\partial \bar{y}} = C_1, \quad \bar{T}_1 = C_1 \bar{y} + C_2 \quad . \tag{7}$$

Applying the two boundary conditions in equations (2) and (3),

$$\bar{T}_1 (0) = \frac{T_c}{T^*} = C_2 \quad , \tag{8}$$

and

$$\text{at} \quad \bar{y} = \bar{h}: \quad \bar{Q}_o = C_1 \bar{k} + Z_1 (\bar{T}_1) + Z_2 (\bar{T}_1) \quad , \tag{9}$$

$$\text{where} \quad Z_1 = \overline{\Delta H_f} \, \bar{m} \quad , \tag{10}$$

$$\text{and} \quad Z_2 = \sigma \bar{\varepsilon}_w (\bar{T}_1)^4 \quad . \tag{11}$$

The mass ablation rate is a function of the surface temperature and varies for different materials. In a report entitled "Development of the thermal/ablation model for a passive decoy epoxy material,[19]" the Acurex Corporation discussed tests conducted in stagnation arc facilities on epoxy test specimens to derive the surface recession rates and consequently mass ablation rate for epoxy. Although $\bar{T}$ as derived will in general apply for any material the results discussed in this section will be restricted to epoxy ($\alpha^* = 5.9 \times 10^{-5}$ in^2/s). The mass ablation rate of epoxy obtained from Reference 19 will be of the form

$$m = M_1 e^{(M_2 T)} \quad , \tag{12}$$

where ρ = density of epoxy (0.03302 lb m/in^3),

M_1 = 2.536 x 10^{-5} (in/s),

and M_2 = 0.0022387 (1/•R).

Assuming that this ablation rate is correct, an epoxy body may be modeled.

Using the surface boundary condition (9), the value for C_1 can be determined through iteration and thus $\overline{T}_1$ can be obtained.

$$\overline{T}_1 = C_1 \bar{y} + \overline{T}_1(0) \quad . \tag{13}$$

Figure 4 shows experimental data of the non-dimensional cold wall heat flux ($\overline{Q_{cw}}$) from Reference 19 versus non-dimensional ablation temperature. As heat flux is defined by

$$Q = H\left(T_{aw} - T_w\right) \quad , \tag{14}$$

where H = heat transfer coefficient,

T_{aw} = adiabatic wall temperature

and T_w = wall temperature,

cold wall heat flux for $T_{aw} >> T_w$ is[20]

$$Q_{cw} = H\, T_{aw} \quad . \tag{15}$$

The data from Reference 19 in Figure 4 is compared to values of $\overline{Q}_{cw}$ and $\overline{T}_1$ ablation obtained from equation (9) for a model including ablation, conduction and radiation and another model including only ablation and conduction ($Z_2(\overline{T}_1) = 0$). The justification for using the former is that at the $\overline{Q}_{cw}$ used to simulate M.I.T. Lincoln Laboratory's gas bearing balance test (discussed in Chapter 3), this model showed identical values to that of Acurex. At other $\overline{Q}_{cw}$ values agreement is poor. This lack of consistency could be due to either an oversimplified analytical model or inappropriate experimental results. Since the epoxy tested by Acurex was not prepared in the same laboratory or from the same base resin, it is possible that the behavior was different. It may be that the difference is mainly due to the oversimplification of the model. However since the $\overline{Q}_{cw}$ value used for the gas bearing balance test produced agreement with the stagnation arc test measurement the ablation, conduction, and radiation model will be used.

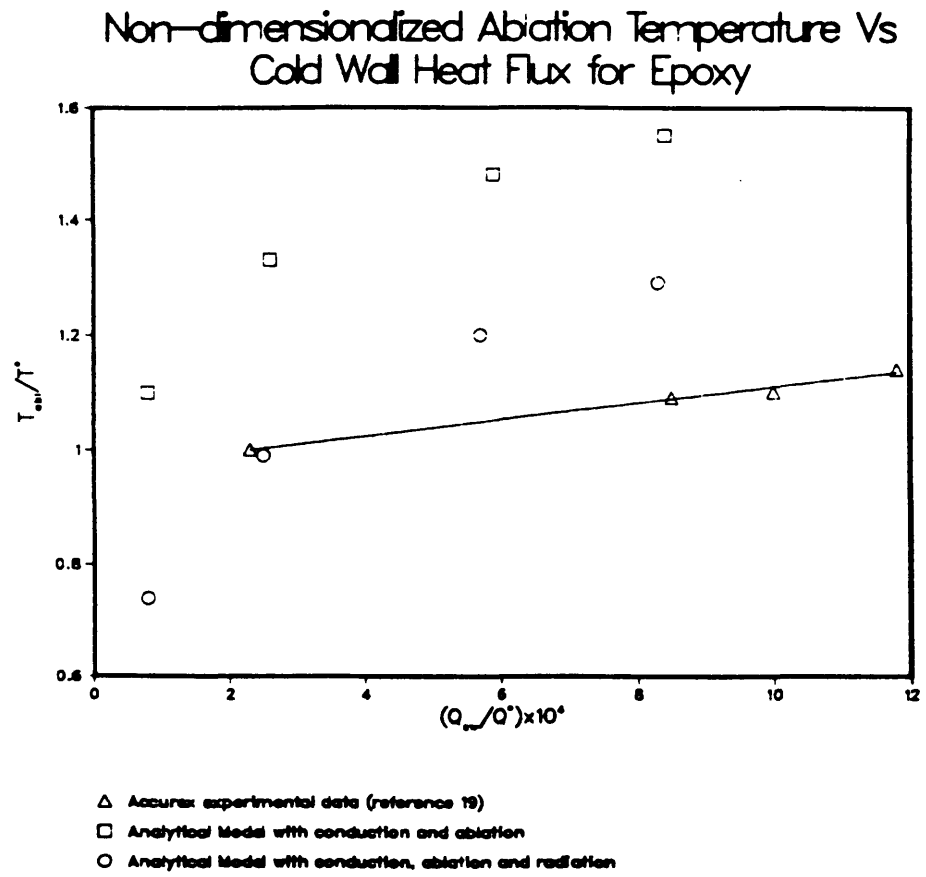

Figure 4. Non-dimensionalized cold wall heat flux versus ablation temperature, epoxy.

Having found $T_1(y)$, equation (1) and (6) can be solved for $\Delta\overline{T}_1(\overline{x},\overline{y})$, using a solution of the form

$$\Delta\overline{T}_1 = F(\overline{y})\, e^{i\overline{x}} \quad , \tag{16}$$

where F(y) is a complex term. The first and second derivatives of the solution are

$$\frac{\partial\overline{\Delta T}_1}{\partial\overline{x}} = F(\overline{y})\, ie^{i\overline{x}} \qquad \frac{\partial\overline{\Delta T}_1}{\partial\overline{y}} = F'(\overline{y})\, e^{i\overline{x}}$$

$$\frac{\partial^2\overline{\Delta T}_1}{\partial\overline{x}^2} = F(\overline{y})\, e^{i\overline{x}} \qquad \frac{\partial^2\overline{\Delta T}_1}{\partial\overline{y}^2} = F''(\overline{y})\, e^{i\overline{x}} \tag{17}$$

and substituting these into the differential equation (1), the following equation is obtained

$$\left(\overline{\Delta T}_{1\,\overline{xx}} + \overline{\Delta T}_{1\,\overline{yy}}\right) = \frac{\overline{u}}{\alpha}\,\Omega\,\overline{\Delta T}_{1\,\overline{x}} \quad , \tag{18}$$

where $\Omega = \frac{u^* L}{\alpha^*}$. After manipulation the latter becomes

$$F''(\bar{y}) - \lambda F(\bar{y}) = 0 \quad , \tag{19}$$

$$\text{where } \lambda = \sqrt{1 + i \frac{\bar{u}}{\bar{a}} \Omega} \quad . \tag{20}$$

Then F is of the form[21]

$$F = A e^{\lambda \bar{y}} + B e^{-\lambda \bar{y}} \quad . \tag{21}$$

Using the boundary conditions (2) and (3)

$$\text{at} \qquad \bar{y} = 0: \ \overline{\Delta T_1} = 0, \ F(0) = 0, \ \text{thus } A = -B \tag{22}$$

and at $\bar{y}=\bar{h}$,

$$\bar{Q}_o \left(1 + \varepsilon e^{i\bar{x}}\right) = \bar{k} \left(A \lambda \left[e^{\lambda \bar{h}} + e^{-\lambda \bar{h}}\right] e^{i\bar{x}} + \partial \bar{T}_1 / \partial \bar{y}\right)$$

$$+ Z_2 \left(\bar{T}_1 + \overline{\Delta T_1}\right) + Z_3 \left(\bar{T}_1 + \overline{\Delta T_1}\right) \quad . \tag{23}$$

Linearizing $\bar{m}(\bar{T}_1 + \Delta \bar{T}_1)$ and $\bar{m}(\bar{T}_1 + \Delta \bar{T}_1)^4$, assuming $\Delta \bar{T}_1 << \bar{T}_1$,

$$\bar{m} \left(\bar{T}_1 + \Delta \bar{T}_1\right) \simeq m \left(\bar{T}_1\right) + \Delta \bar{T}_1 \frac{d\bar{m}}{dT} \Big|_{\bar{T}_1} \tag{24}$$

$$\text{and } \left(\bar{T}_1 + \Delta \bar{T}_1\right)^4 \simeq \bar{T}_1^4 \left(1 + \frac{4 \Delta \bar{T}_1}{\bar{T}_1}\right) \quad . \tag{25}$$

Substituting the linearized forms into (21) and substituting (9),

$$\bar{Q}_o \varepsilon e^{i\bar{x}} = \bar{k} A \lambda \left[e^{\lambda \bar{h}} + e^{-\lambda \bar{h}}\right] e^{i\bar{x}}$$
$$+ \Delta \bar{H}_f \Delta \bar{T}_1 \frac{d\bar{m}}{dT} \Big|_{\bar{T}_1}$$
$$+ \sigma \bar{\varepsilon}_w 4 \Delta \bar{T}_1 \left(\bar{T}_1\right)^3 \quad . \tag{26}$$

Letting

$$Q^* = \frac{K^* T^*}{L} \quad , \tag{27}$$

$$\overline{\Delta T_1} = A\left(e^{\lambda \bar{h}} - e^{-\lambda \bar{h}}\right) \quad , \tag{28}$$

$$Y_1 = \bar{Q}_o \, \varepsilon \quad , \tag{29}$$

$$Y_2 = \frac{\overline{\Delta H_F} \, \frac{d\bar{m}}{dT} \Big|_{T_1}}{Q^*} \quad , \tag{30}$$

$$Y_3 = \frac{\sigma \bar{\varepsilon}_w \left(\bar{T}_1\right)^3}{Q^*} \quad , \tag{31}$$

and solving for A,

$$A = \frac{Y_1}{\lambda\left[e^{\lambda \bar{h}} + e^{-\lambda \bar{h}}\right] + \left(Y_2 + 4Y_3\right)\left(e^{\lambda \bar{h}} - e^{-\lambda \bar{h}}\right)} = -B \quad . \tag{32}$$

Having found the expressions for A and B, the solution for the surface temperature perturbation due to sinusoidal heating solution can be written as

$$\overline{\Delta T_1}\left(\bar{x}, \bar{h}\right) = \frac{Y_1 e^{i\bar{x}}}{\frac{\lambda\left(e^{\lambda \bar{h}} + e^{-\lambda \bar{h}}\right)}{\left(e^{\lambda \bar{h}} - e^{-\lambda \bar{h}}\right)} + \left(Y_2 + 4Y_3\right)} \quad . \tag{33}$$

Obtaining the thermal lag ($\theta_{T.L.}$) and the amplitude of the temperature $|\overline{T}|$ from this equation

$$\theta_{T.L.} = -\tan^{-1}\left[\frac{\mathrm{Im}\,\Delta\bar{T}_1\left(\bar{x}, \bar{h}\right)}{\mathrm{Re}\,\Delta\bar{T}_1\left(\bar{x}, \bar{h}\right)}\right] \tag{34}$$

(positive in the direction of spin),

$$\text{and } \bar{T} = \left| \sqrt{\text{Re}\left(\Delta\bar{T}_1\right)^2 + \text{Im}\left(\Delta\bar{T}_1\right)^2} \right| + \bar{T}_1 \quad . \tag{35}$$

Letting

$$e^{\lambda\bar{h}} + e^{-\lambda\bar{h}} = N_1 + iN_2 \quad , \tag{36}$$

$$e^{\lambda\bar{h}} - e^{-\lambda\bar{h}} = D_1 + iD_2 \quad , \tag{37}$$

and

$$Y_4 = Y_2 + 4Y_3 \quad , \tag{38}$$

equation (33) becomes

$$\Delta\bar{T}_1(\bar{x}\,,\,\bar{h}) = Y_1\, e^{i\bar{x}}\, \frac{D_1 + iD_2}{\lambda\left[N_1 + iN_2\right] + Y_4\left[D_1 + iD_2\right]} \quad . \tag{39}$$

Substituting

$$L_1 = \text{Re}\left[\lambda\left(N_1 + iN_2\right)\right] + Y_4 D_1 \quad , \tag{40}$$

$$\text{and } L_2 = \text{Im}\left[\lambda\left(N_1 + iN_2\right)\right] + Y_4 D_2 \quad , \tag{41}$$

$$\overline{\Delta T_1}\,(\bar{x}\,,\,\bar{h}) = Y_1\, e^{i\bar{x}}\, \frac{D_1 + iD_2}{L_1 + iL_2} \quad . \tag{42}$$

$$\therefore\ \overline{\Delta T_1}\,(\bar{x}\,,\,\bar{h}) = \left(\frac{Y_1}{L_1^2 + L_2^2}\right)\left[\left(D_1 L_1 + D_2 L_2\right) + i\left(D_2 L_1 - D_1 L_2\right)\right] \quad . \tag{43}$$

Hence from equation (34) the thermal-lag becomes

$$\theta_{T.L.} = -\tan^{-1}\left[\frac{\left(D_2 L_1 - D_1 L_2\right)}{\left(D_1 L_1 + D_2 L_2\right)}\right] \quad , \tag{44}$$

and the maximum surface temperature perturbation

$$\overline{\Delta T_{1}}_{max} = \left(\frac{Y_1}{L_1^2 + L_2^2}\right) \sqrt{\left[D_1 L_1 + D_2 L_2\right]^2 + \left[D_2 L_1 - D_1 L_2\right]^2} \quad . \tag{45}$$

Assuming $\lambda\bar{h} = a + ib = \bar{h}\sqrt{c + id}$ (equation (20)),

$$\text{where } a = \bar{h}\left(c^2 + d^2\right)^{1/4} \cos\left[\frac{\tan^{-1}\left(\frac{d}{c}\right)}{2}\right] \quad , \tag{46}$$

$$\text{and} \quad b = \bar{h}\left(c^2 + d^2\right)^{1/4} \sin\left[\frac{\tan^{-1}\left(\frac{d}{c}\right)}{2}\right] \quad , \tag{47}$$

then substituting D_1, D_2, L_1, and L_2 for θ,

$$\theta_{T.L.} = - \tan^{-1}\left[\frac{a \sin(2b) - b \sin h(2a)}{a \sin h(2a) + b \sin(2b) + Y_4\left[\cos h(2a) - \cos(2b)\right]}\right] \quad . \tag{48}$$

Thus the thermal lag can be described by equation (48), where $\theta_{T.L.}$ is a function of the non-dimensional spin rate $\frac{\omega r^2}{\alpha}$ (where r = L and is the radius of the axi-symmetric body), the ablation term Y_2, and the radiation term Y_3.

$$\theta\left(\frac{\omega r^2}{\alpha}, Y_2, Y_3\right) \quad . \tag{49}$$

The thermal lag and the non-dimensionalized surface temperatures are plotted in figures (5, 6, 7, and 8) for epoxy, using equation (12), the mass ablation rate of epoxy.[19] It should be taken into account that the following results are based upon the assumption that the mass ablation model, from Reference 19, is correct for the materials of the test. The properties of epoxy which are listed in Appendix B were also obtained from the same source.

In Figure 5, the thermal lag is plotted versus the non-dimensionalized spin rate for an epoxy model with ablation, conduction and radiation characteristic, and one with conduction only ($Y_2 = Y_3 = 0$). The latter model begins at a thermal lag of 0 degrees when the body is not spinning, and asymptotes to 45 degrees (Figure 6). As the sinu-

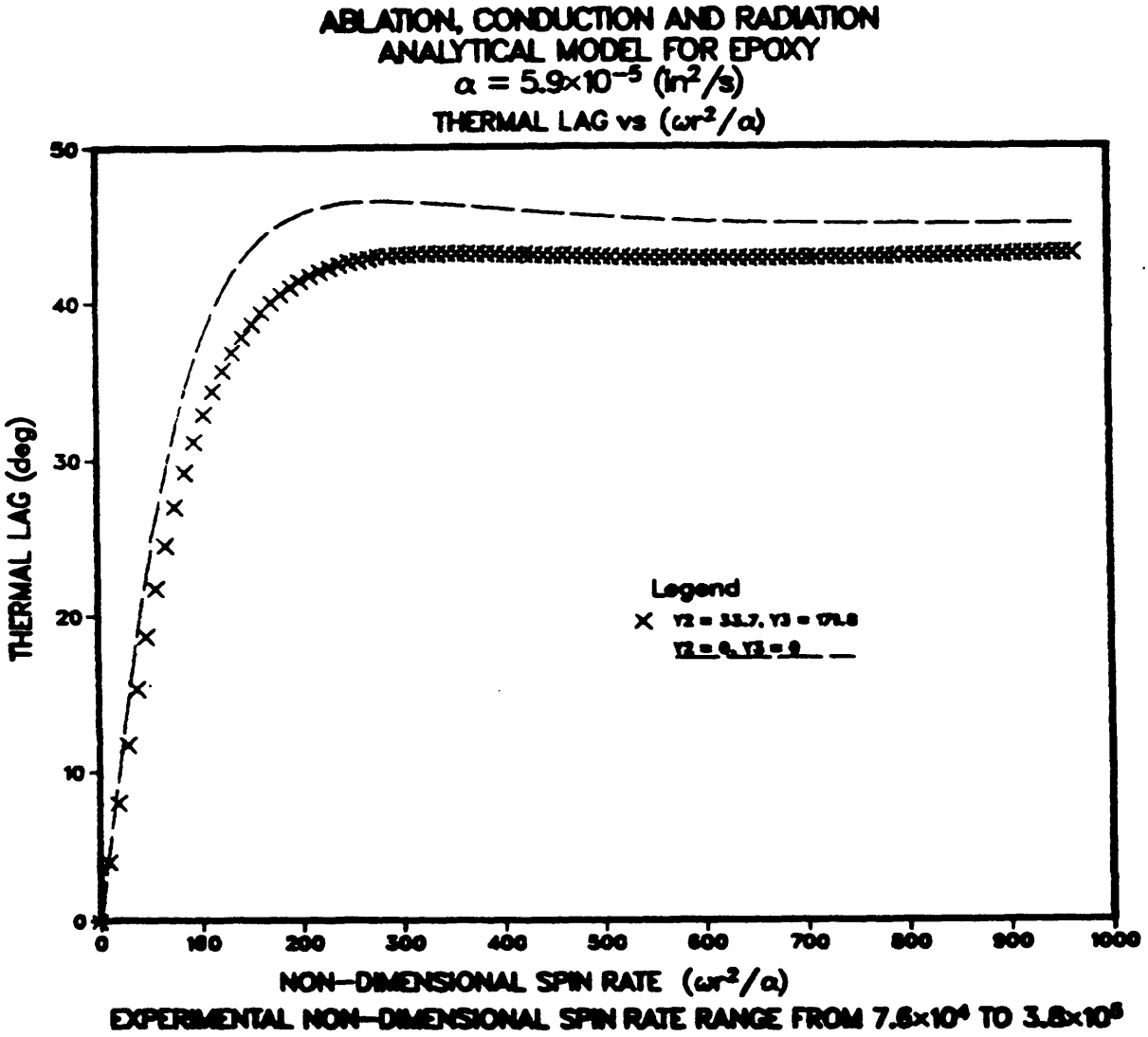

Figure 5. Thermal lag versus non-dimensionalized spin rate (0-1,000), epoxy.

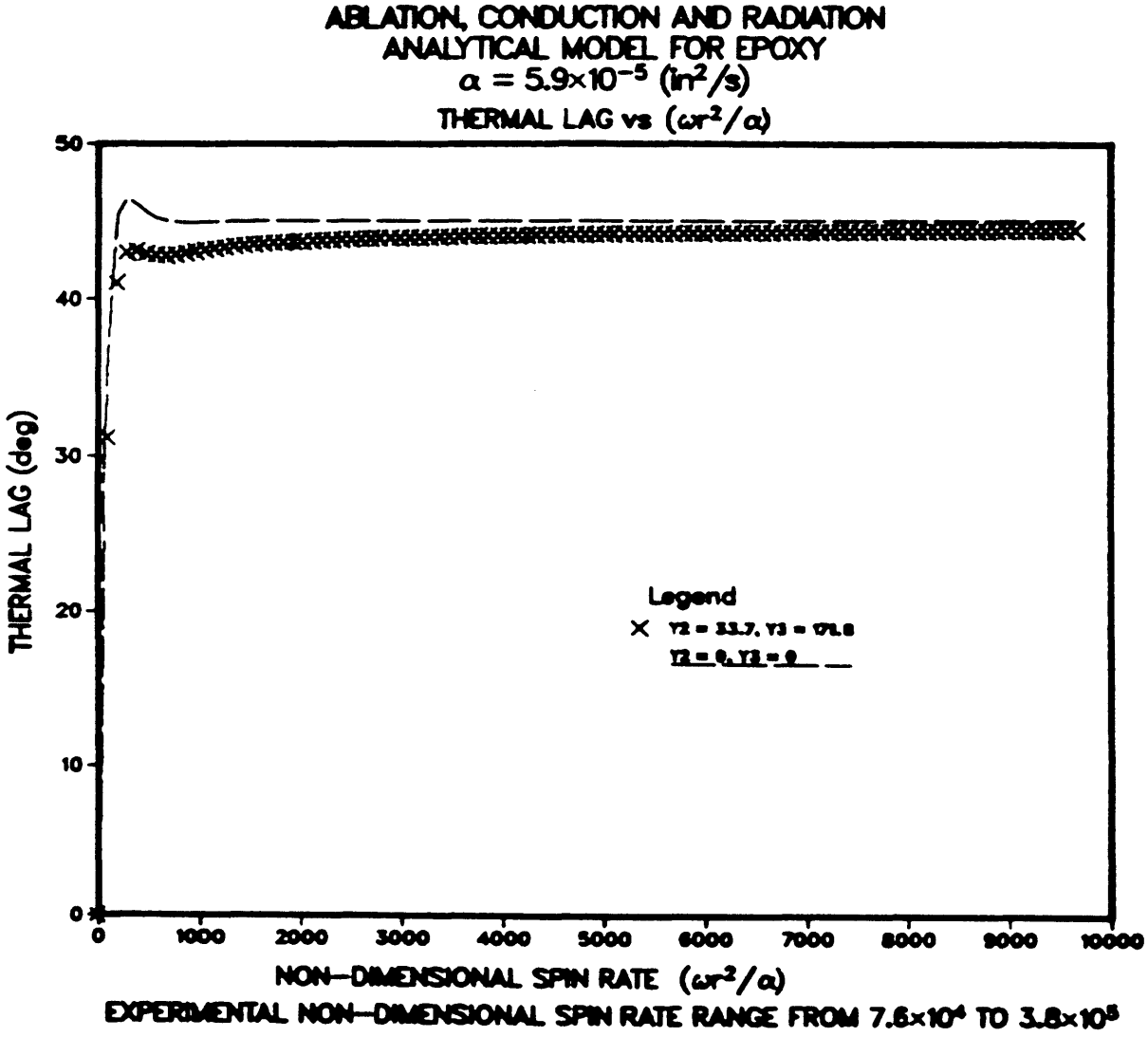

Figure 6. Thermal lag versus non-dimensionalized spin rate (0-10,000), epoxy.

soidal terms are dominant, a peaking effect is seen at spin rates of 200 to 900. The hyperbolic terms tend to dominate at higher spin rates, hence forcing the lag to an asymptote (Figure 6). Similar thermal lag effects are observed for the model including ablation, conduction, and radiation terms, except that the 45 degree asymptote is reached at a higher spin rate. Assuming that the models describe the experiment accurately, as the experimental non-dimensional spin rate ranges from 7.6×10^4 to 3.8×10^5, approximately from 20 to 10 cycles/sec (see Appendix B for dimensional values), it is safe to assume that the thermal lag is at 45 degrees during the M.I.T. Lincoln Laboratory's gas bearing balance test.

Figures 7 and 8 show plots of spin rate versus surface temperature perturbation ($\Delta\overline{T}_{1\,max}$) and total surface temperature ($\overline{T}_{surface}$) respectively. The amplitude of the temperature perturbation at zero spin in the conduction model is higher than when the model is allowed to ablate and radiate. This is true since if ablation and radiation are not present in the model, the temperature gradient into the solid is larger then if they were. Consequently the more complex model is at a lower surface temperature. As $\Delta\overline{T}_{1\,max}$ is only ten percent of the $\overline{T}_{surface}$, the assumption that $\overline{\Delta T}_1 << \overline{T}_1$ is valid.

In order to confirm the results shown in Figures 5 and 6, the value of the thermal lag at the limits where the spin rate is infinite or zero was estimated for the conduction model ($Y_2 = Y_3 = 0$).

Limit $\omega \rightarrow \infty$:

-using equation (2) for λ, (46) and (47) for a and b respectively

-as $\omega \rightarrow \infty$, $d \rightarrow \infty$ (if $\frac{L}{\alpha^*} \neq 0$)

-then $\tan^{-1}(\frac{d}{c}) \rightarrow 90°$ and $\cos\left[\frac{\tan^{-1}(\frac{d}{c})}{2}\right] = \sin\left[\frac{\tan^{-1}(\frac{d}{c})}{2}\right] = \frac{\sqrt{2}}{2}$

-thus a = b and equation (48) becomes

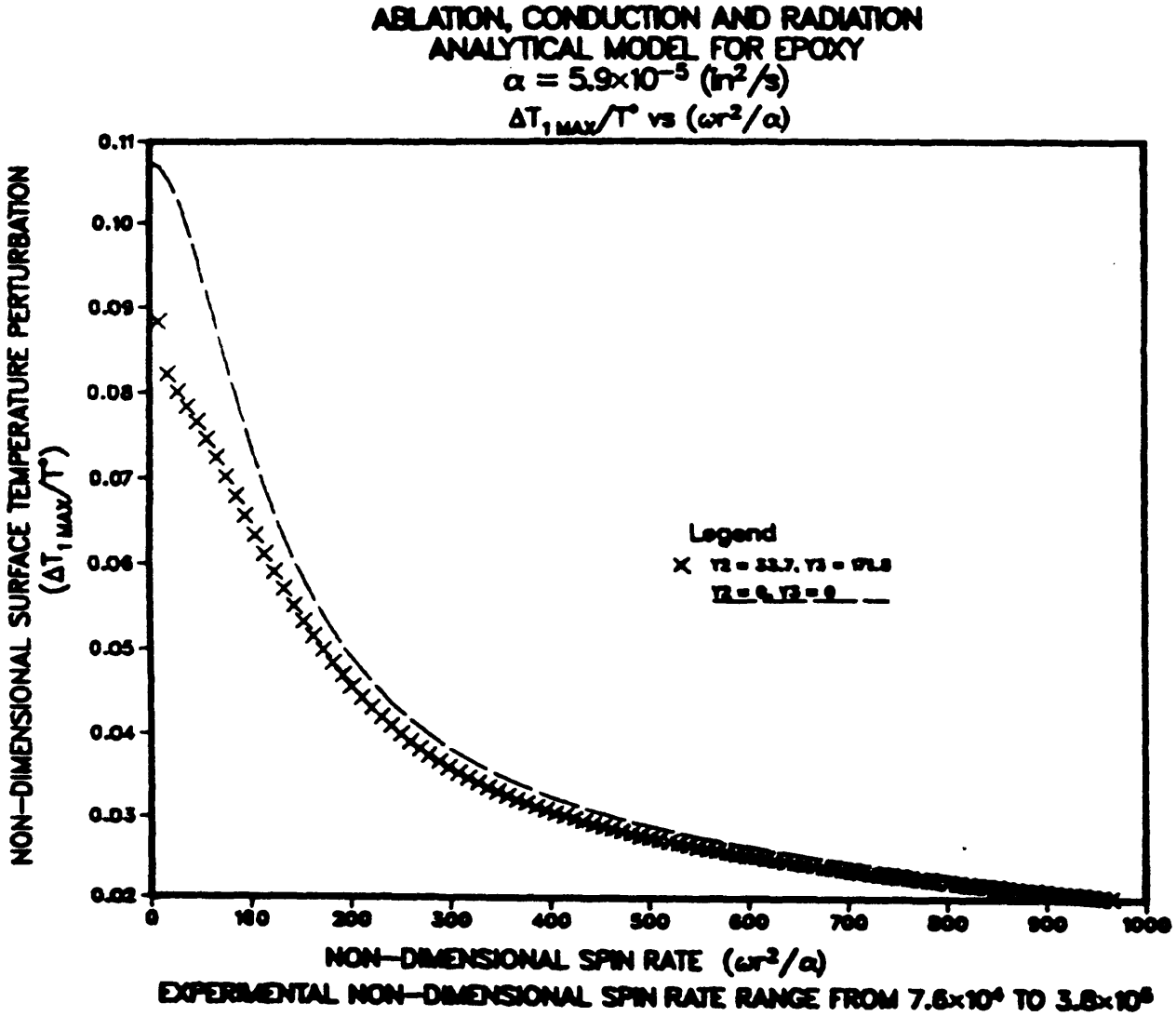

Figure 7. Spin rate versus surface temperature perturbation, epoxy.

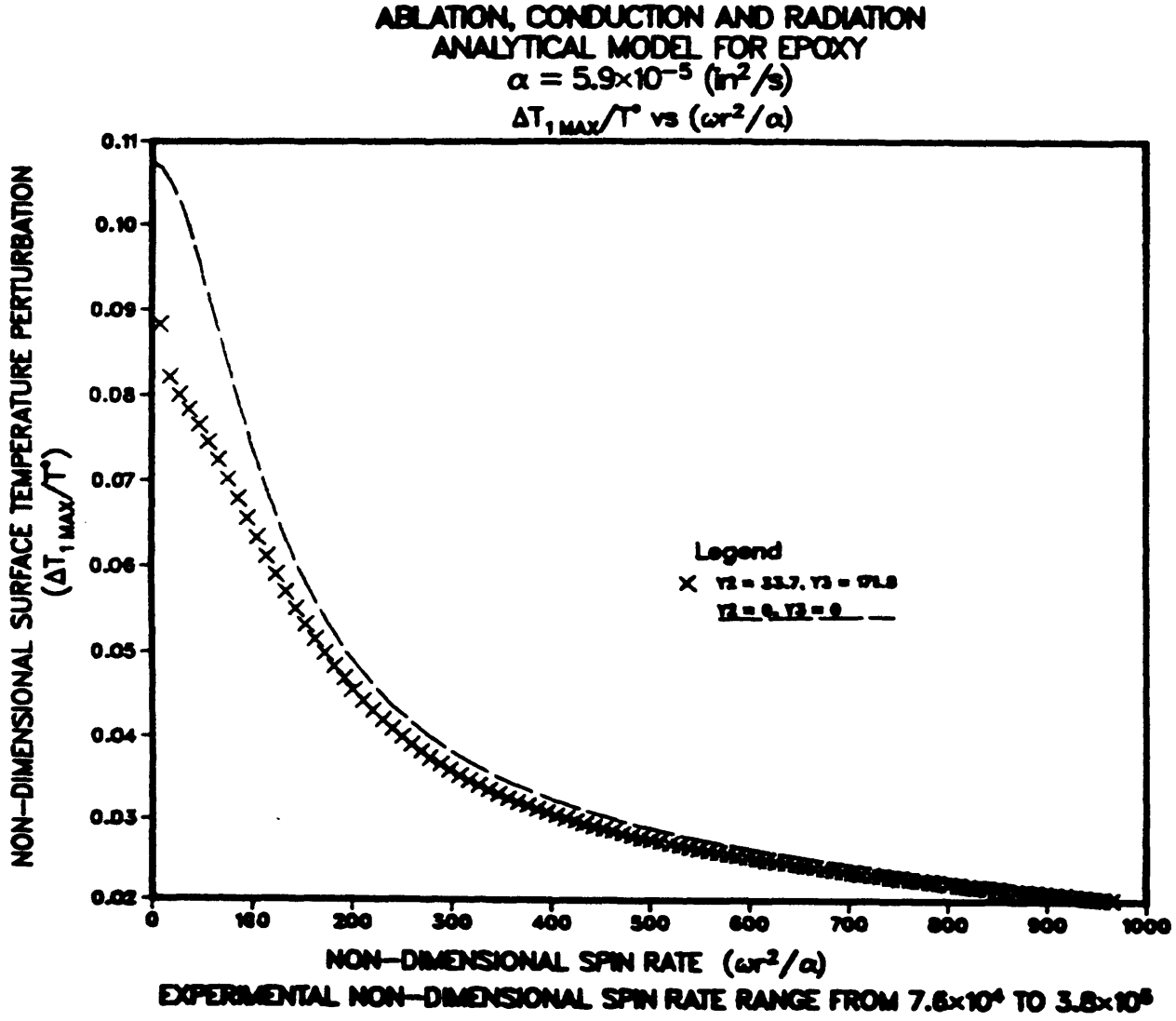

Figure 8. Spin rate versus total surface temperature, epoxy.

$$\theta_{T.L.} = - \tan^{-1} \left[\frac{b \sin(2b) - b \sin h(2b)}{b \sin h(2b) + b \sin(2b)} \right] \quad (50)$$

-as $Y_4 = 0$

-while $b \rightarrow \infty$, sin (2b) oscillates between positive and negative 1, sinh(2b) increases and the latter becomes the dominating term

$$\theta_{T.L.} = -\tan^{-1} \left[\frac{-\sin h(2b)}{\sin h(2b)} \right] = 45° \quad (51)$$

Therefore the limit of the thermal lag when $Y_4 = 0$ and spin rate approaches infinity is 45° from the highest heating rate on the surface in the direction of motion of the slab.

Limit $\omega \rightarrow 0$:

-as $\omega \rightarrow 0$, $d \rightarrow 0$, and $\tan^{-1}(\frac{d}{c}) \rightarrow 0$

-hence $\sin\left(\frac{\tan^{-1}(\frac{d}{c})}{2}\right) \rightarrow 0$ and $b \rightarrow 0$

-thus equation (48) becomes (for $Y_4 = 0$)

$$\theta_{T.L.} = - \tan^{-1} \left(\frac{0}{a \sin h(2a)} \right) = 0° \quad (52)$$

Therefore when the angular velocity is zero, the thermal lag is 0° (there is no lag; the highest temperature is at the windward ray).

In the next section a computational transient conduction model is discussed and compared to this analytical steady-state model.

b) TRANSIENT COMPUTATIONAL CONDUCTION MODEL

The computational modeling of the thermal lag was carried out by using a general thermal analyzer code called SINDA.[22] SINDA, the Systems Improved Numerical Differencing Analyzer, is a software system which possesses capabilities which make it well suited for solving lumped parameter representations of physical problems governed by diffusion-type equations. The system is designed as a general thermal analyzer accepting conductor-capacitor network representations of thermal systems. This code was originally developed by Chrysler Space Division (Cinda and Cinda-3G programs) at New Orleans, Los Angeles in the mid 1960's. The particular version of the program that was used is called SINDA 1983/ANSI.

The input for Sinda consists of a series of input blocks which contain either data or instructions. There are either two or four data blocks and four operations blocks in addition to the title block. A fixed sequence of inputs as indicated in the 1983/ANSI SINDA manual[22] is required. These blocks include:

Block	*Explanation*
Title Input	Title of input for Sinda
Node Data	Contains node number, type (diffusion arthimetic, or boundary), initial temperature and capacitance of node.
Conductor Data	Contains the conductor number, the type (linear or radiation), adjoining node number, and conductor values.
Constants Data	Example: Initial time, final time, and time increment of data analyzed.
Array Data	Contains material characteristics
Execution Operations	Execution of program and setting of array of the number of node.

Variable 1 Operation	Store the boundary conditions (heat flux, temperature).
Variable 2 Operations	Allows user to perform post-solution operations, thus solved network may be examined for quantities such as nodal heat flow.
Output Calls Operations	Calls subroutines for printing data acquired.

(Note: Appendix C shows a flow chart of the Sinda Operations.)

The key in using this network type analysis program, as any other for that matter, lies in the user's ability to develop a lumped parameter representation of the physical problem. Once this is done, superposition of the network mesh is a mechanical task. The following diagram is borrowed from the SINDA 1983/ANSI manual[22] in order to show an example of how the network is lumped:

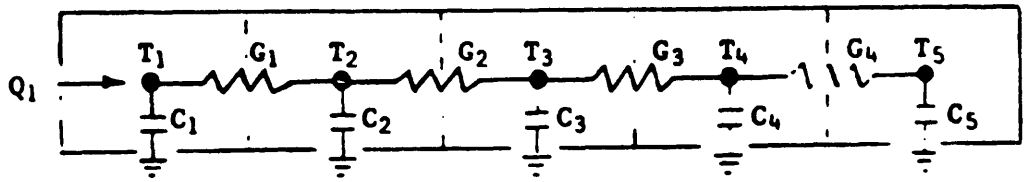

Figure 9. Dimensional heat-transfer numerical model simulation using Sinda.

The "node" points are centrally located within the lumps, and temperature T at the nodes are considered uniform throughout the lump. The capacitors C from the nodes indicate the ability of the lump to store energy. Capacitance values are calculated as lump volume times density times specific heat. The conductor (electrical symbol G) represents the capability for transmitting thermal energy from one lump to another. Conductor values for energy transmission through solids are calculated as thermal conductivity times the energy cross-sectional flow area divided by path length (distance between nodes).[22]

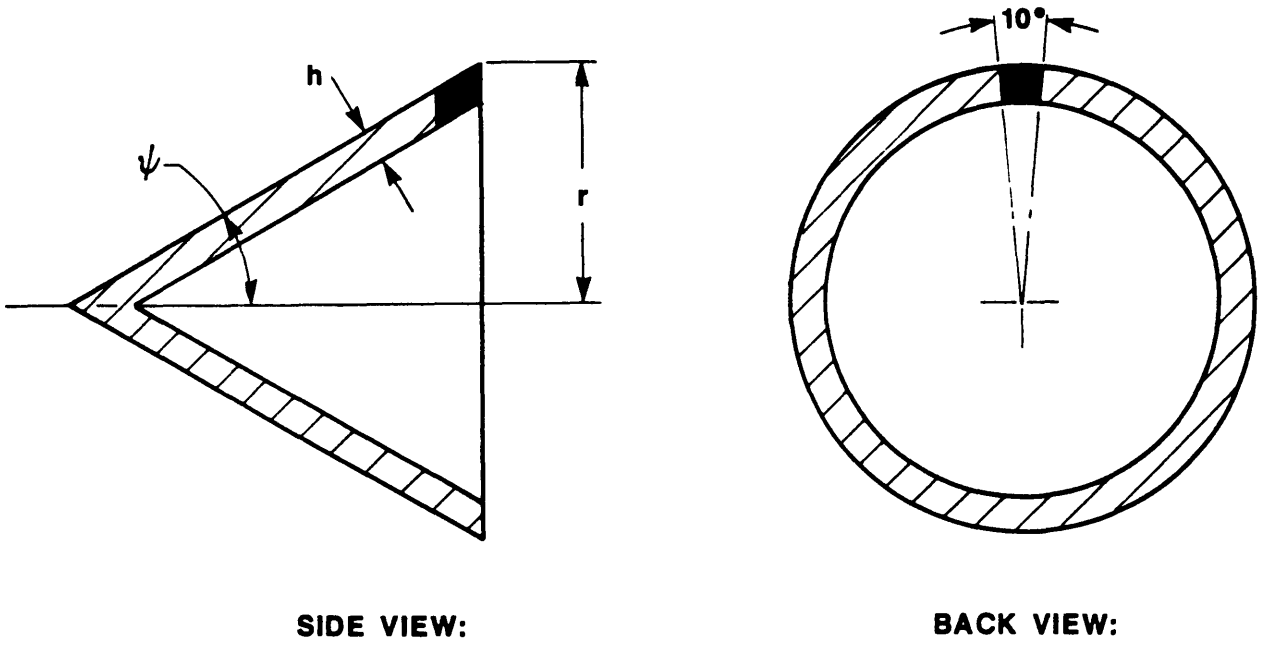

Figure 10. Model of cone section.

Having explained the manner in which SINDA operates, the computational modes used can now be discussed. In Figure 10, two sectional views of a cone are shown. The portion of the cone that has been shaded is the region which undergoes heat conduction in the real problem; the dark region points out an example of an area which has been modeled using SINDA. The thickness of the element being tested was small compared to the base radius of the cone for all the computational models, hence the analysis is only indicative of this type of problem.

Two of the three computational models are shown in Figure 11 (1-D SLAB and 1-D CONE). As it can be seen, the only difference between the two one-dimensional models is that the 1-D CONE took into account the radius of curvature. Different radii were used for the 1-D CONE in order to simulate various positions along the cone. The results obtained for those runs and that of the 1-D SLAB were identical. The third model is a two-dimensional one describing depth and circumferential variations. It was not analyzed, as the semi-infinite heat conduction problem,[23] discussed later in this chapter, demonstrates that the circumferential variations do not effect the thermal lag.

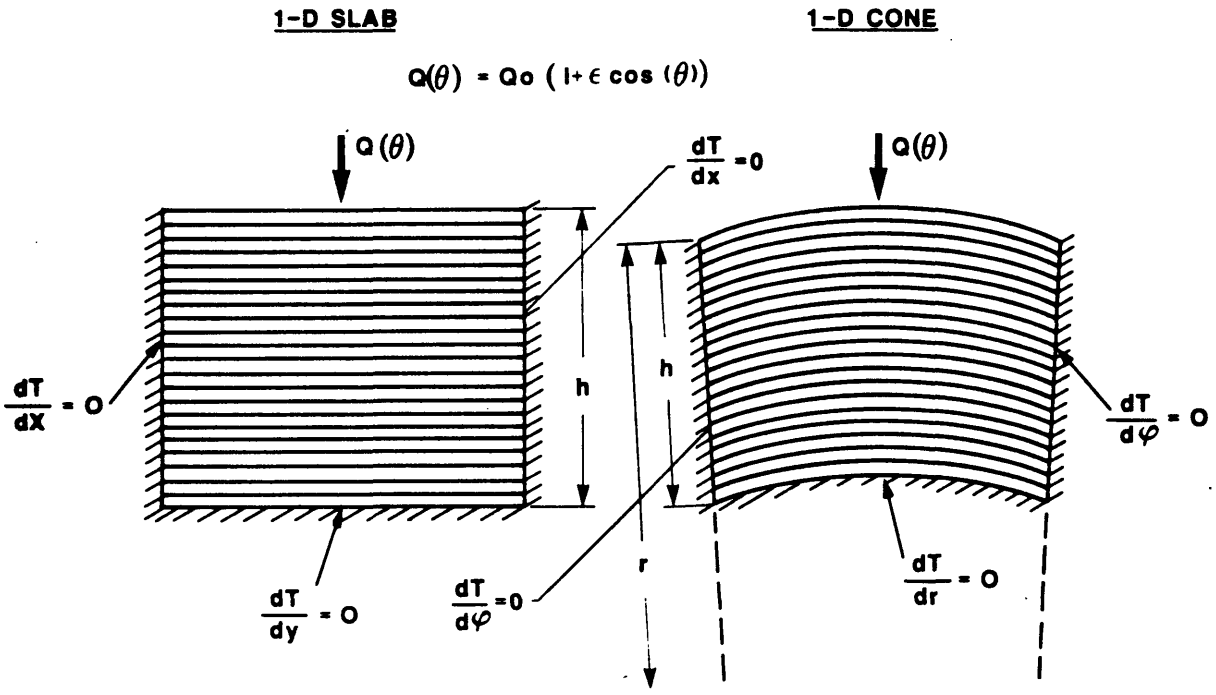

Figure 11. Sinda elements.

Both elements were subjected to a heating rate of

$$Q(\theta) = Qo(1 + \varepsilon \cos \theta) \tag{53}$$

(Figure 2). The side walls and the inner surfaces were adiabatic; the thickness of the two elements were the same.

Taking a look at the results obtained from the one-dimensional computational models, one can see the way the amplitude of the temperature varies throughout the thickness of the elements (Figures 12 and 13). In both figures, the top line shows the surface temperature variation, while lower lines show how the temperature change at inner nodes. Figure 12 depicts this for a spin rate of 7.6×10^4 (2 cycles/sec), whereas Figure 13 demonstrates the 3.8×10^5 (10 cycles/sec) case. As it can be seen, the dampening effect of the latter is greater than the former.

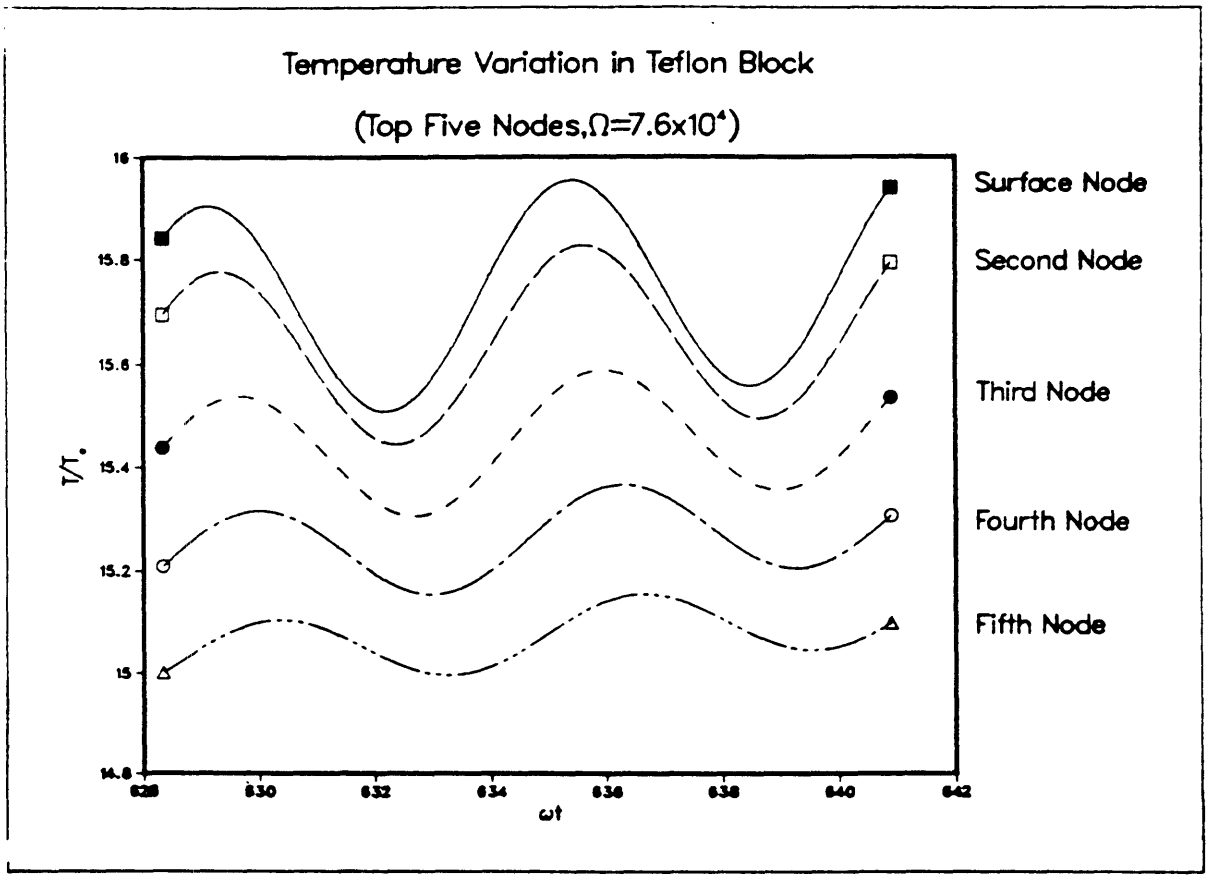

Figure 12. Temperature variation through slab, $\frac{\omega r^2}{\alpha} = 7.6 \times 10^4$, Teflon.

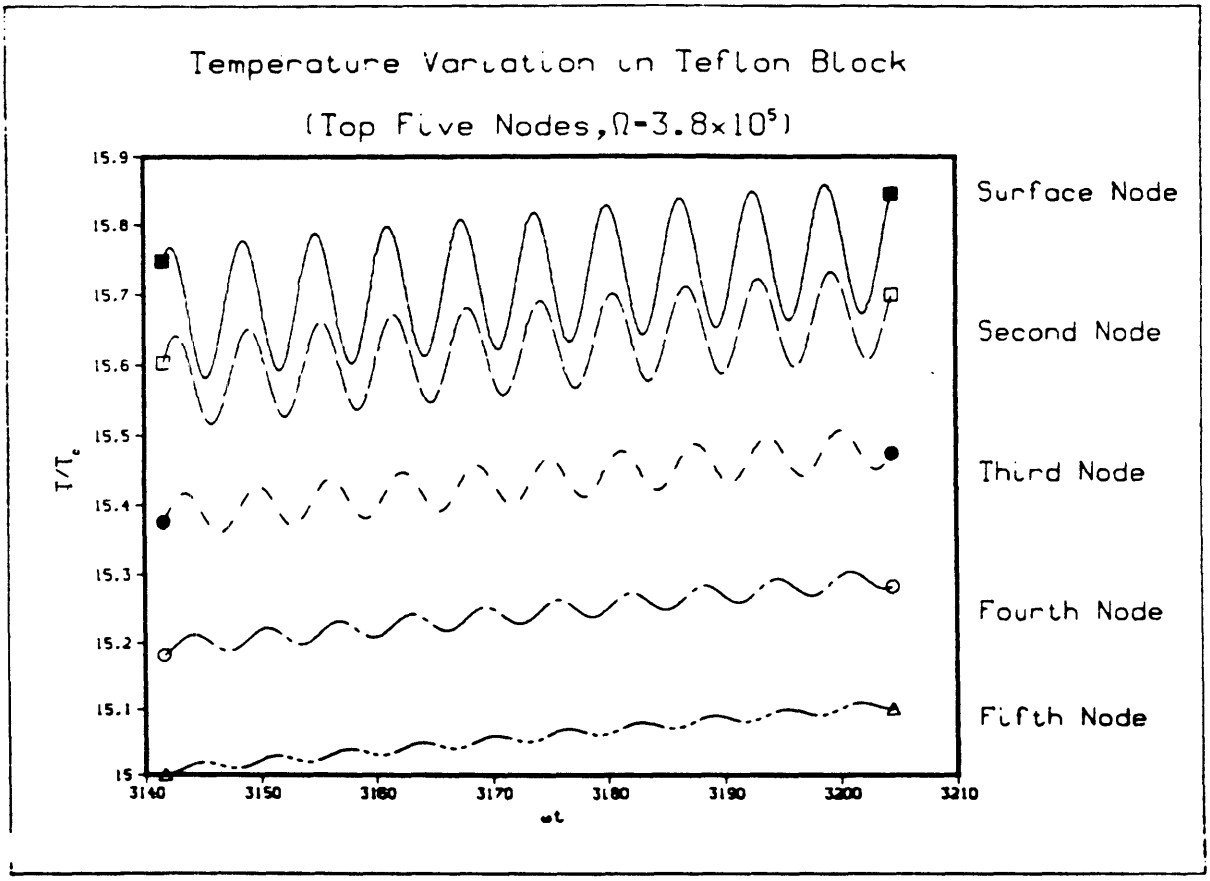

Figure 13. Temperature variation through slab, $\frac{\omega r^2}{\alpha} = 3.8 \times 10^5$, Teflon.

In Figure 14, a plot of the normalized surace temperature with respect to surface temperature at the windward ray (0 degrees) versus angular position around the circumference of the cone, for different rotational frequencies at the same time, is shown. This graph depicts the thermal lag and temperature characteristics of Teflon ($\alpha = 1.6 \times 10^{-4}$) as it undergoes higher spin rates. The plots for other materials were not included here, as they were extremely similar to that of Teflon. As can be seen from Figure 14, while the spin rate increases the thermal lag remains constant at 45°. The minimum temperature occurs naturally at a position 180° from that of the maximum temperature. It can also be noted that the increase in angular velocity reduces the difference between the maximum and minimum temperature points on the model. Hence hypothetically allowing the spin to approach infinity the temperature would become uniform around the circumference, while the thermal lag remains at 45°. (Note: As the angular velocity was increased, the time step at which data was taken was increased, and the data obtained was less accurate, hence the largest ω used for the plot was at 20 cycles/sec.)

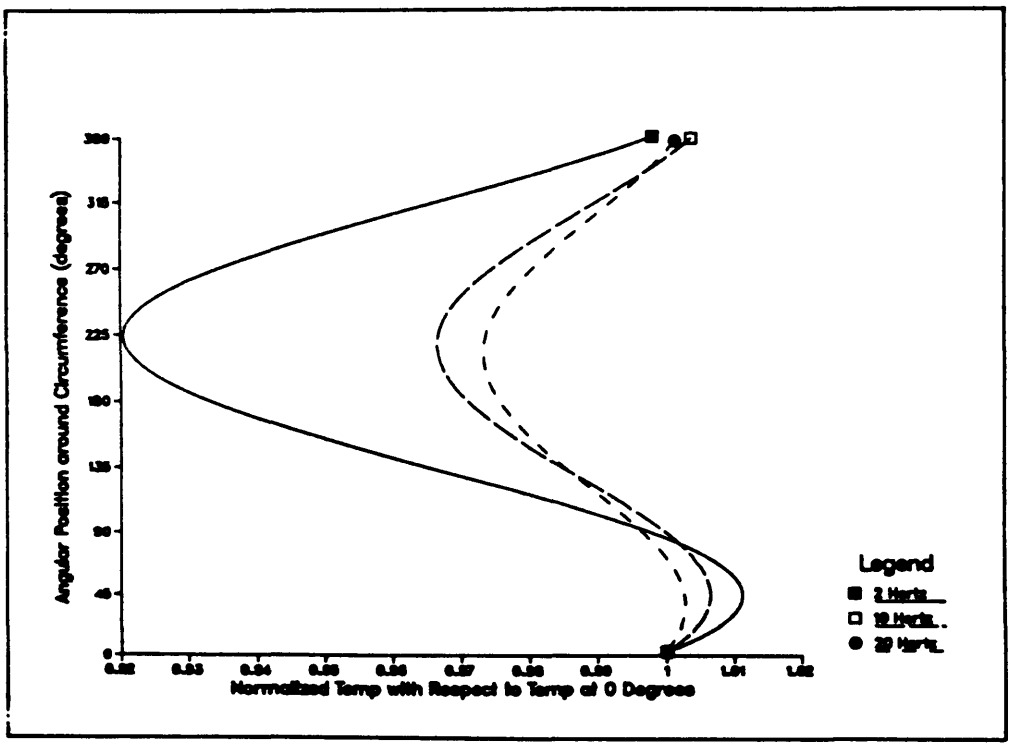

Figure 14. Angular position around cone versus normalized surface temperature, Teflon.

The idea of running the two-dimensional model describing both the depth and circumferential variations using SINDA, was abandoned, due to the lengthy computational time, and thus cost. Nevertheless the semi-infinite heat conduction problem[23] satisfied the uncertainty of having an over simplified one-dimensional model, as the circumferential variation does not effect the thermal lag.

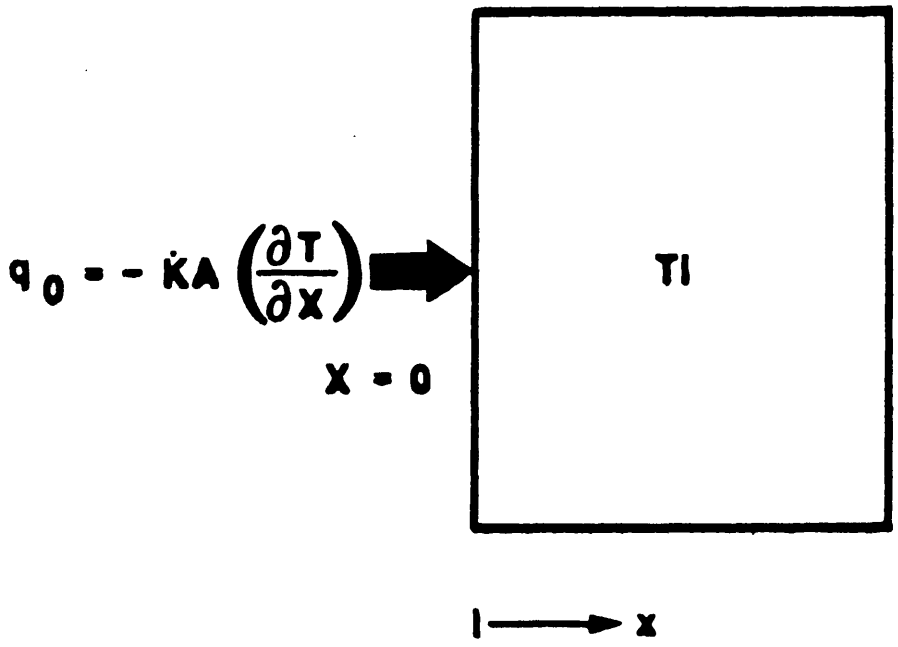

Figure 15. Semi-infinite heat conduction problem.

Assume a semi-infinite solid that is at an initial temperature Ti. The temperature on the surface is suddenly lowered to To. In order to find an expression for the temperature distribution in the plate as a function of time, the following differential equation is used

$$\frac{\partial^2 T}{\partial x^2} = \frac{1}{\alpha}\frac{\partial T}{\partial t} \quad , \tag{54}$$

where x = displacement into solid and t = time. The boundary conditions are

$$T(x, 0) = Ti$$

$$\text{and} \qquad T(0, t) = To \qquad \text{for } t > 0 \quad . \tag{55}$$

Using the Laplace transform technique employed and the solution given in Reference 24

$$\frac{T(x, t) - To}{Ti - To} = \text{erf}\left[\frac{x}{2\sqrt{\alpha t}}\right] , \tag{56}$$

where the Gauss error function is defined as[23]

$$\text{erf}\,\frac{x}{2\sqrt{\alpha t}} = \frac{2}{\sqrt{\pi}} \int_0^{x/2\sqrt{\alpha t}} e^{-\eta^2}\, d\eta \ . \tag{57}$$

Thus the temperature distribution can be derived. (Note: η is a dummy variable and the integral is a function of its upper limit.)

Using the graph of the temperature distribution shown in Figure 16,[23]

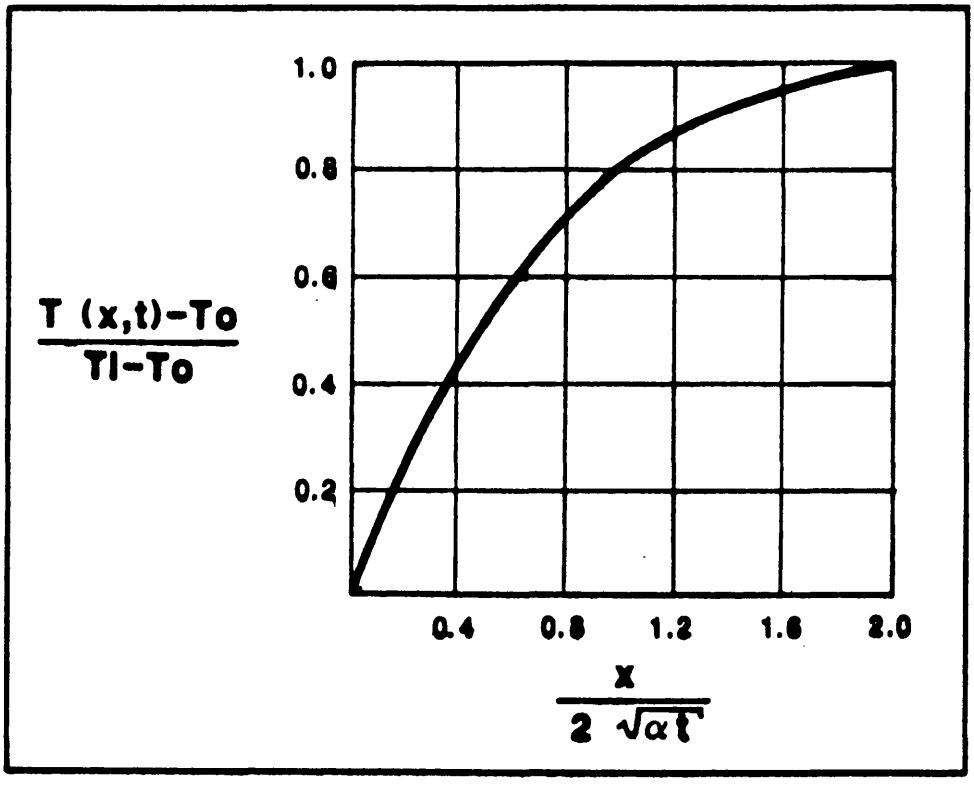

Figure 16. Temperature distribution in the semi-infinite solid.

the value for $\frac{x}{\sqrt{\alpha t}}$ can be obtained with a temperature distribution of 0.99.

$$\text{erf}\left[\frac{x}{2\sqrt{\alpha t}}\right] = 0.99 \quad . \tag{58}$$

From Figure 16,

$$x = 3.6\sqrt{\alpha t} \quad . \tag{59}$$

Examine the time it takes to heat a location of 0.25 inches into the solid for two materials with different thermal diffusivities:

for Teflon (at $x = 0.25$ in and $\alpha = 1.6 \times 10^{-4}$ in^2/s): $t = 29$ sec, and

for copper (at $x = 0.25$ in and $\alpha = 0.3416$ in^2/s): $t = 0.014$ sec.

As the time it took to heat the inner surface of the element for Teflon was large, the effect of the circumferential heating was minimal; thus the results were satisfactory for the 1-D case. For copper on the other hand, although the inner surface heated quickly, the circumferential heating would merely affect the amplitude of the temperature and not the lag angle; hence as the temperature amplitude is not of concern here whereas the thermal lag is, once again, the 1-D case is satisfactory.

A thermal lag of 45° is thus predicted by both the steady-state analytical infinite slab and the transient computational finite nodal block models. As the spin rate increases the lag angle does not vary, whereas as the temperature distribution becomes uniform around the body. It should be noted that the computational model, being 1-D, does not allow for circumferential heat conduction. Thus for low spin (approaching zero) and high-thermal diffusivities the model is not very good. Nevertheless the analytical model allows the author to conclude that when the spin rate is zero, the thermal lag is zero.

Chapter 3

Reduction and Analysis of M.I.T. Lincoln Laboratory 20-MW Arc Jet Force Data

a) THE EXPERIMENT

Although presently the most common means of discerning aerodynamic loads induced on wind-tunnel models has been the utilization of strain gage balances, these balances suffer from a number of deficiencies. The most significant of these drawbacks is the coupling between balance sensitivity and balance stiffness.[25] Increasing the design load induces an increase in the balance stiffness which consequently results in lowering of the resolution.

Other drawbacks of the strain gage balance include its sensitivity to electrical noise and ambient temperature.[25] In experiments where temperature transients or electro-magnetic interferences are present in the test environments a different balance is desirable.

Using gas bearing technology,[26] M.I.T. Lincoln Laboratory's Aerospace Engineering Group has designed a hydrostatic gas bearing wind-tunnel balance. This balance consists of two hydrostatic journal bearings coupled to a double acting thrust bearing. Aerodynamic loads are measured as a function of differential hydrostatic film pressures between the support shaft and bearing surfaces. The primary purpose behind building this gas bearing balance is to measure the ablation aerodynamic forces and moments of heat shield materials.

Using the gas bearing balance, M.I.T. Lincoln Laboratory investigated ablation aerodynamic effects at the NASA Ames Research Center 20-megawatt Aerothermal facility. As this was the first experiment ever performed using the newly designed gas bearing balance, the following were the test and data reduction goals:

1. To evaluate an air bearing wind-tunnel balance capable of measuring ablation aerodynamic forces where conventional strain gage balances suffered low signal to noise ratios.

2. To obtain preliminary data on ablation aerodynamic forces and moments for heat shield materials.
3. To provide compatible data acquisition for NASA Ames 20-megawatt arc tunnel.
4. To develop experimental techniques for using the air bearing wind-tunnel balance and the data acquisition system.

The test setup is shown in Figure 17. Different models of various heat shield materials (teflon, epoxy, and graphite) were tested downstream of the 12-inch diameter arc-jet exhaust nozzle. The model pitch or yaw angle of attack was remotely controlled during the ablation testing. A roll rate between 0 to 10 Hertz could be produced by setting an electric spin motor which was housed in the sting. The sting-support assembly was mounted to the Ames X-Y traversing table which in turn allowed the insertion of the sting-assembly model within the arc-jet exhaust plume. All instrumentation leads from the model sting assembly were accessed through a port-flange cover plate located on the test cell wall. Outside the test cell these instrumentation leads were connected to a workstation which controlled and monitored the experiment with electrically isolated hardware. This was to ensure the safety of the test operator and hardware, so that they would not be subjected to high-voltage static discharges which could have occurred during plasma formation within the arc-jet exhaust plume.

Prior to the experiment, the balance was calibrated. A hydrostatic journal bearing was used to apply calibration loads and moments to either a spinning or nonspinning air bearing balance shaft. These balance calibrations were repeated and pressure data were recorded. In order to reduce the force data an influence coefficient matrix was developed as described in Reference 27, namely:

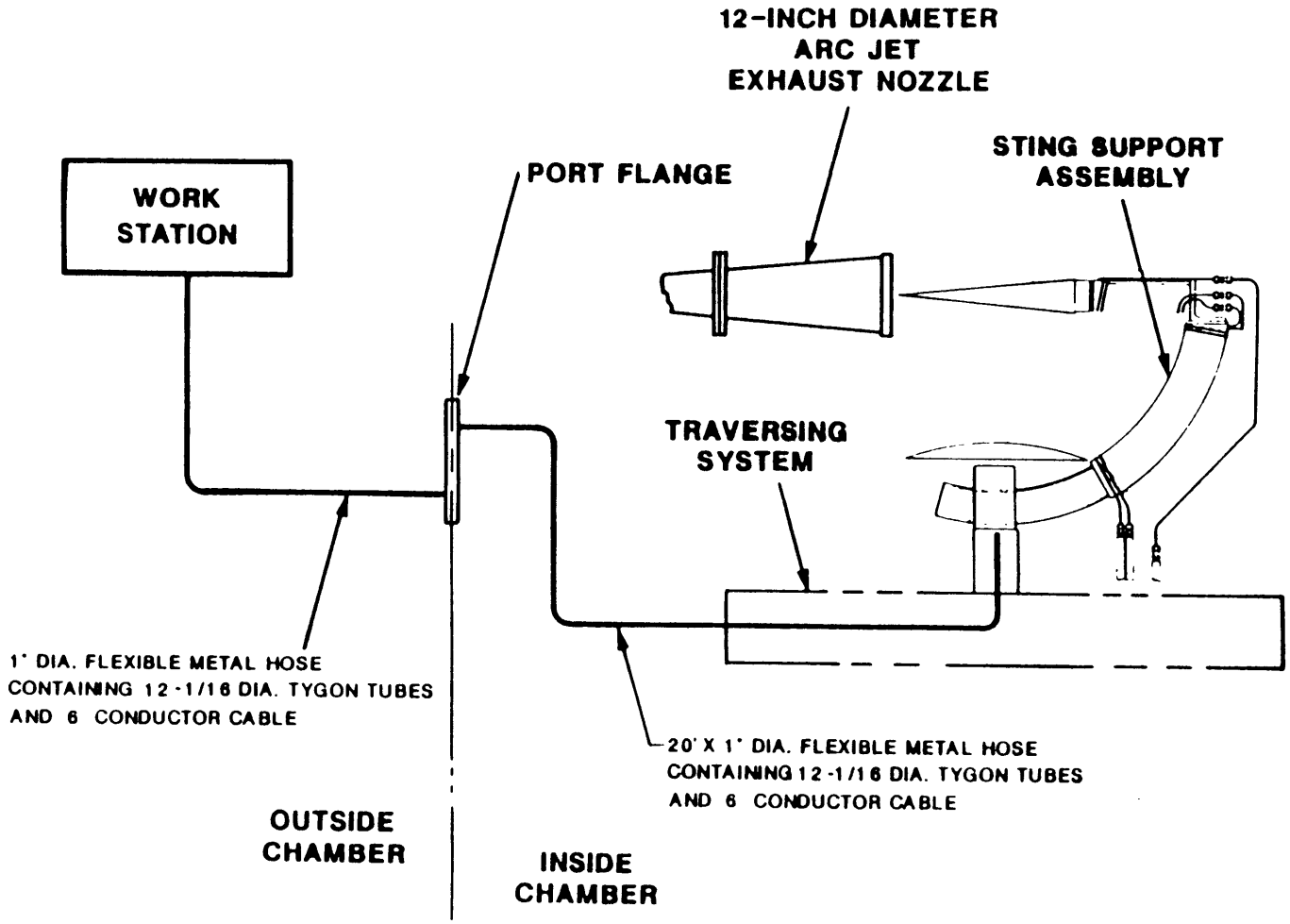

Figure 17. Ames ablation test setup.

$$\begin{bmatrix} P_1 \\ P_2 \\ P_3 \\ P_4 \end{bmatrix} = \begin{bmatrix} C_{11} & C_{12} & C_{13} & C_{14} \\ C_{21} & C_{22} & C_{23} & C_{24} \\ C_{31} & C_{32} & C_{33} & C_{34} \\ C_{41} & C_{42} & C_{43} & C_{44} \end{bmatrix} \begin{bmatrix} F_1 \\ F_2 \\ M_1 \\ M_2 \end{bmatrix} \tag{60}$$

where $P_1 = \Delta P_1 + \Delta P_3$ (See Figure 18)

$P_2 = \Delta P_2 + \Delta P_4$

$P_3 = \Delta P_1 - \Delta P_3$

$P_4 = \Delta P_2 - \Delta P_4$

F_1 = Normal Force

F_2 = Side Force

M_1 = Pitching Moment

M_2 = Yawing Moment

ΔP_n = Difference in pressure taps n (See Figure 18).

The journal bearing shown in Figure 18 is approximately 2.8 inches in length with a shaft diameter of 0.5 inches. It contains four pairs of 0.007 inches diameter pressure taps and thirty-two 0.007 inches diameter gas-injection of holes. Each tap is situated in the middle of four feed holes to provide a balanced bleed off from the journal flow. The design called for pressure-tap mass flow to be 25% of the total flow. This was the maximum allowable bleed off that would not collapse the bearing's supporting film.

Using

$$\begin{aligned} P_1 &= C_{11}F_1 + C_{12}F_2 + C_{13}M_1 + C_{14}M_2 \\ P_2 &= C_{21}F_1 + C_{22}F_2 + C_{23}M_1 + C_{24}M_2 \\ P_3 &= C_{31}F_1 + C_{32}F_2 + C_{33}M_1 + C_{34}M_2 \\ P_4 &= C_{41}F_1 + C_{42}F_2 + C_{43}M_1 + C_{44}M_2 \ , \end{aligned} \tag{61}$$

the matrix [C] could be found by using known loads and moments and calibration results for P_n. For example, applying a normal force at the center of pressure of the journal bearing (moments and side force are zero),

$$P_1 = C_{11}F_1 \quad . \tag{62}$$

Therefore,

$$C_{11} = \frac{\Delta P_1 + \Delta P_3}{F_1} \quad . \tag{63}$$

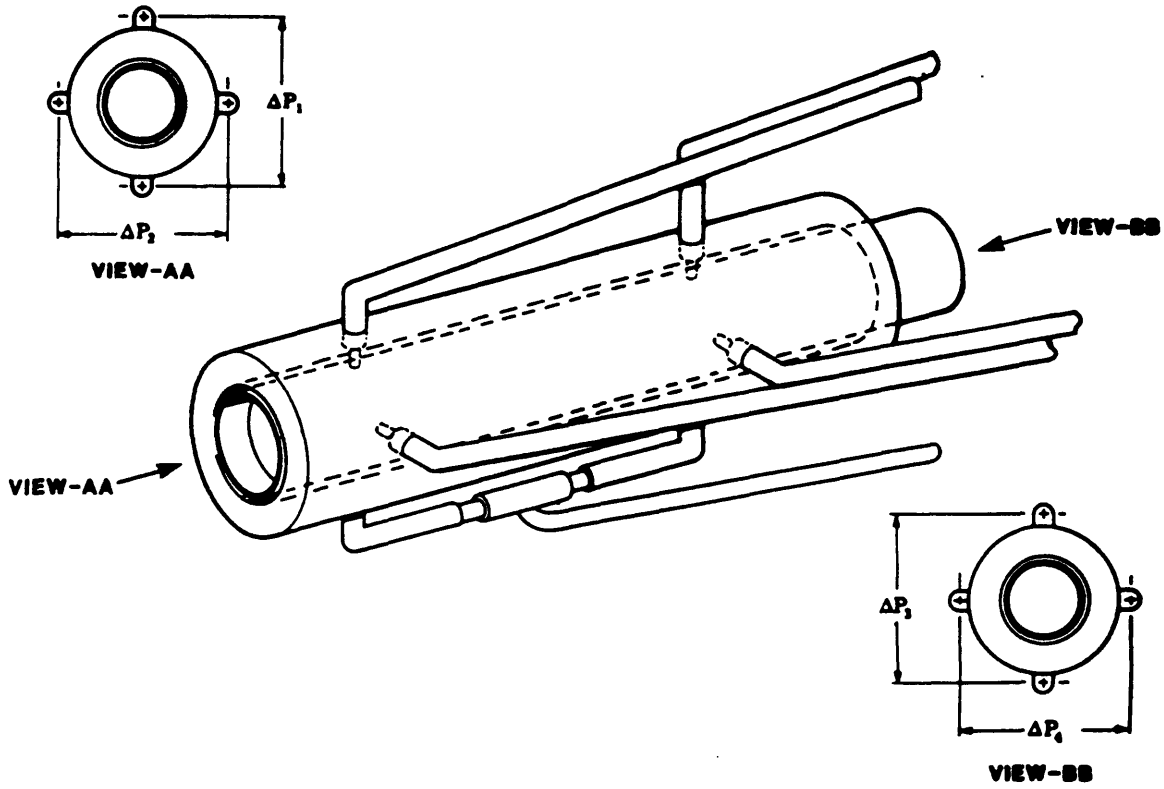

Figure 18. Position of pressure taps on the journal bearing.

Likewise all components of the influence coefficient matrix were found. The magnitude of the off-diagonal terms indicated the degree of the balance linearity. (Appendix D includes the values obtained for the influence coefficient matrix used.) This matrix was then used in order to reduce the results shown in the next section.

The results of the balance calibration data are presented in Appendix E. Linear behavior was observed in both the side force and yawing moment calibration data. Normal force and pitching moment calibration data were also linear except the normal force data showed non-linearity at the lower loads of 0.25 to 0.5 lb_f. The non-linearity was investigated and believed to be caused by a leak at the pressure taps measuring the normal force and pitching moment. As the error in the pressure readings was additive for the force data and subtractive for the moment,

$$F_1 \propto (\Delta P_1 + \varepsilon) + (\Delta P_3 + \varepsilon) = \Delta P_1 + \Delta P_3 + 2\varepsilon \tag{64}$$

$$M_1 \propto (\Delta P_1 + \varepsilon) - (\Delta P_3 + \varepsilon) = \Delta P_1 - \Delta P_3 \ , \tag{65}$$

where now ε = error in pressure reading due to leak, the pitching moment calibration data seems linear. Nevertheless prior to the test the leaks seemed to have been sealed by on-site repair as recalibration after the test showed linearity throughout the data.

Figure 19 shows balance raw data from the forward, normal plane pressure taps during a typical run in the Ames 20-megawatt Aerothermal facility. This data is recorded at 1/64 second intervals and averaged over one second. It clearly shows the asymptotic time response characteristics of the balance after 20 seconds. The lower portion of the graph displays the standard deviation of the data. The maximum standard deviation during the run was 3% of the data obtained. Given the conditions of the arc-jet environment, this ratio is quite acceptable and demonstrates the functionality of the balance under adverse test conditions.

Forward, Normal Plane Pressure Taps, Run 15, Epoxy.

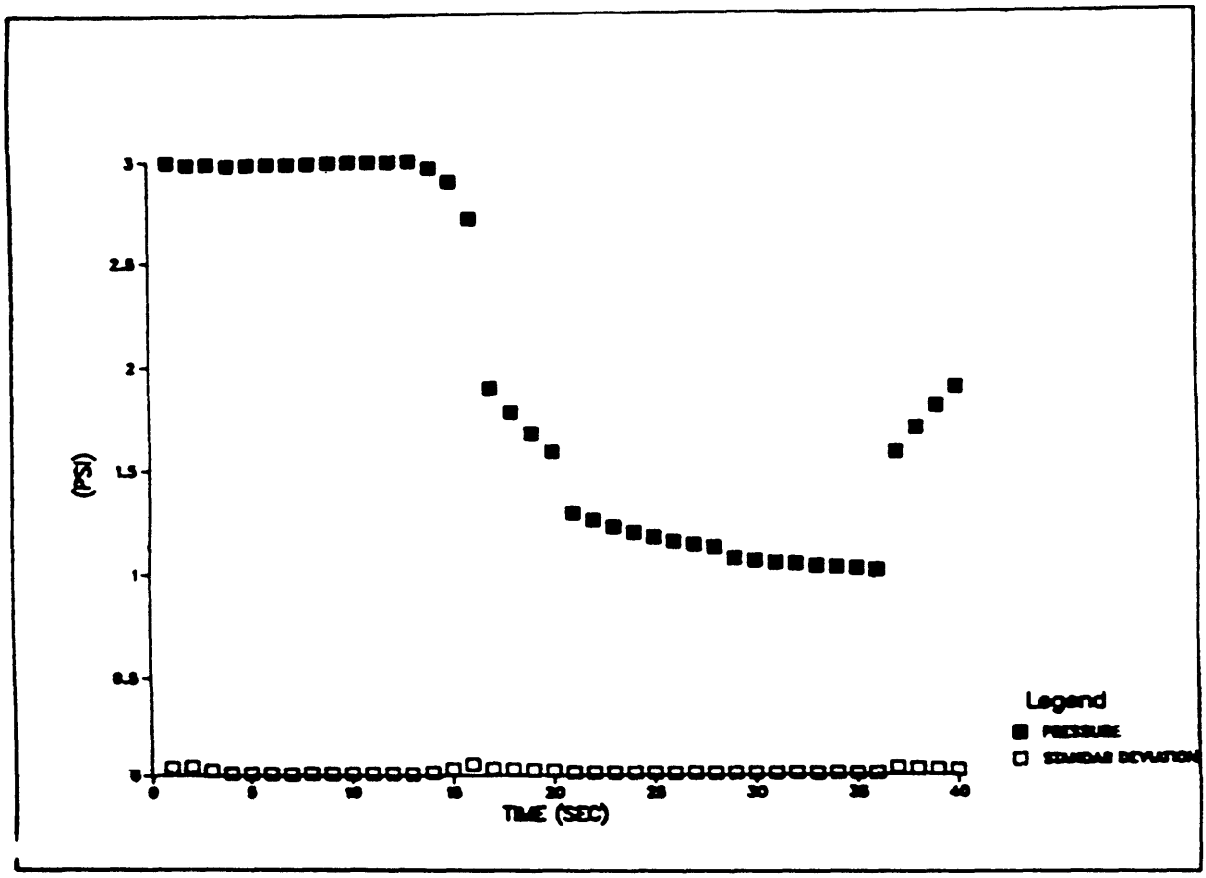

Figure 19. Balance raw data.

b) ANALYSIS OF EXPERIMENTAL RESULTS

The experimental force results are calculated using the influence coefficient matrix technique described in Reference 27. The journal on the hydrostatic gas-bearing wind-tunnel balance is designed for a maximum load of 5 lbf. The forces measured in the experiment are well under this limit. These forces and their respective moments are measured for Teflon, epoxy, and graphite heat-shield materials at various yaw and pitch angles. Figures F-1 through F-12 (Appendix F) are plots of the graphite, epoxy and Teflon data reduced from the test results. As the error margins in these graphs were extremely small for most of the points, the bars were only indicated for the points with significant margins. The average force data was ±14.7% of the calculated value.

Graphite ($\alpha = 1.3 \times 10^{-2}$ in^2/s) forces and moments are shown in Figures F-1 through F-4. The normal force and pitching moment do not vary significantly with yaw angle, but are affected by the change in pitch angle. The yawing angle influences the yaw moment, whereas the pitch angle appears to induce a side force on the body. As graphite at the experimental arc jet conditions can be considered practically a non-ablating material (if the surface temperature of any known material is increased, eventually the material will ablate), the side force due to pitch is likely a result of model support pitch-yaw coupling and not the ablation characteristics of the material. It is possible that the graphite shell placed in the tunnel experienced a deflection in the yaw direction due to the flexing loads of support cooling tubes as the body was pitched.

Figure 20 shows a picture of the graphite heat-shield cone in the arc tunnel at angle of attack (pitch).

Epoxy ($\alpha = 5.9 \times 10^{-5}$ in^2/s) forces and moments are shown in Figures F-5 through F-8. Once again the normal force and pitching moment do not vary with yaw angle, but are affected by pitch. However, the side force and yawing moment are influenced by both yaw and pitch angles. In the initial tests anomalous side force due to pitch appears to be related to lack of stiffness of the model support which is being re-built along with other changes designed to remove these interactions. The side force and yawing moment

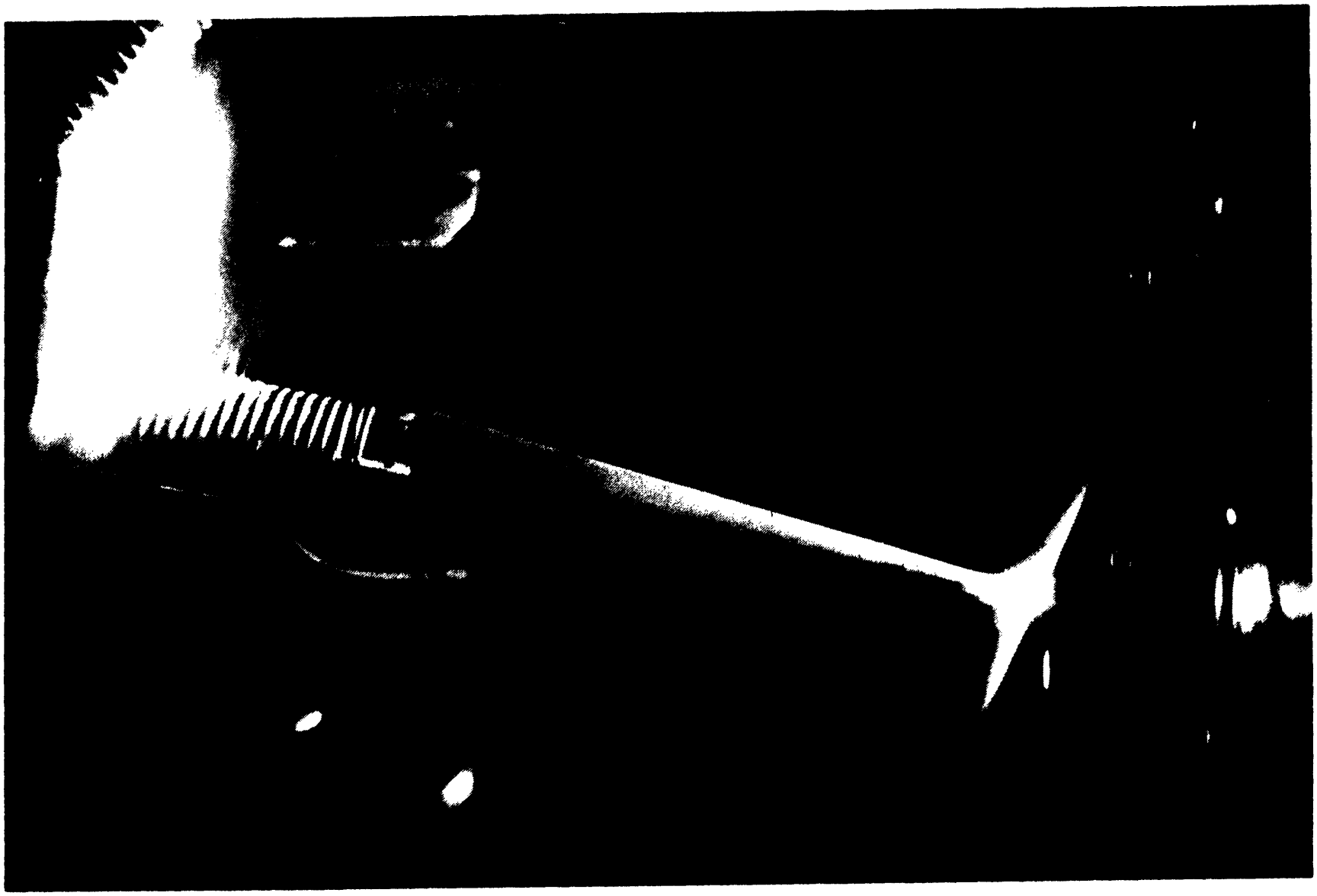

Figure 20. Graphite model at angle of attack in arc tunnel.

combine the effect of yaw coupling and ablation characteristics of epoxy (Epoxy ablation temperature ranges from 2,300 to 2,800°R approximately).

Figure 21 shows a picture of an ablating epoxy model placed at zero angle of attack in the arc jet. The white region around the cone is the ablated epoxy within the boundary layer of the body. Comparing Figure 21 to 20, one can immediately see the justification in assuming that the graphite model does not ablate.

Finally Teflon ($\alpha = 1.6 \times 10^{-4}$ in^2/s) forces and moments are shown in Figures F-9 through F-12. As can be seen from these plots there seems to be a large scatter in the Teflon results, and although the data is shown here, no concrete conclusions can be made from these graphs. The scatter in the data is due to poor annealing of the Teflon model which caused the body to undergo shape change under heating.

In order to calculate the thermal lag $\theta_{T.L.}$ from the experimental data, it is necessary to make an important assumption. The thermal lag has been defined here to be the angle from the windward ray in the direction of rotation at which the surface temperature is greatest. The higher surface temperature induces higher mass loss off the body. The mass loss contributes to an average momentum flux in a certain direction, and this momentum flux in turn creates a force. Call the momentum lag, the angle from the windward ray in the direction of rotation at which the momentum flux off the body is the largest. Assuming the value of the momentum lag is the same as the thermal lag, $\theta_{T.L.}$ may be calculated from the experimental data.

Define F_N the sum of the aerodynamic (F_{N_0}) and ablation induced (F_{N_B}) forces in the normal direction

$$F_N = F_{N_o} + F_{N_B} \quad . \tag{66}$$

Define F_S the sum of the aerodynamic (F_{S_0}) and ablation induced (F_{S_B}) forces in a direction perpendicular to the normal

$$F_S = F_{S_o} + F_{S_B} \quad . \tag{67}$$

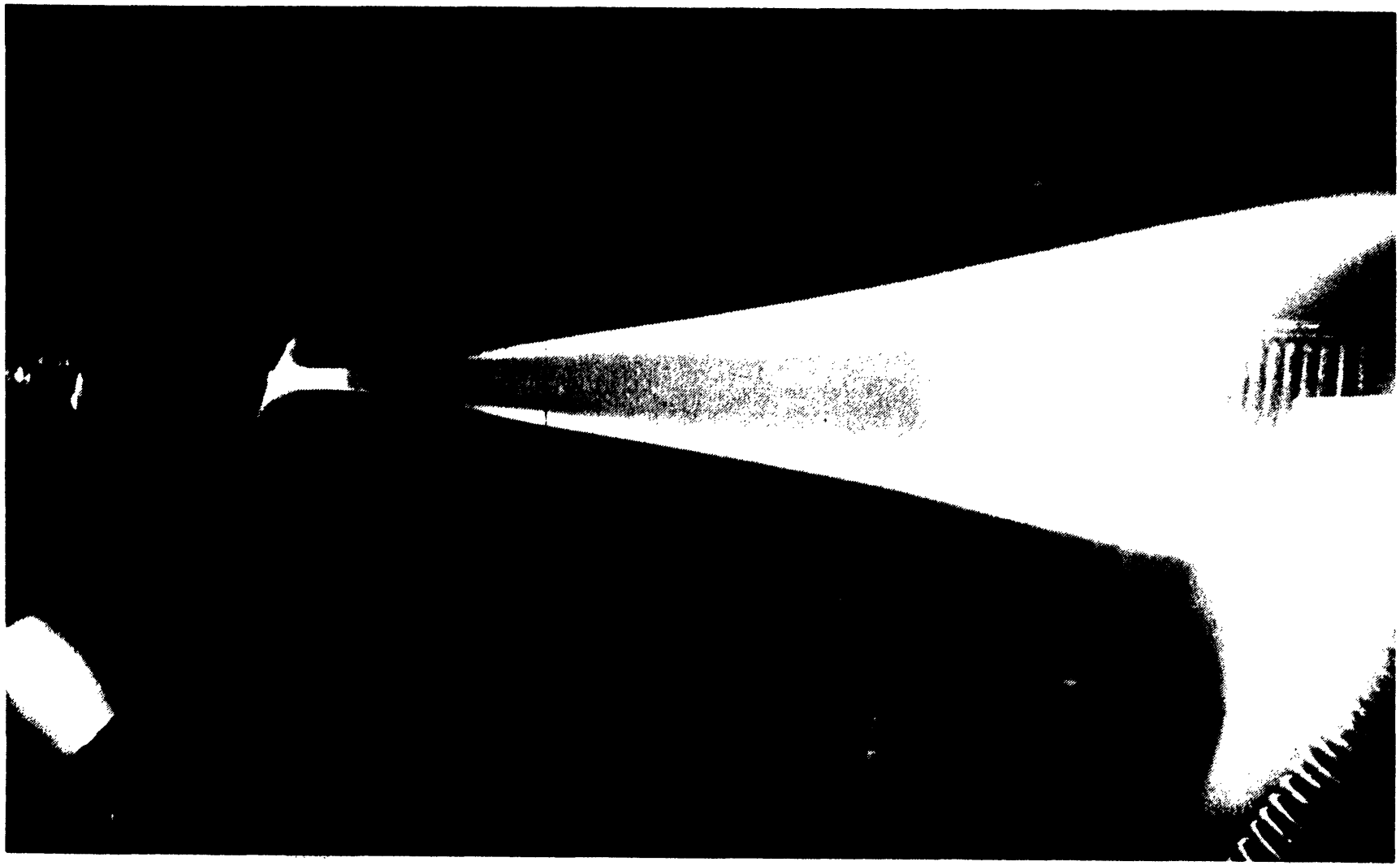

Figure 21. Epoxy model at zero angle of attack in arc tunnel.

For an axi-symmetric spinning body at angle of attack (pitch) undergoing a sinusoidal heating

$$Q(\theta) = Q_o (1 + \varepsilon \cos\theta) \quad , \tag{68}$$

where now ε is a function of angle of attack and $\theta = 0$ at the windward ray (Figure 22), the aerodynamic force contribution is solely in the normal direction

$$F_{S_o} = 0 \quad . \tag{69}$$

Assuming momentum and thermal lag have the same values, the thermal lag is

$$\theta_{T.L.} \tan^{-1} \frac{F_{S_B}}{F_{N_B}} \quad . \tag{70}$$

Define ϕ, to be the angle from the windward ray in the direction of rotation of the body of the resultant force F_R (aerodynamic and ablation induced),

$$F_R = F_N \cos\phi + F_S \sin\phi \tag{71}$$

and

$$\phi = 180 - \tan^{-1} \frac{F_S}{F_N} = 180 - \tan^{-1} \frac{F_{S_B}}{F_{N_o} + F_{N_B}} \quad . \tag{72}$$

Looking at the experimental results, as graphite does not ablate at the test conditions, the forces on the graphite model (F_{N_g} and F_{S_g}) should represent the aerodynamic forces. Thus

$$F_{N_g} = F_{N_o} \tag{73}$$

and

$$F_{S_g} = F_{S_o} \quad . \tag{74}$$

Since F_{S_o} should be zero as the body is pitched, F_{S_g} can be attributed to an anomalous yaw deflection of the body.

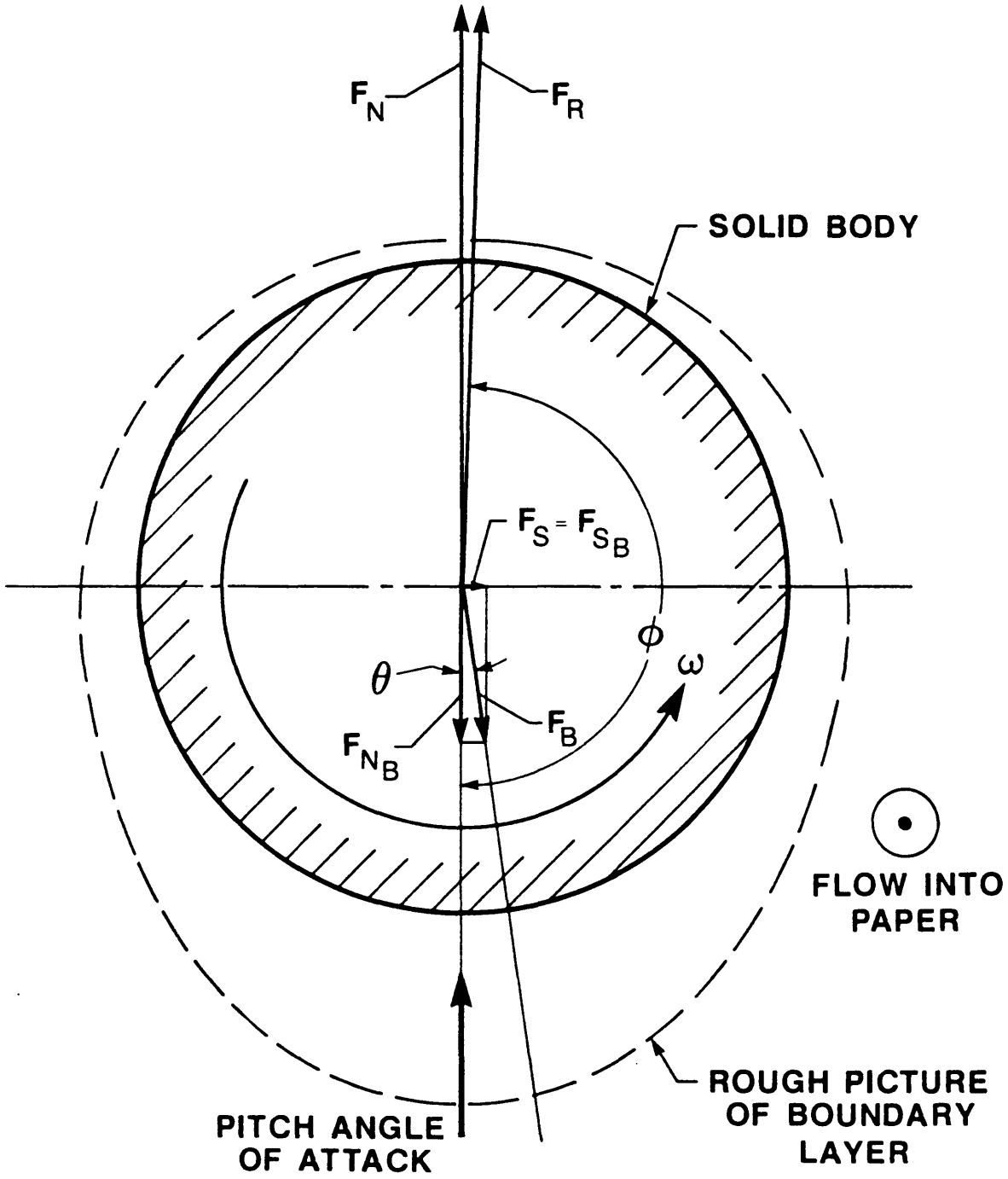

Figure 22. Aerodynamic and ablation induced forces on spinning body at angle of attack.

The forces on the epoxy model on the other hand (F_{N_e} and F_{S_e}) are assumed to include both the ablation and aerodynamic effects. Hence

$$F_{N_e} = F_{N_o} + F_{N_B} \tag{75}$$

and

$$F_{S_e} = F_{S_B} \quad . \tag{76}$$

At zero angle of attack a (Figure F-7), there seems to be a side force present. There cannot be a side force present at zero angle of attack, as the momentum flux off the body due to ablation is the same all around each cross section of the cone. This force is also attributed to deflection of the model. Hence F_{S_B} becomes

$$F_{S_B} = F_{S_{e_o}} + F_{S_e} - F_{S_g} \quad , \tag{77}$$

where $F_{S_{e_o}}$ is the side force of epoxy at zero angle of attack. Then the thermal lag of the epoxy model can be calculated by

$$\theta_{T.L.} = \tan^{-1}\left(\frac{F_{S_{e_o}} + F_{S_e} - F_{S_g}}{F_{N_e} - F_{N_o}}\right) \quad . \tag{78}$$

Figure 23, shows the experimental values of the thermal lag versus the pitch angle.

Using equations (72), (75), and (77) the angle of the resultant force F_R, ϕ may be calculated

$$\phi = 180 - \tan^{-1}\left(\frac{F_{S_{e_o}} + F_{S_e} - F_{S_g}}{F_{N_e}}\right) \quad . \tag{79}$$

Figure 27, shows ϕ versus α, the angle of attack.

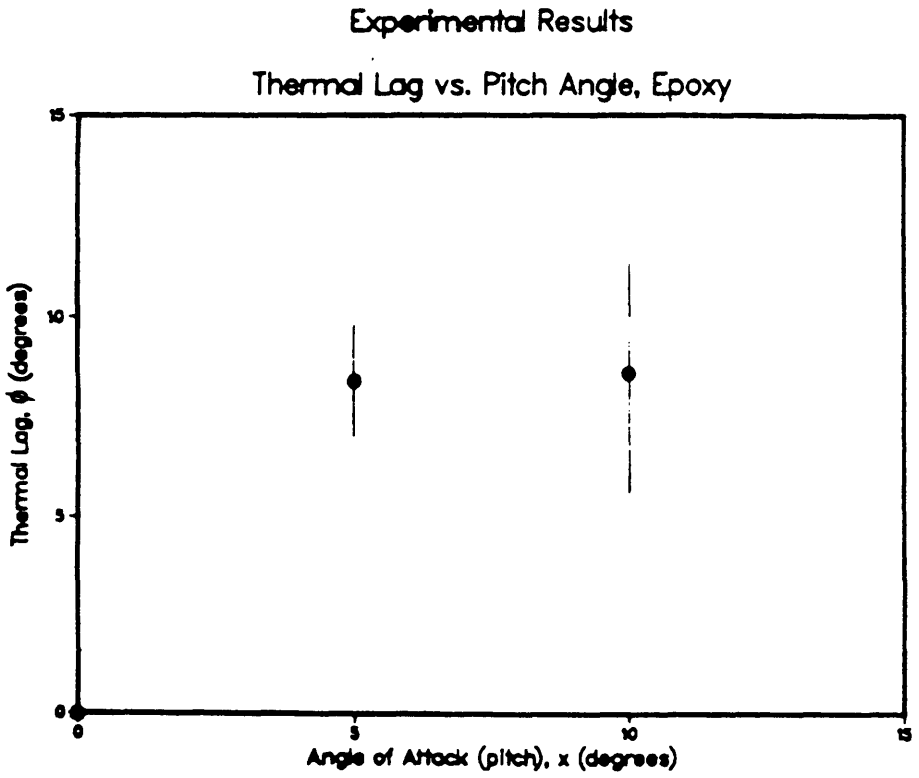

Figure 23. Experimental results. Thermal lag versus pitch angle, Epoxy.

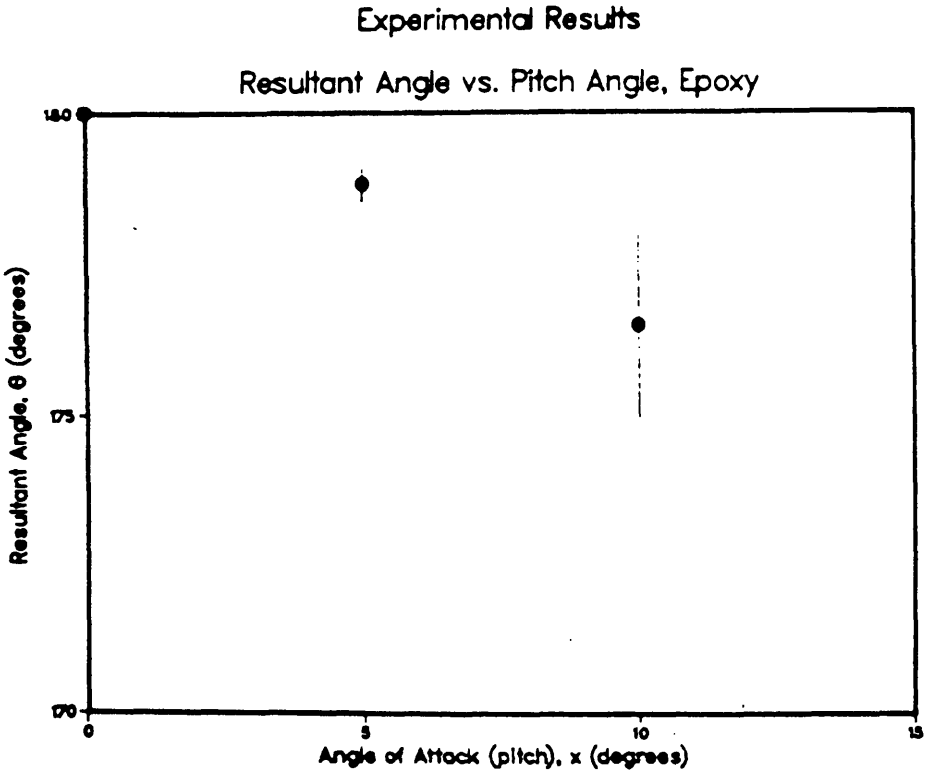

Figure 24. Experimental results. Direction of resultant force versus pitch angle, Epoxy.

It is important to remember that $\theta_{T.L.}$ and ϕ are not the same. The resultant force is merely a few degrees from the position of the aerodynamic force contribution because the ablation force is relatively quite small (Figure 22).

c. COMPARISON OF EXPERIMENTAL AND THEORETICAL RESULTS

The theoretical steady-state analysis indicated that the thermal lag of an ablating rotating body such as epoxy (thermal diffusivity $\alpha = 5.9 \times 10^{-5}$ in^2/s) at experimental spin rates $\frac{\omega r^2}{\alpha}$ of 7.6×10^4 to 3.8×10^5 is 45 degrees from the windward ray in the direction of spin. The same thermal lag was calculated using Teflon ($\alpha = 1.6 \times 10^{-4}$ in^2/s) in a transient computational model. Nevertheless, the experiment seemed to indicate a thermal lag of approximately 8.5 degrees from the windward ray in the direction of spin using an epoxy heat-shield material.

The theoretical thermal lags differed from the experimental by a factor of 5. Possible reasons that may explain this difference are:

1. The assumption that the thermal and momentum lags on the body are equal is incorrect.
2. The experimental results that have been used are not sufficiently accurate, and that planned improvements in the test techniques have to be made before valid results can be obtained.
3. The computational transient conduction model and the analytical steady-state ablation, conduction and radiation model are oversimplifications of the actual experiment.

Chapter 4

Ablation Mass Loss Model

The Teflon and epoxy heat-shield materials ablate at the Arc Jet experimental conditions. Their mass loss rates may be calculated by measuring the heat-shields' recession rates at various axial and circumferential positions along the cone, and multiplying those numbers by the density of the appropriate material. An attempt to model this mass ablation rate has been made and is described in this chapter.

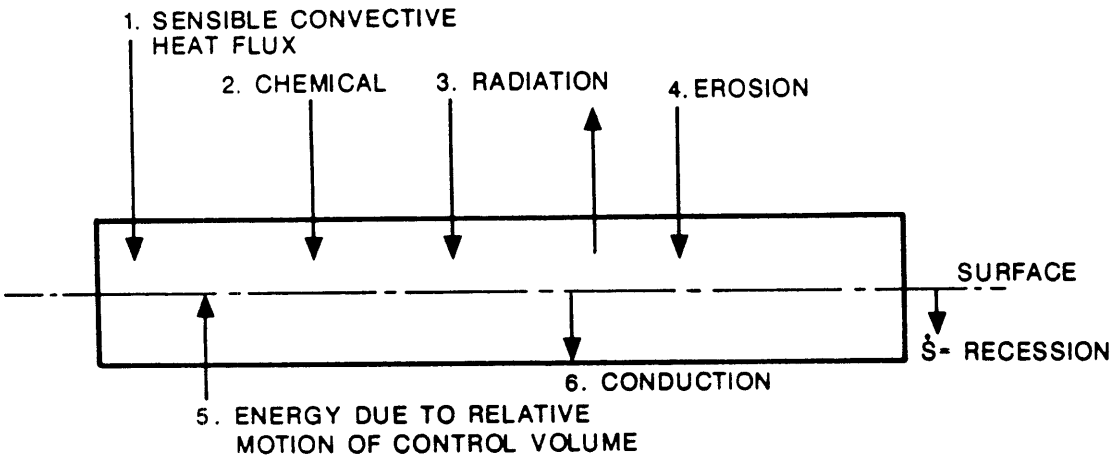

Figure 25. General energy and mass balance model.

Using Figure 25 (References 5 and 28) a general surface energy and mass balance equation may be written.

$$\bar{q}_{conv} + \bar{q}_{chem} - \bar{q}_{rad} + \bar{q}_{e} - \bar{q}_{abl} - \bar{q}_{cond} = 0 \quad . \tag{80}$$

In order to simplify equation (80) a few assumptions need to be made

. The mass loss due to the chemical energy flux ($\bar{q}_{chem}$) has been assumed to be zero. References 5 and 29 and 19 discuss in depth the chemical energy flux, $\bar{q}_{chem}$. This mass loss is determined by the rate at which chemical products and reactants can be diffused and convected through the boundary layer to the reacting surface where the products and reactions are present in chemical equilibrium. $\bar{q}_{rad}$ is the difference between radiation from the surface to the flow ($\bar{q}_{rad\ out}$) and the radiation from the tunnel walls to the surface ($\bar{q}_{rad\ in}$). As the gas in the tunnel is "optically thin," the gas radiation to the body is minimal. Assuming the tunnel does not radiate appreciable energy,

$$\bar{q}_{rad\ in} = 0 \quad . \tag{81}$$

The collision of suspended particles with the surface ($\bar{q}_e$) causing the body to erode may also be neglected whenever the mass loss due to errosion (m_e) is small compared to that due to the gross motion (blowing) of the gas adjacent to the surface (m_{tc} = the thermochemical mass flux).[28]

$$m_e << m_{tc} \quad . \tag{82}$$

Summarizing the assumptions made:

$$\bar{q}_{chem} \simeq 0 \quad , \tag{83}$$

$$\bar{q}_{rad\ in} = 0 \quad \text{then} \quad \bar{q}_{rad} = \bar{q}_{rad\ out} \quad , \tag{84}$$

and

$$m_e << m_{tc} \quad \text{then} \quad \bar{q}_e \simeq 0 \quad . \tag{85}$$

Thus Figure 26 describes the simplified energy and mass balance actually used.

Therefore

$$\bar{q}_{conv} = \bar{q}_{abl} + \bar{q}_{cond} + \bar{q}_{rad\ out} \quad , \tag{86}$$

Using References 5, 28, and 30,

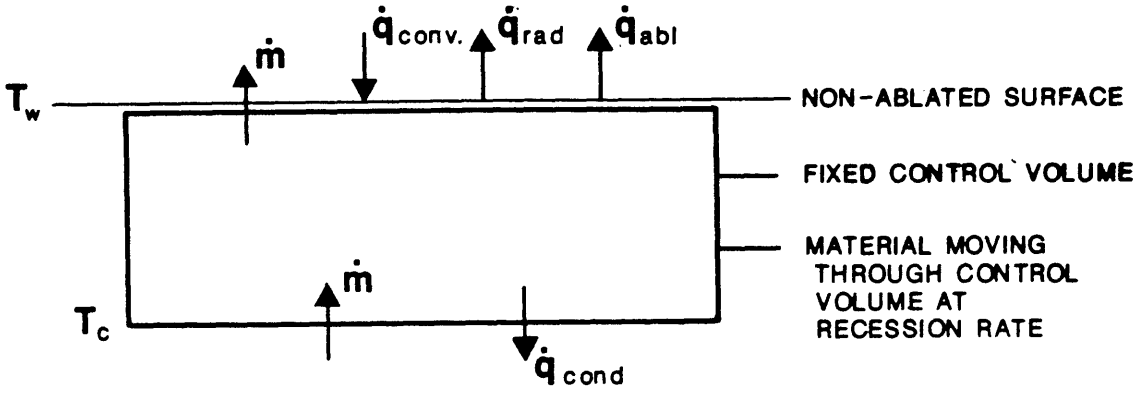

Figure 26. Simplified energy and mass balance model.

$$\overline{q}_{conv} = \frac{H(T_r - T_w)}{Q_1^*} \tag{87}$$

= energy contribution due to convection,

$$\overline{q}_{abl} = \frac{m\ \Delta H_f}{Q_1^*} \tag{88}$$

= energy contribution to surface evaporation,

$$\bar{q}_{cond} = \frac{\dot{m}\, C_p (T_w - T_c)}{Q_1^*} \tag{89}$$

= energy conducted into the body, and

$$\bar{q}_{radout} = \frac{\sigma\, \varepsilon_w (T_w)^4}{Q_1^*} \tag{90}$$

= radiation energy off the surface,

where $Q_1^* = \rho_\infty u_\infty A \Delta H_f^*$, ρ_∞ and u_∞ are the free stream density and velocity repectively, reference area A is allowed to be the Arc Jet tunnel cross-section and ΔH_f^* is the heat of formation of the ablating material. Rewriting equation (86)

$$\frac{m}{\rho_\infty u_\infty A} = \left[\frac{H(T_r - T_w) - \sigma \varepsilon_w (T_w)^4}{\Delta H_f + C_p (T_w - T_c)}\right] \frac{1}{\rho_\infty u_\infty A} \quad , \tag{91}$$

where T_c = temperature of inner surface,

C_p = specific heat at constant pressure,

ΔH_f = heat of formation of material,

T_w = wall temperature,

ε_w = material emissivity,

σ = Stefan-Boltzmann constant,

and H = heat transfer coefficient. (Appendix B contains the dimensional values used in this model.)

Material properties fix the heat of formation (ΔH_f) and the emissivity (ε_w), while the temperature of inner surface (T_c) is assumed. As the body's surface is ablating, the wall temperature (T_w) is the same as the ablation temperature (T_{abl}) of the solid. The specific

heat (C_p) can be determined for a gas containing dissociated oxygen at a free-stream Mach number (M_∞) of 12.5 (from experiment). At free-stream tunnel temperatures (range of 1,400°R to 1,600°R) only the oxygen molecules in the gas dissociate.[31,32] Let

$$T^* = T_{abl} \tag{92}$$

and

$$T_r = \sqrt{P_r}\,(T_o - T_e) + T_e \qquad \text{(Reference 32)} \quad , \tag{93}$$

where T_r = recovery temperature,

while P_r = Prandtl number,

T_o = stagnation temperature,

and T_e = boundary layer edge temperature (Figure 27).

The boundary layer edge temperature is

$$\frac{T_e}{T_\infty} = \frac{P_e}{P_\infty}\,\frac{\rho_e}{\rho_\infty} \quad . \tag{94}$$

$\frac{P_e}{P_\infty}$, $\frac{\rho_e}{\rho_\infty}$ and $\frac{M_e}{M_\infty}$ are found from cone tables.[34] The stagnation temperature is

$$\frac{T_o}{T_e} = 1 + \frac{\gamma - 1}{2} M_e^2 \quad . \tag{95}$$

The stagnation and recovery temperatures calculated using these perfect gas solutions (Appendix B) are larger than if T_o and T_r had been determined using real high temperature gas properties.

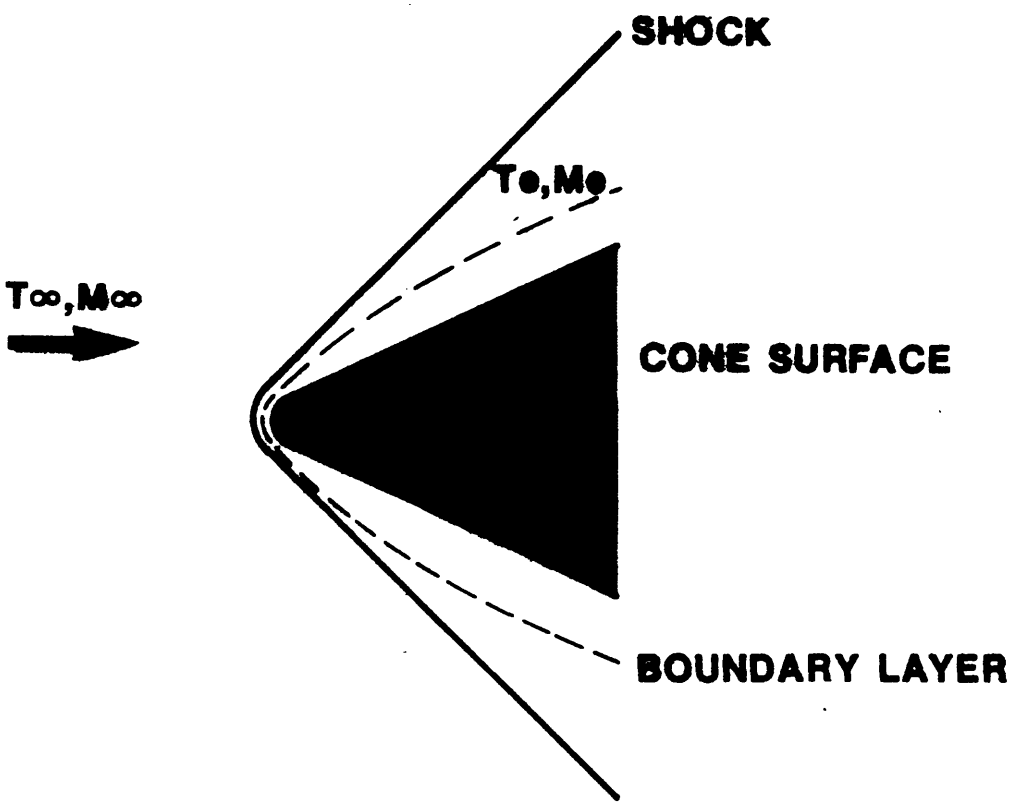

Figure 27. Boundary layer and shock on a cone in Supersonic Flow.

Using a Prandtl number of 0.72 for the Arc Jet conditions,[33] the recovery temperature and thus enthalpy may be calculated. Hence in order to calculate the mass loss (equation (91)) merely the heat transfer coefficient remains to be defined.

Assuming a laminar flow, a constant pressure solution, and a Lewis number of unity,

$$H = \sqrt{3}\,(0.332)\,k \sqrt{P_r^* U_e \frac{\rho^* \mu^*}{\mu^2}} \frac{1}{\sqrt{x}} \tag{96}$$

where $\sqrt{3}$ = Mangler factor for cones,[35] the Prandtl number (P_r*), density (ρ*), and viscosity (μ*) are evaluated at the reference material ablation temperature (T*), and u_e is assumed to be 99% of the freestream velocity.[34]

To determine the heat transfer coefficient, the edge viscosity μ_e is obtained from Sutherland's Law,[36]

$$\mu_e = \frac{2.27\, T_e^{3/2}}{T_e + 198.6} \left[lb_f - sec/ft^2\right] \quad . \tag{97}$$

Hence the mass loss of a heat-shield material may be of the form

$$m_{material} \propto \frac{1}{\sqrt{x}} \quad , \tag{98}$$

where x is the axial distance from the tip of a sharp cone toward its base. Of course, the sharp cone assumption clearly prevents comparison near any blunt nose stagnation region.

This model has been applied to Teflon and epoxy heat shields. The results are compared for the two materials (Figures 28 and 29).

The theory seems to agree with the experimental data at the rear of the body, whereas the results closer to the nose seem to diverge by an order of magnitude from the test for the two heat shields. In nondimensionalizing the experimental mass loss

$$\frac{m}{\rho_\infty U_\infty A} \sqrt{\frac{x}{L}} \tag{99}$$

term is chosen.

Despite the agreement close to the rear of the body, the model clearly is not adequate. The assumption of a sharp cone in laminar flow undergoing steady-state ablation at the surface does not simulate the experiment with any accuracy. In order to create a more accurate model of the test a blunt cone should be assumed such that stagnation region effects are included.[5]

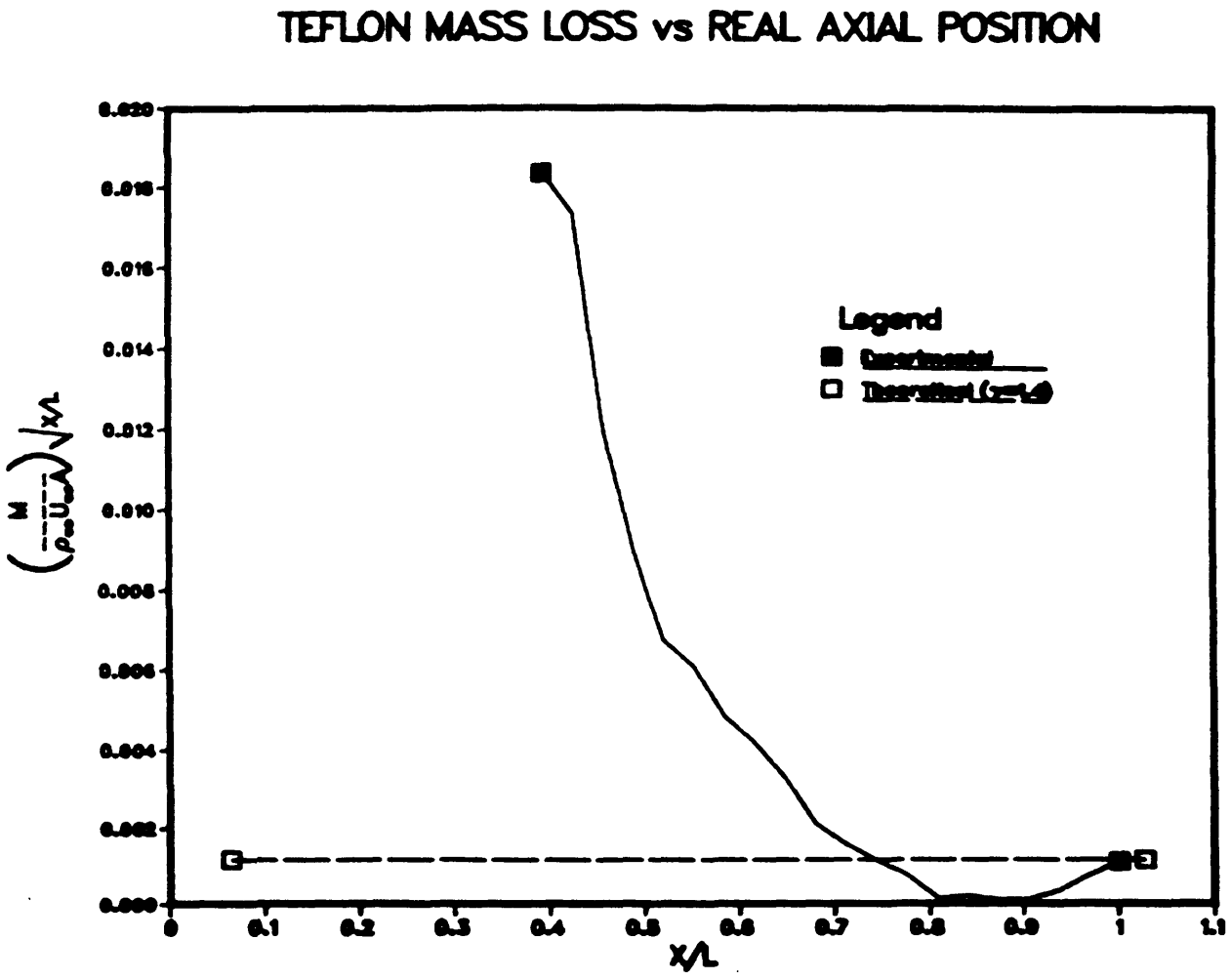

Figure 28. Comparison of experimental and theoretical ablation mass loss, Teflon.

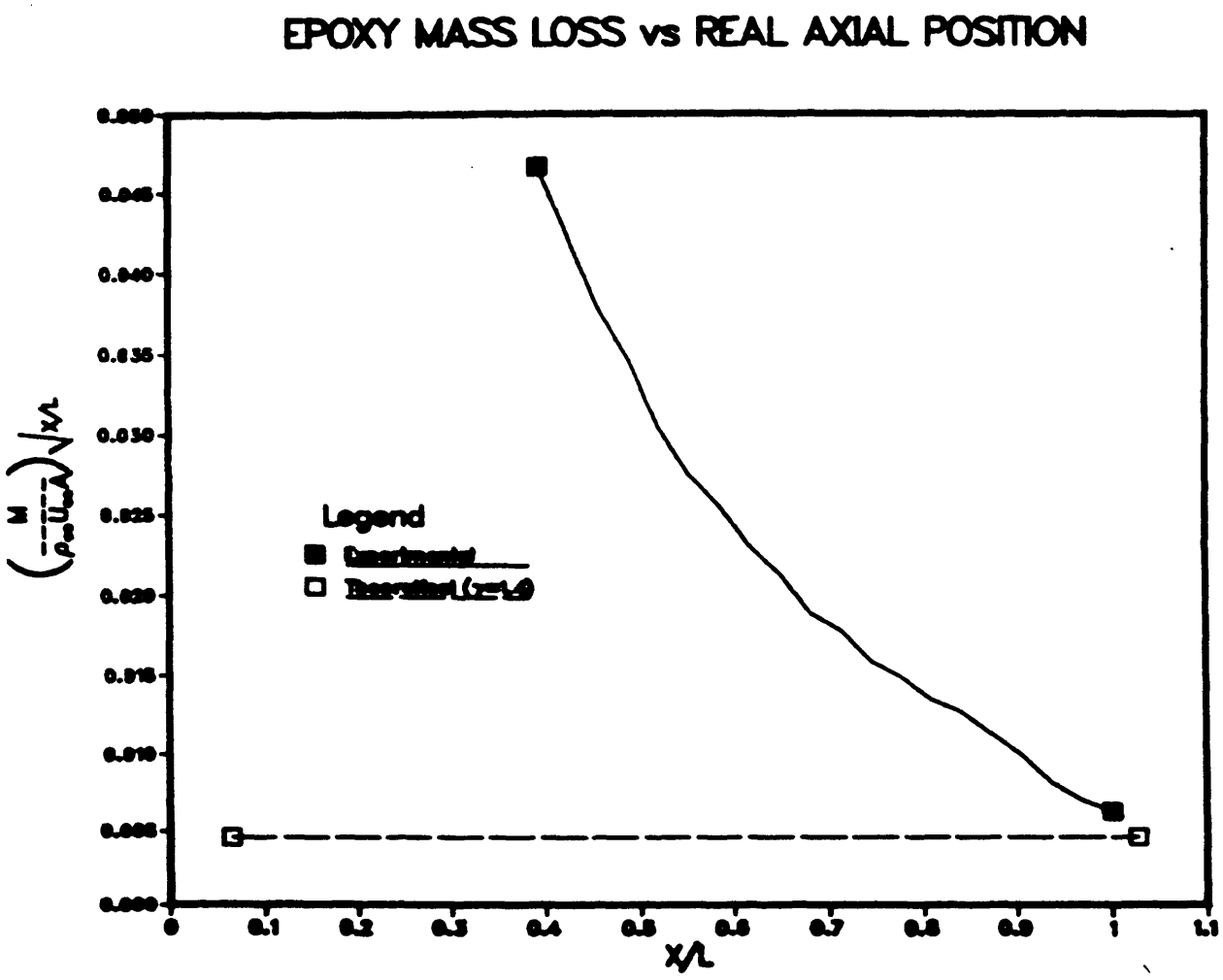

Figure 29. Comparison of experimental and theoretical ablation mass loss, Epoxy.

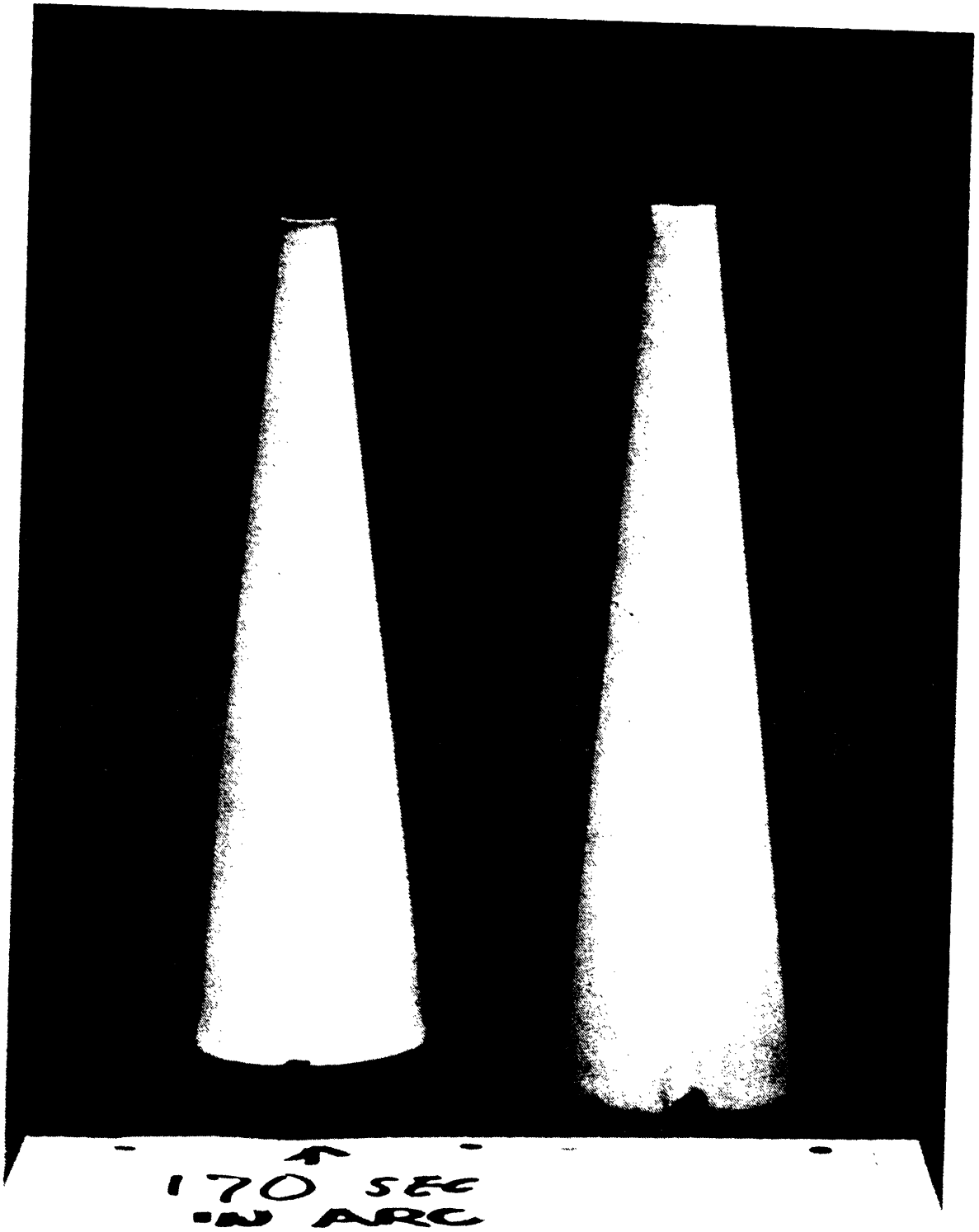

Figure 30. Teflon model before and after exposure to Arc Jet.

Chapter 5

Conclusions and Summary

Force and thermal effects have been studied for rotating ablating bodies in high-speed atmospheric flight undergoing non-uniform heating. Two models have been developed to calculate a thermal-lag angle assuming the heating is sinusoidal in form, while another model describes the ablation mass loss off the axi-symmetric body. A thermal-lag angle ($\theta_{T.L.}$) was defined as the angle from the windward ray (in the direction of rotation) at which the highest surface temperature is located.

These models were compared to the results obtained from a 20-MW Arc Jet in which M.I.T. Lincoln Laboratory had conducted preliminary tests of various heat-shield materials (epoxy, Teflon, and graphite) using a hydrostatic gas bearing wind-tunnel balance. While the balance operated successfully and provided the needed sensitivity, other aspects of the experiment lacked the precision to provide the needed data for checking the models developed here. Experimental aspects needing improvement include a more rigid model support with a model spin system that does not affect balance readings and provides constant spin. Of the available data only the epoxy model yielded a side force estimate and could be compared to the thermal-lag models.

The first of the two thermal-lag models represents a steady-state simplification of a transient problem in which the heat input contributes to conduction into, ablation from and radiation off the body. The second describes a transient computational model in which all the heat input on the surface is conducted into the solid. In the computational method the lag is a function of spin rate $\frac{\omega r^2}{\alpha}$. In the analytical solution the lag is influenced by $\frac{\omega r^2}{\alpha}$, an ablation and a radiation term. Nevertheless the results of the two models are practically identical for the angular velocities at which the bodies spin in the 20-MW Arc Jet force test.

At zero spin, the highest heating is at the windward ray, the surface temperature at that location rises to a maximum compared to other areas on the surface, and $\theta_{T.L}$ is zero. In this case of a rotating vehicle, the peak temperature, thus the thermal lag, is displaced

to one side of the body from the windward ray. The analytical steady-state model uses an ablation mass loss rate[17] for an epoxy heat-shield material to determine that the thermal lag asymptotes to 45° as the spin rate increases. A computational transient model using SINDA also reaches a 45° thermal-lag angle.

In order to compare the 20-MW Arc Jet force data to the theoretical models and calculate the experimental thermal lag, an important assumption was required. The momentum lag (the angle from the windward ray in the direction of rotation at which the momentum flux from the body is the largest) is assumed to be identical to the thermal lag. The logic behind this assumption is that the area on the surface with the highest temperature has the greatest ablation, and thus the largest momentum from the body. Using this assumption and considering that the force on the ablating rotating body in the wind tunnel is the sum of an aerodynamic and an ablation induced term, calculating the angle from the windward ray of the latter force determines the lag.

At the conditions at which the Arc Jet operates, graphite ($\alpha = 1.3 \times 10^{-2}$ in^2/s) may be considered a non-ablating material. Then the forces on it may be solely attributed to the aerodynamics. This simplifies finding the ablation induced force on epoxy ($\alpha = 5.9 \times 10^{-5}$ in^2/s). It is the difference between the total force on the epoxy heat shield and that of the graphite model. The scatter in the Teflon ($\alpha = 1.6 \times 10^{-4}$ in^2/s), due to poor annealing of the material caused the heat shield to change shape. This was considered enough to suggest disregarding those results.

For angles of attack (pitch) of five and ten degrees, a thermal-lag angle of approximately 8.5 degrees was calculated for the experiment. The theoretical model thermal lag of 45 degrees is larger by a factor of 5. There are three major reasons for which this difference exists:

-The assumption that the thermal and momentum lags on the body are equal may be incorrect.

-The gas-bearing wind-tunnel balance is the first of its kind, and the experimental results are not sufficiently accurate. Further improvements

in the test techniques need to be made in order to measure thermal lag adequately.

-The computational transient conduction model and the analytical ablation, conduction and radiation model are oversimplifications of the actual experiment.

The ablation mass loss of the arc jet test was also estimated. Although the theoretical mass loss agreed with the experiment reasonably well close to the rear of the body, the model was not adequate overall. It is realized that an assumption of a sharp cone in laminar flow undergoing steady-state ablation at the surface is much too simplifying.

It is extremely important to note that the thermal lag is not the angle from the windward ray of the resultant force on the body, but only of the ablation induced force. Although the thermal lag may be large the resultant force is merely a few degrees from the position of the aerodynamic force contribution. The ablation force is relatively small, and the influence of any thermal lag that may be present may not necessarily be a dominant effect.

It is recommended that additional experiments correcting the difficulties encountered in the preliminary tests be conducted, such that the validity of the models may be assessed.

References

[1]Zahm, A. F., "Superaerodynamics," Journal of the Franklin Institute, Vol. 217, pp. 153-166 (January 1934).

[2]Tsien, H. S., "Superaerodynamics, Mechanics of Rarefied Gases," Journal of the Aeronautical Sciences, Vol. 13, pp. 653-664 (December 1946).

[3]Adams, M. C. and Probstein, R. F., "On the Validity of Continuum Theory for Satellite and Hypersonic Flight Problems at High Altitudes," Jet Propulstion, Vol. 6, pp. 86-89 (February 1958).

[4]Boundary-Layer Theory, Schlichting, H., Seventh Edition, McGraw Hill Book Company, Incorporated (1979).

[5]Viscous Hypersonic Flow, Dorrance, W. H., McGraw Hill Book Company, Incorporated (1963).

[6]Heat Transfer in Structures, Schuh, H., Pergamon Press (1965).

[7]Supersonic Flow, Chemical Processes and Radiative Transfer, Olfe, D. B., and Zakkay V., Pergamon Press Book (1964).

[8]Hurwicz, H., "Thermal Protection Systems," Air Force Materials Laboratory, ML-TDR-64-82 (January 1965).

[9]Munson, T. R. and Spinkler, R. J., "Transient Thermal Behavior of Decomposing Materials, Part 1: General Theory and Application to Convective Heating," IAS Paper No. 62-30, 30th IAS Annual Meeting, New York (January 1962).

[10]Kratsch, K. M. Hearne, L. F., and McChesney, R. R., "Thermal Performance of Heat Shield Composites During Planetary Entry," AIAA-NASA National Meeting, Palo Alto, California (October 1963).

[11]Arne, C. L., "Ablative Materials Subject to Combustion and Thermal Radiation Phenomena," Douglas Paper No. 1851 (January 1964).

References (Continued)

[12]Kendall, R. M., Rindal R. A., and Bartlett, E. P., "A Multicomponent Boundary Layer Chemically Coupled to an Ablating Surface," AIAA Journal, Vol. 5, No. 10 (June 1967).

[13]Waterfall, A. P., "Effect of Ablation on the Dynamics of Spinning Re-Entry Vehicles," Journal of Spacecraft and Rockets, Vol. 6, pp. 1038-1044 (September 1969).

[14]Ragsdale, W. C. and Horanoff, E. V., "Investigation of a Side Force Due to Ablation," AIAA Journal, Vol. 16, pp. 1010-1011 (May 1978).

[15]Morrison, A. M. and Fiscina, C., "Effects of Spin and Mass Addition on High-Angle-of-Attack Re-entry," Journal of Spacecraft, Vol. 22, pp. 68-73 (January 1982).

[16]Vaughn, H. R. and Reiss, G. E., "A Magnus Theory," AIAA Journal, Vol. 11, pp. 1396-1403 (October 1973).

[17]Morrison, A. M. and Fiscina C., "Effects of Spin and Mass Addition on High-Angle-of-Attack Re-entry," Journal of Spacecraft, Vol. 22, No. 1 (1982).

[18]Naval Surface Weapons Center, "Handbook of Inviscid Sphere-Cone Flow Fields and Pressure Distributions," Vol. 1, NSWC Technical Report (December 1975).

[19]Wilson, R. E., Carlson, D. L., and Minell, C. L., "Development of the Thermal/Ablation Model for a Passive Decoy Epoxy Material," Acurex Corporation, Aerotherm Division, Document No. 8800-85-0127 (May 1985).

[20]Fay, J.A. and Riddell, F. R., "Theory of Stagnation Point Head Transfer in Dissociated Air," Journal of Aeronautical Sciences, Volume 25 (February 1958).

[21]Advanced Calculus for Applications, Second Edition, Francis B. Hildbrand, Prentice-Hall Incorporated (1976).

[22]Sinda Manual, 1983/ANSI, NASA.

[23]Heat Transfer, J. P. Holman, McGraw-Hill Book Company (1976).

[24]Conduction Heat Transfer, Schneider, P. J., Addison-Wesley Publishing Company, Incorporated, Reading, Massachusetts (1955).

[25]Haldeman, C. W. and Weinberg, A. D., Personal Communication, ["A viable alternative to strain gauge wind tunnel force balances using conventional Hydrostatic Bearing Technology," future AIAA Journal Report.].

[26]Gas Lubricated Bearings, N. S. Grassam and J. W. Powell, Butterworths, London, pp. 110-139, 181-217, 265-267 (1964).

[27]Aeroelasticity, R. L. Bisplinghoft, H. Ashley, and R. L. Halfman, Addison-Wesley Publishing Company, Incorporated, pp. 15-23 (Copyright 1955).

[28]Acurex Corporation, Passive Nosetip Technology (PANT II) Program, "Computer User's Manual: ABRES Shape Change Code (ASCC)," Vol. 2 (October 1976).

[29]Kendall, R. M. Rindal, R. A., and Bartlett, E. P., "A Multi-component Boundary Layer Chemically Coupled to an Ablating Surface," AIAA Journal, Vol. 5, No. 6 (June 1967).

[30]Lees, L., "Convective Heat Transfer with Mass Addition and Chemical Reactions," Combustion and Propulsion, Third AGARD Dolloquium, Pergamon Press, New York (March 1958).

[31]Kemp, N. H., Rose, P. H., and Detra, R. W., "Laminar Heat Transfer Around Blunt Bodies in Dissociated Air," Avco Everett Research Laboratory, Journal of Aerospace Science, Vol. 26 (1959).

[32]Hansen, C. F., "Approximations for the Thermodynamic and Transport Properties of High-Temperature Air," NASA Technical Report R-50 (1959).

[33]Kays, W. M. and Crawford, M. E., Convective Heat and Mass Transfer, Second Edition, McGraw-Hill Book Company.

[34]Kopal, Z., "Tables of Supersonic Flow Around Cones," Technical Report #1, Massachusetts Institute of Technology, Cambridge, MA (1947).

[35]Hayes, W. D. and Probstein, R. F., Hypersonic Flow Theory, Academic Press (1959).

[36]Jakob, M. Heat Transfer, Vol. 1, John Wiley & Sons, Incorporated (1962).

APPENDIX A

Model of Heating Rate on Rotating Ablating Body at Angle of Attack

From Reference 31, the relationship between the heat transfer coefficient and pressure on a body may be described by

$$H \propto \sqrt{P} \quad .$$

Using the NSWC inviscid sphere-cone flow fields and pressure distribution calculations[18] for a cone with a half angle of 5.5 degrees and a Mach number of 10, the heat transfer coefficients around the cone at angle of attack of 5 and 10 degrees may be obtained. Figures A-1 and A-2 are plots of those values.

In attempting to model the heat transfer coefficient of rotating ablating axi-symmetric bodies at angle of attack, a sinusoidal heating rate distribution is used. This distribution is of the form

$$Q(\theta) = Q_o (1 + \varepsilon \cos \theta) \quad ,$$

where θ is an angular co-ordinate, Q_0 is the heating rate at zero angle of attack, and ε is an empirical parameter which describes the variation of the angle of attack ($\varepsilon = 0$, $Q = Q_0$). Using the relationship between the heat transfer coefficient and pressure on a body, ε is calculated to be 0.66 and 0.45 for angles of attack of 10 and 5 degrees respectively. An ε of 0.5 has been used to model the heat transfer coefficient for simplicity. As can be seen from Figures A-1 and A-2, using $\varepsilon = 0.5$ is a reasonable model by comparison to the NSWC cone tables.

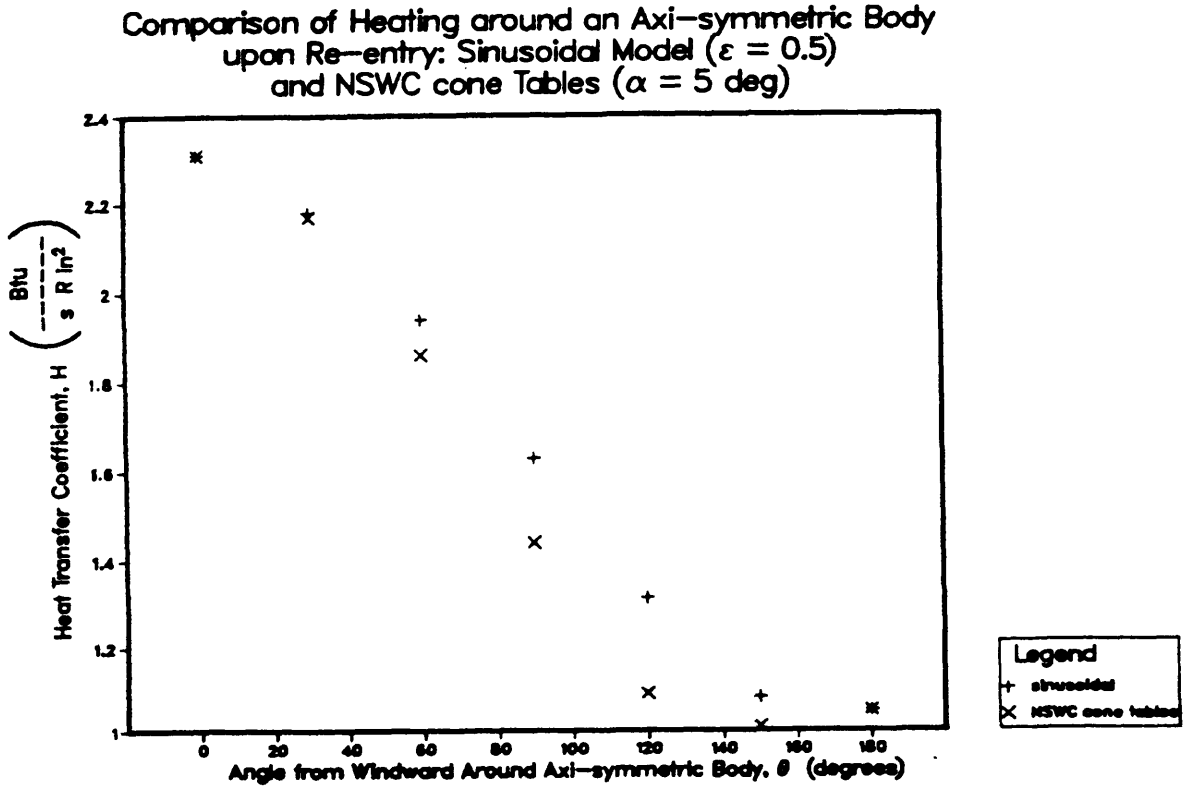

Figure A-1. Comparison of heating rate distributions, sinusoidal model versus NSWC cone tables ($\alpha = 5°$).

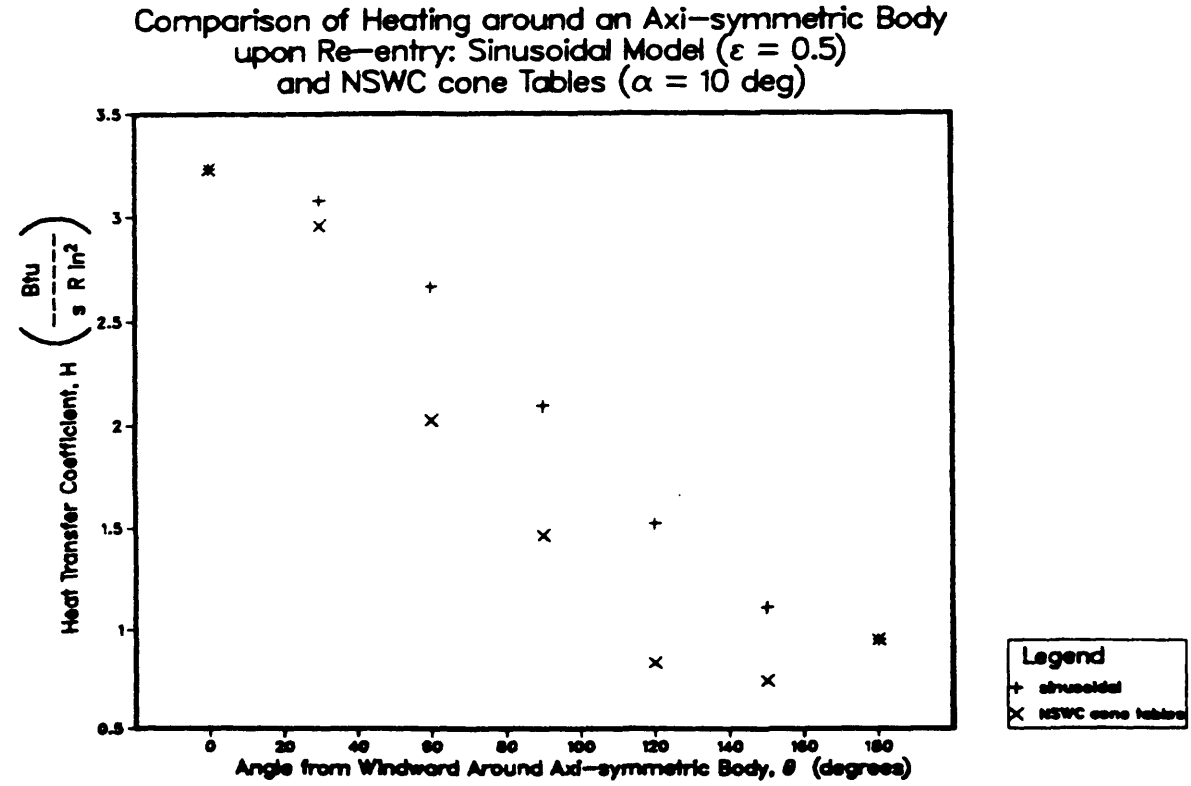

Figure A-2. Comparison of heating distribution, sinusoidal model versus NSWC cone tables ($\alpha = 10°$).

APPENDIX B

Physical Properties and Test Conditions

$H = \frac{1.5 \times 10^{-6}}{\sqrt{x}}, \frac{5.47 \times 10^{-7}}{\sqrt{x}} \frac{Btu}{s\ °R\ in^2}$ for epoxy, teflon

where x is in inches

$h = 0.25$ in

$\Delta H_f^* = 200, 643 \frac{Btu}{lb_m}$ for epoxy, teflon

$k^* = 1.4 \times 10^{-5}, 1.25 \times 10^{-3}, 3.34 \times 10^{-6} \frac{Btu}{in\ s\ °R}$ for epoxy, graphite, teflon

$L = r = 1.5$ in

$M_e = 10.25$, for $\psi = 5.5°$

$M_\infty = 12.5$

M_1 (epoxy) $= 2.536 \times 10^{-5} \frac{in}{s}$

M_2 (epoxy) $= 0.0022387\ °R^{-1}$

$\frac{P_e}{P_\infty} = 3.3466$, for $\psi = 5.5°$

$P_r = 0.72$

$Q^* = \frac{k^* T^*}{L} = 0.0224, 0.0040 \frac{Btu}{s\ in^2}$ for epoxy, teflon

$Q_o = 0.217 \frac{Btu}{s\ in^2}$

$Q_{cw} = 0.243 \frac{Btu}{s\ in^2}$

$r = 1.5$ in

$T_c = 530\ °R$

$T_e = 2180\ °R$

$T_o = 36{,}535\ °R$

$T_r = 31{,}332\ °R$

T^* = 2,400, 1,800 °R for epoxy, teflon

where T^* is a reference material ablation temperature

$u_e = 0.99\, u_\infty$ (Reference 34)

u_∞ = 12,500 $\frac{ft}{s}$, where speed of sound is assumed to be, a_∞ = 1,000 $\frac{ft}{s}$

α^* = 5.9×10^{-5}, 1.3×10^{-2}, 1.6×10^{-4} $\frac{in^2}{s}$ for epoxy, graphite, teflon

$\gamma = 1.4$

$\varepsilon = 0.5$

$\varepsilon_w^* = 0.8$ for both epoxy and teflon

μ^* = 207, 203 $\frac{lb_m}{in\ s}$ for epoxy, teflon

ρ^* = 0.03302, 0.0625, 0.0850 $\frac{lb_m}{in^3}$ for epoxy, graphite, teflon

$\frac{\rho_e}{\rho_\infty} = 2.3030$

$\sigma = 6.94 \times 10^{-15}$ $\frac{Btu}{s\ in^2\ °R^4}$

$\psi = 5.5°$

Ω (experimental range, epoxy) = $\frac{\omega r^2}{\alpha}$ = 7.6×10^4 to 3.8×10^5

ω (experimental range) = 4π to 20π s^{-1}

APPENDIX C

Flow Chart of SINDA Operations

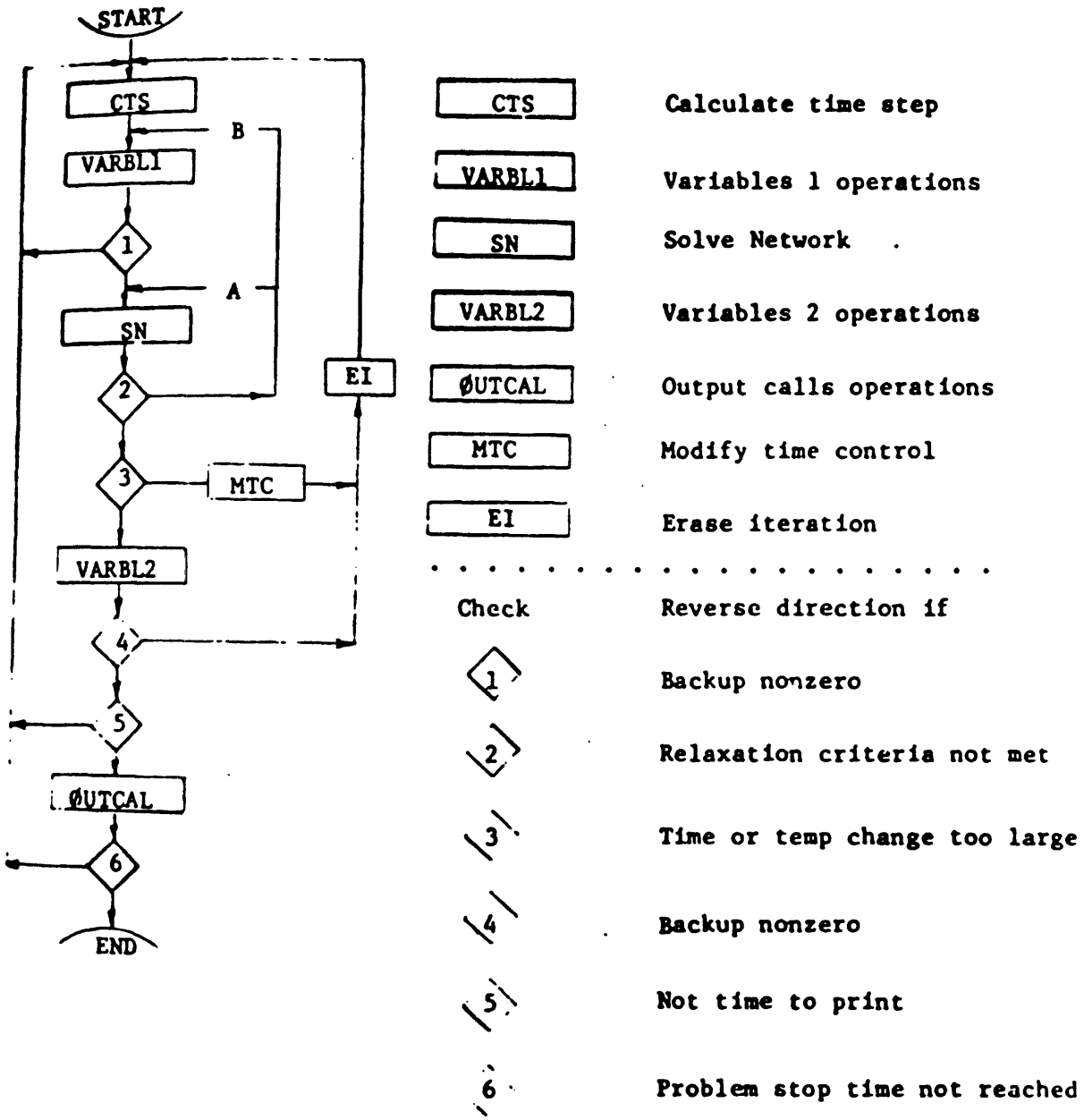

Figure C-1. Flow Chart of SINDA Operations.

APPENDIX D

Influence Coefficient Matrix

$$C = \begin{bmatrix} -2.458 & -0.012 & -0.053 & -0.013 \\ 0.002 & 2.526 & 0.029 & 0.086 \\ 0.045 & -0.096 & 2.586 & 0.045 \\ -0.030 & -0.058 & -0.005 & -2.666 \end{bmatrix}$$

The off-diagonal terms in the influence coefficient matrix, calculated from calibration data of a hydrostatic gas bearing wind-tunnel balance, are small compared to the diagonal terms, indicating a good degree of balance linearity.

APPENDIX E

Raw Balance Calibration Data

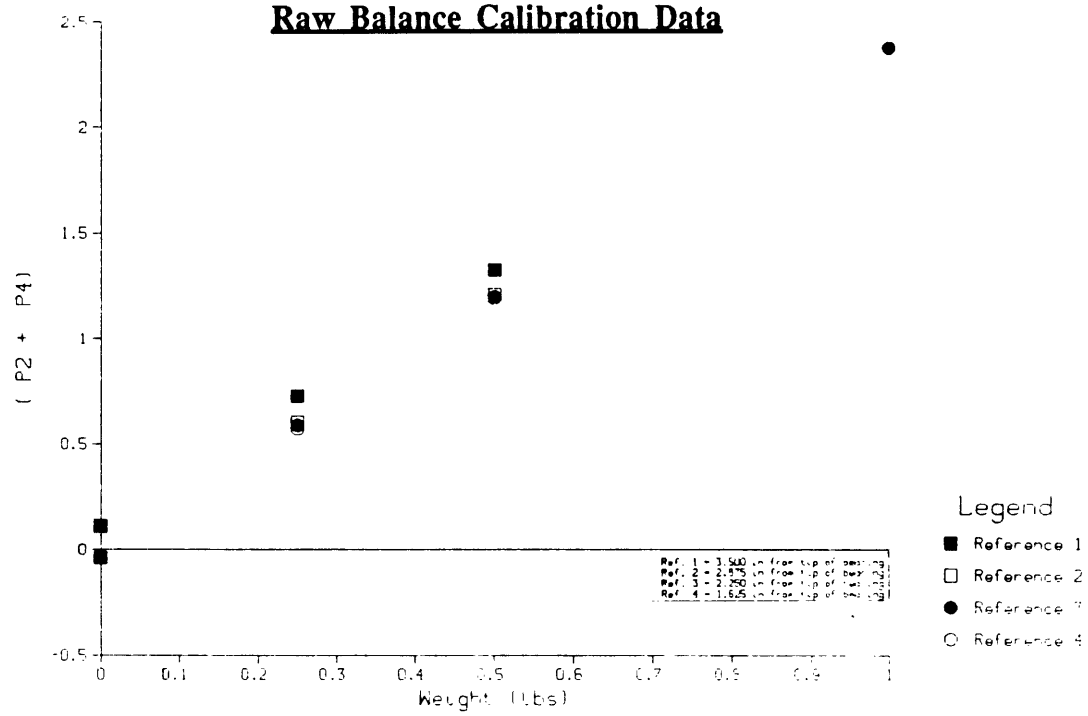

Figure E-1. Raw Side Force Calibration

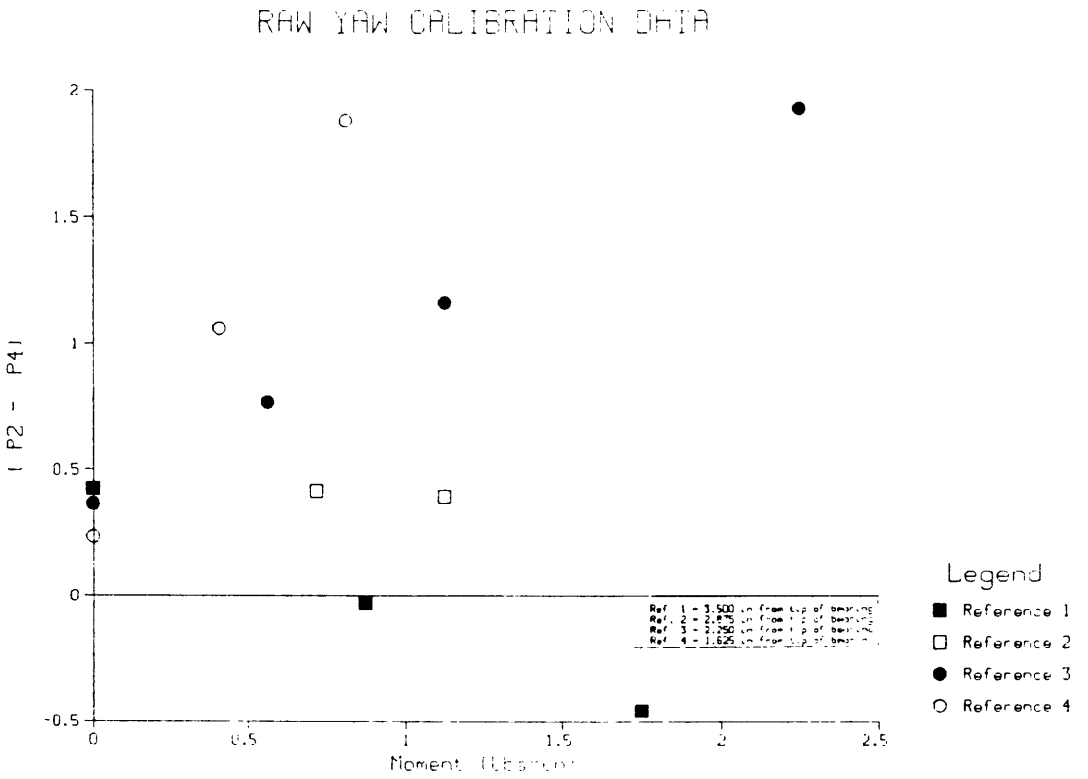

Figure E-2. Raw Yaw Calibration Data.

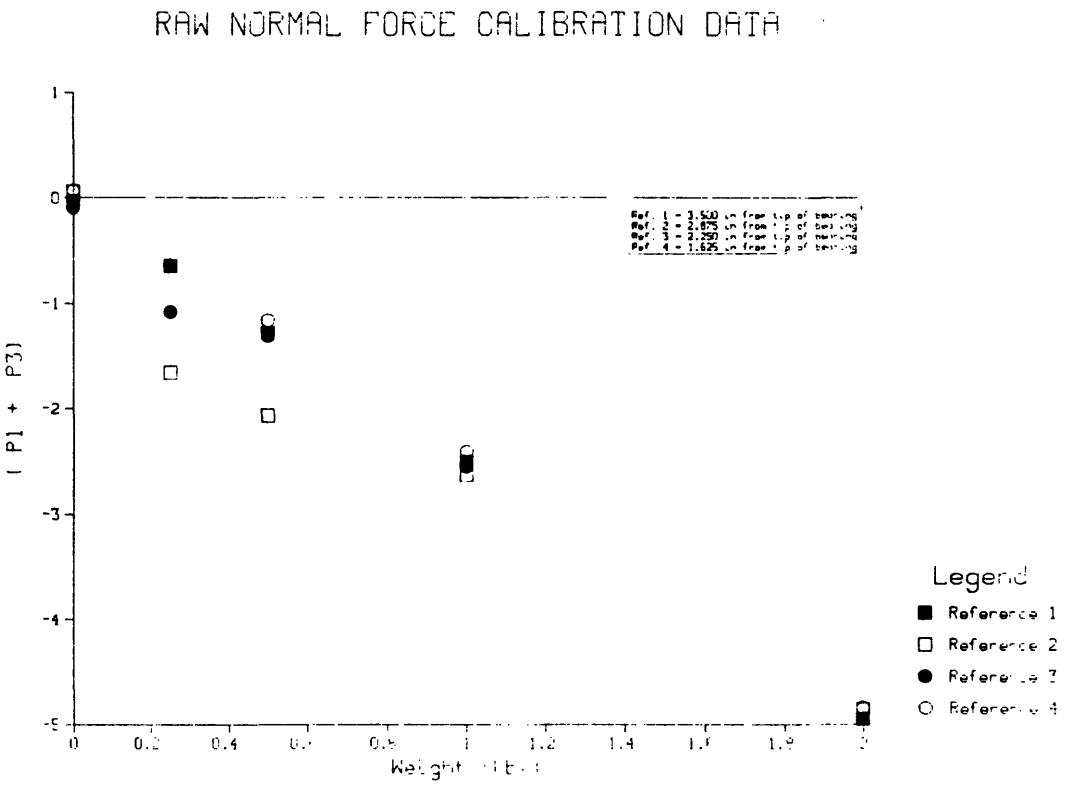

Figure E-3. Raw Normal Force Calibration Data.

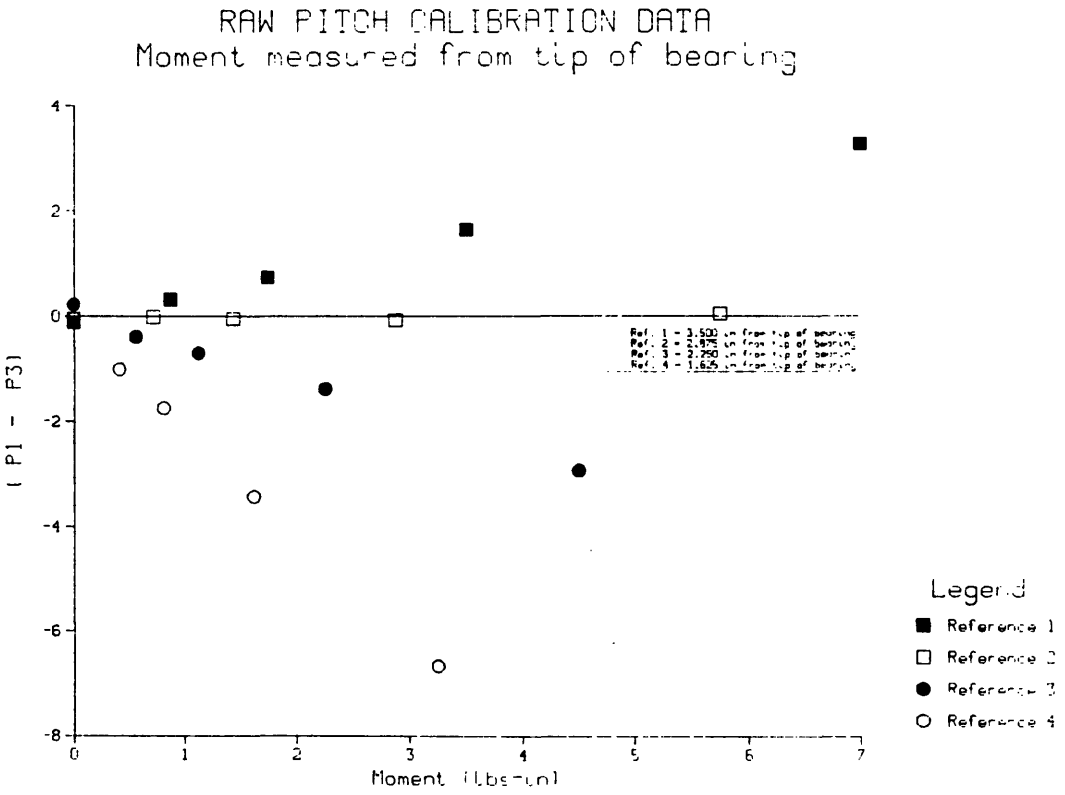

Figure E-4. Raw Pitch Calibration Data.

APPENDIX F

Arc Tunnel Force and Moment Data for Pitch and Yaw — Graphite, Epoxy, and Teflon

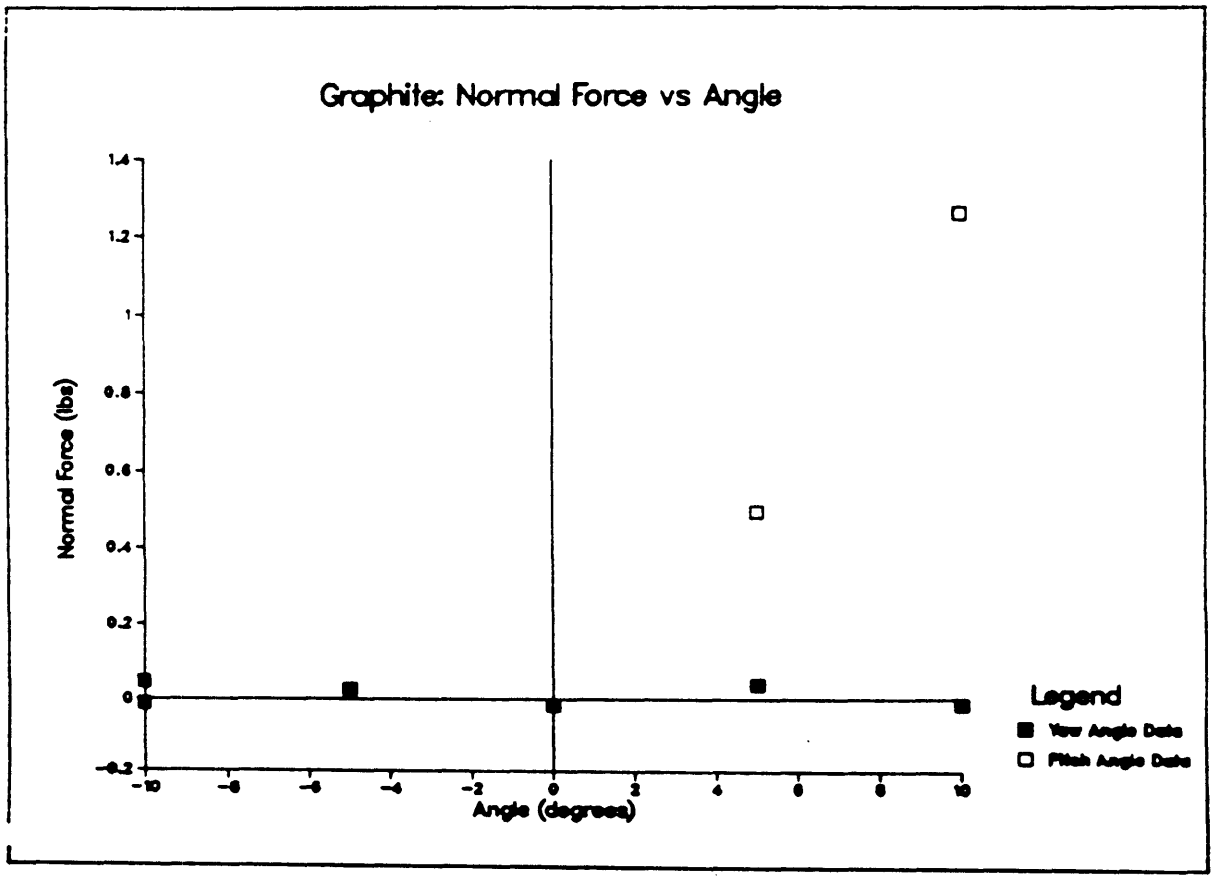

Figure F-1. Graphite — Normal force versus Angle.

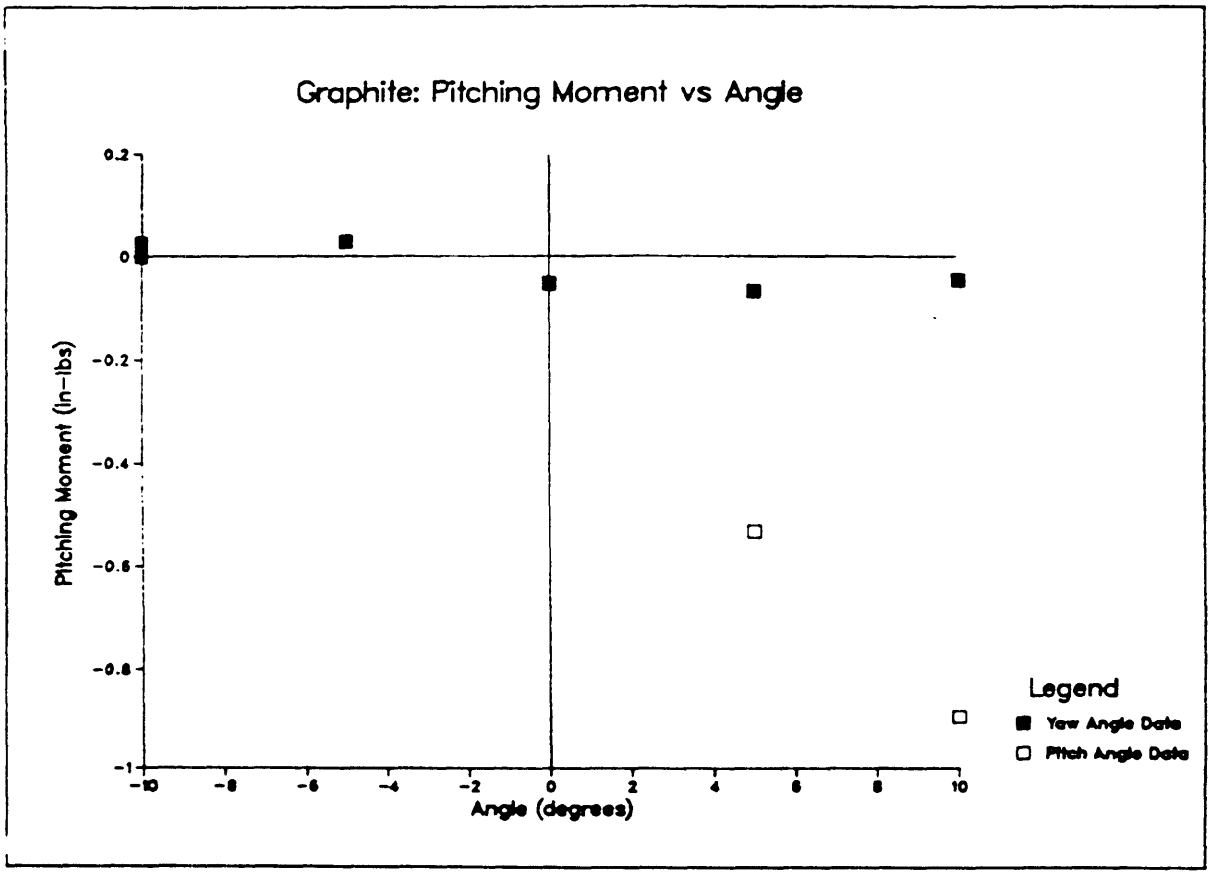

Figure F-2. Graphite — Pitching moment versus angle.

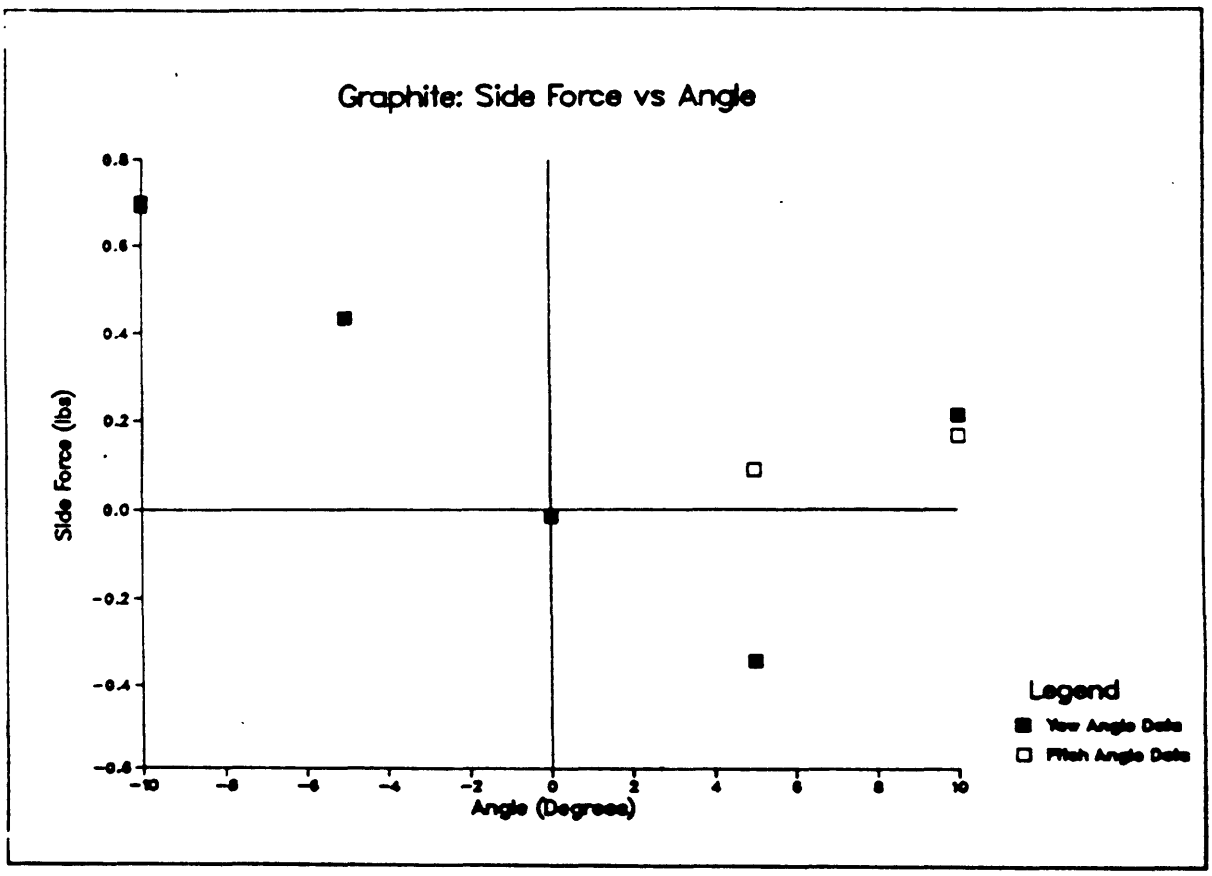

Figure F-3. Graphite — Side force versus angle.

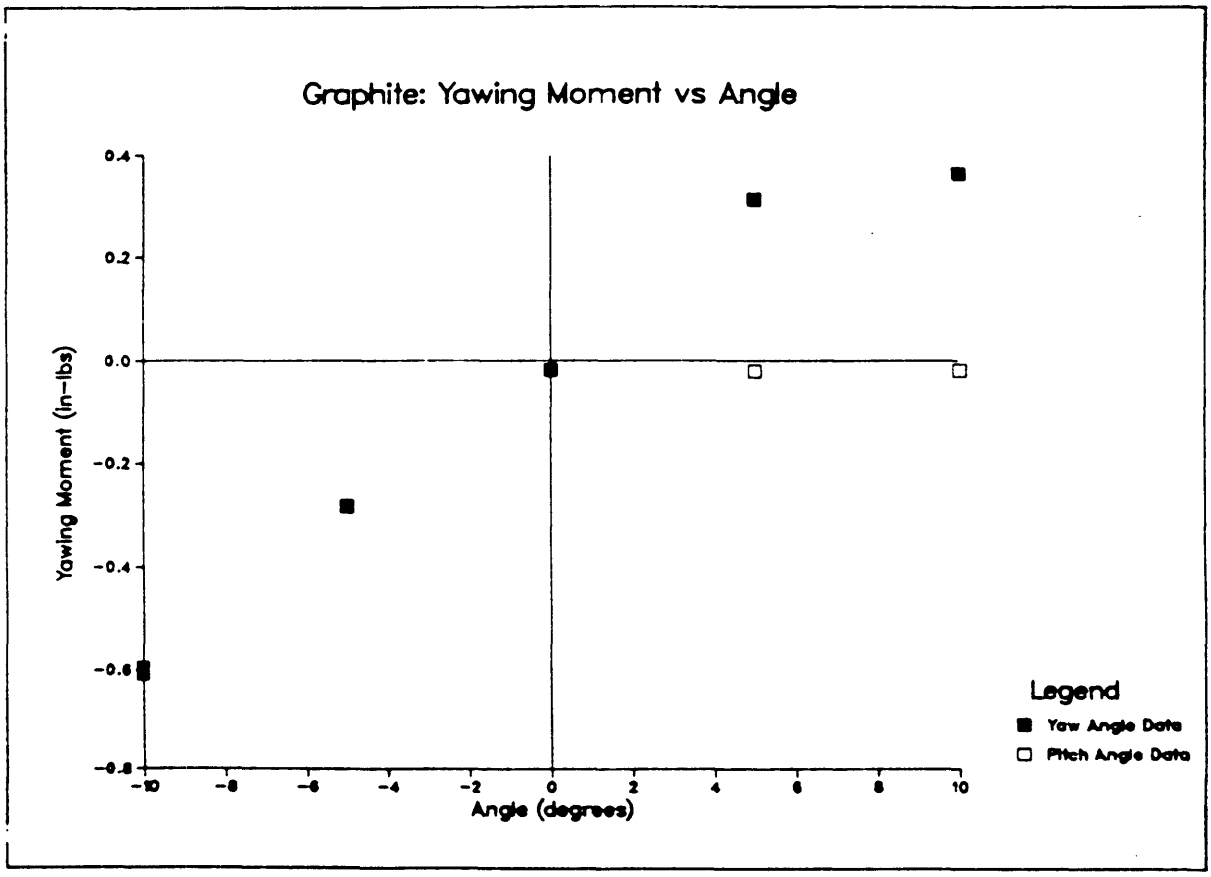

Figure F-4. Graphite — Yawing moment versus angle.

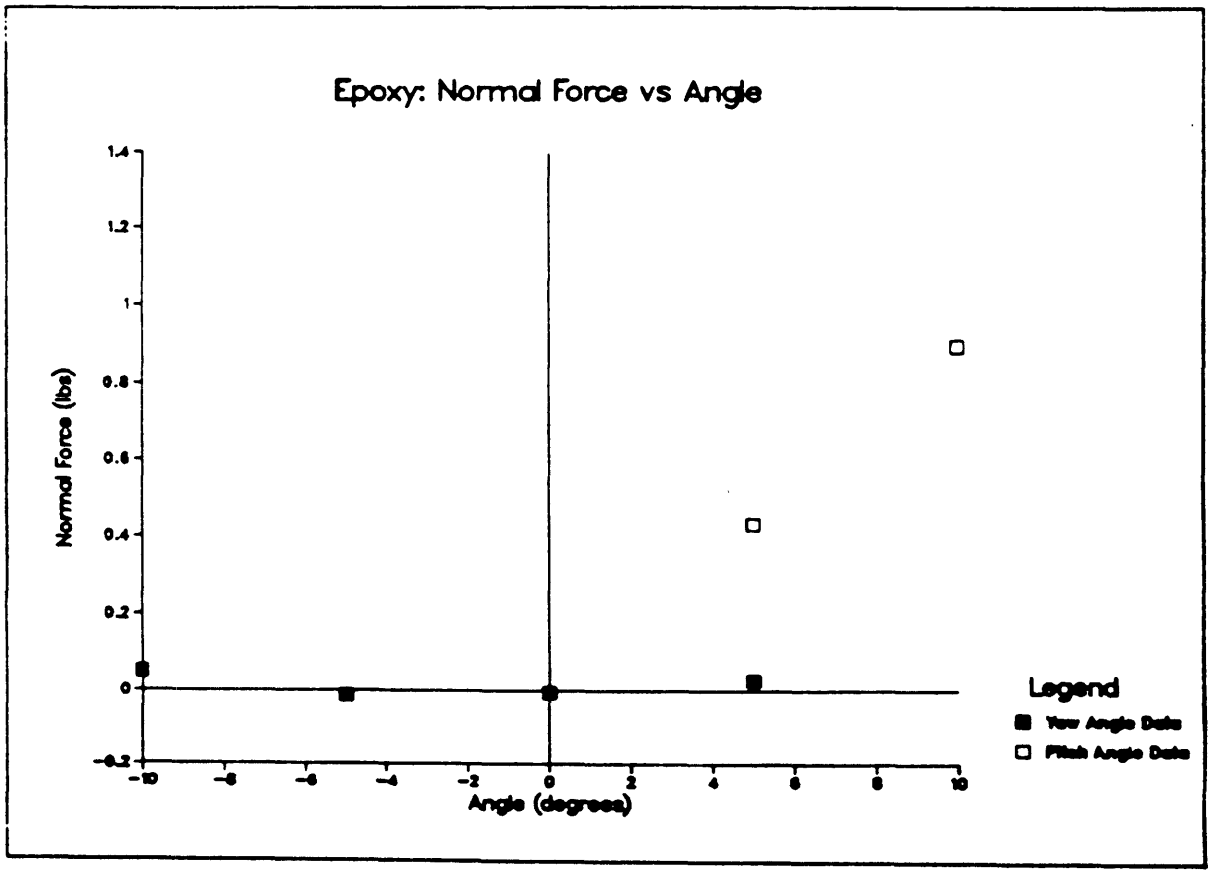

Figure F-5. Epoxy — Normal force versus angle.

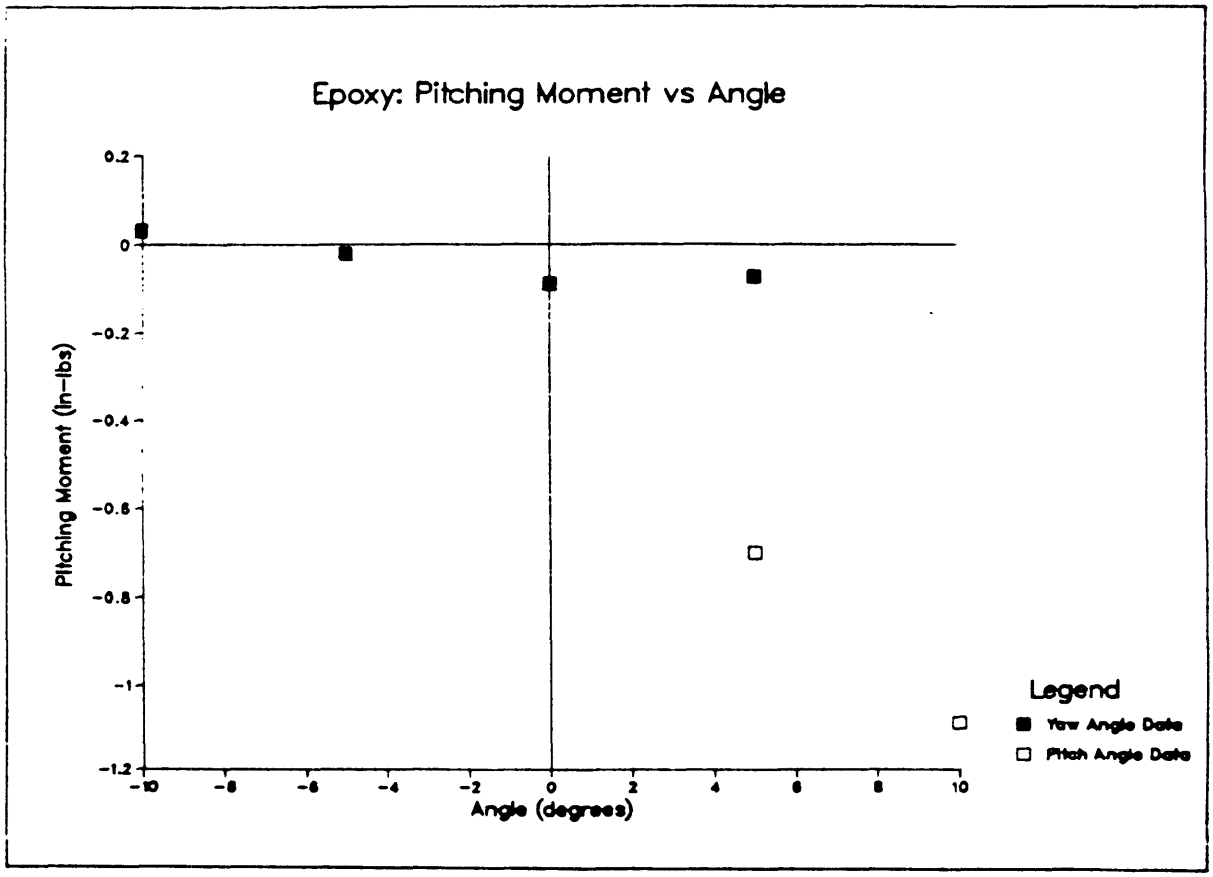

Figure F-6. Epoxy — Pitching moment versus angle.

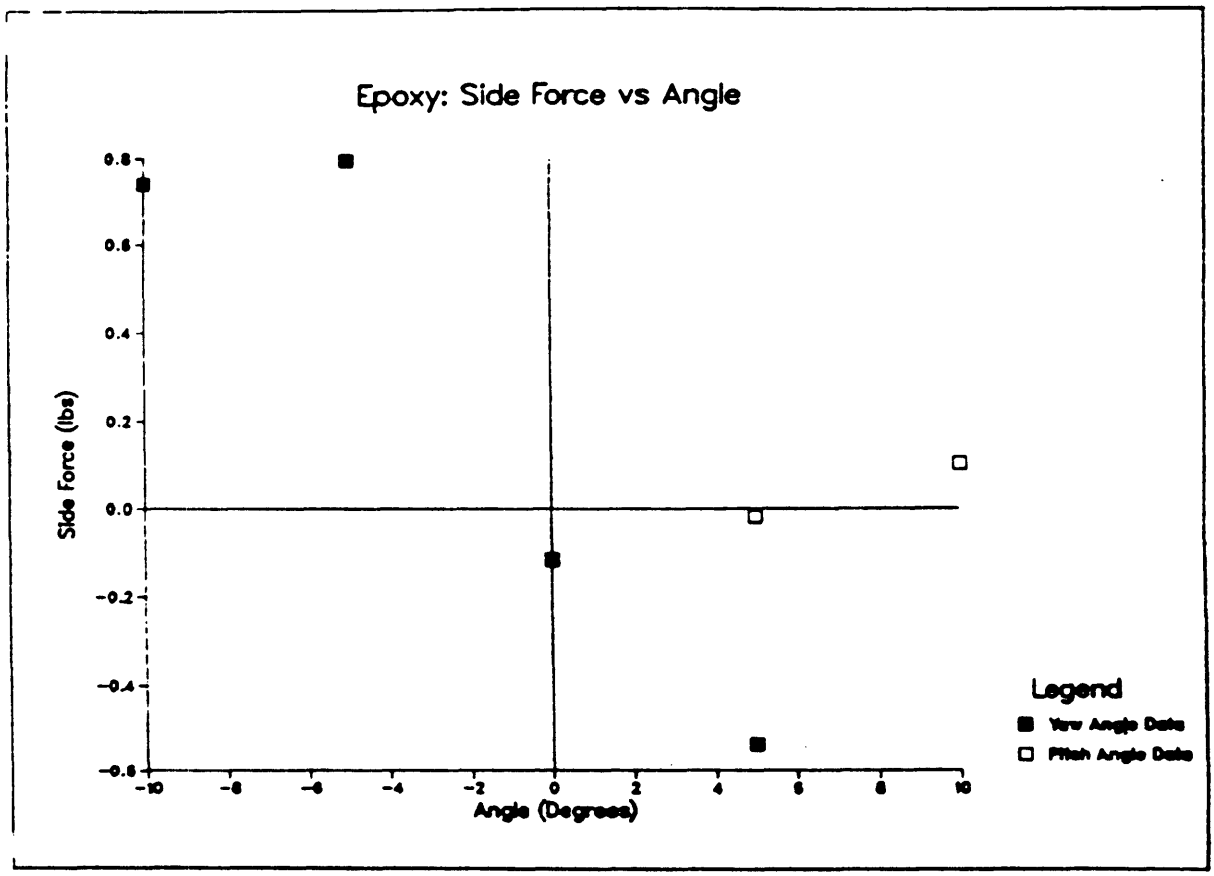

Figure F-7. Epoxy — Side force versus angle.

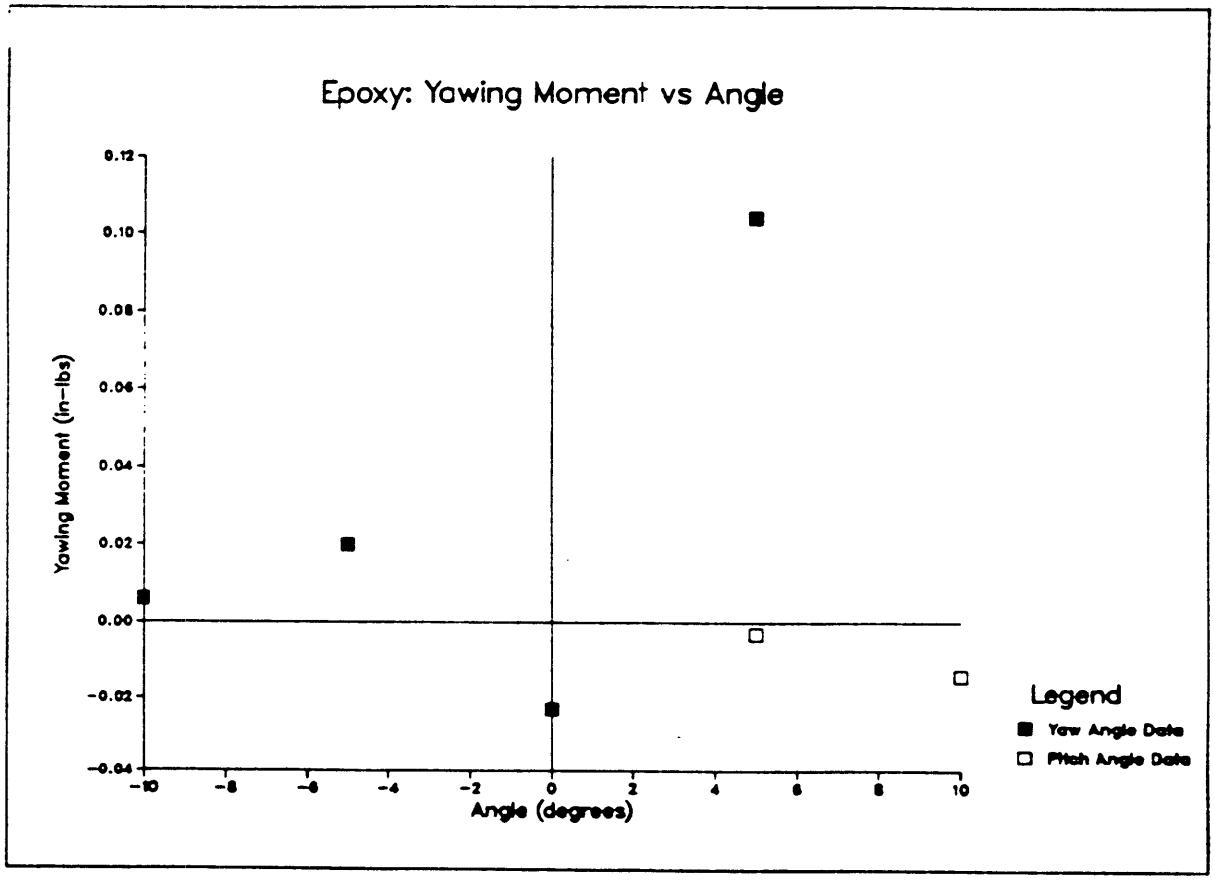

Figure F-8. Epoxy — Yawing moment versus angle.

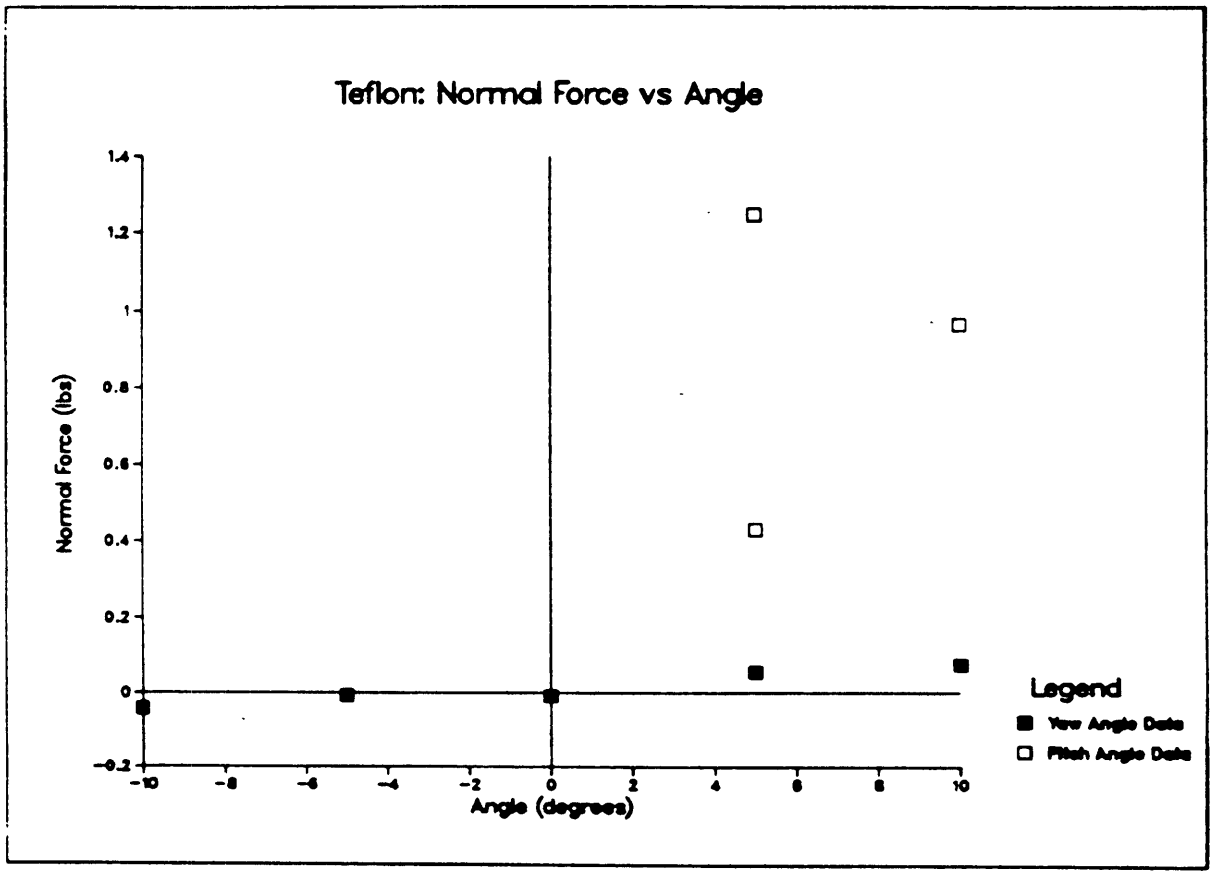

Figure F-9. Teflon — Normal Force versus angle.

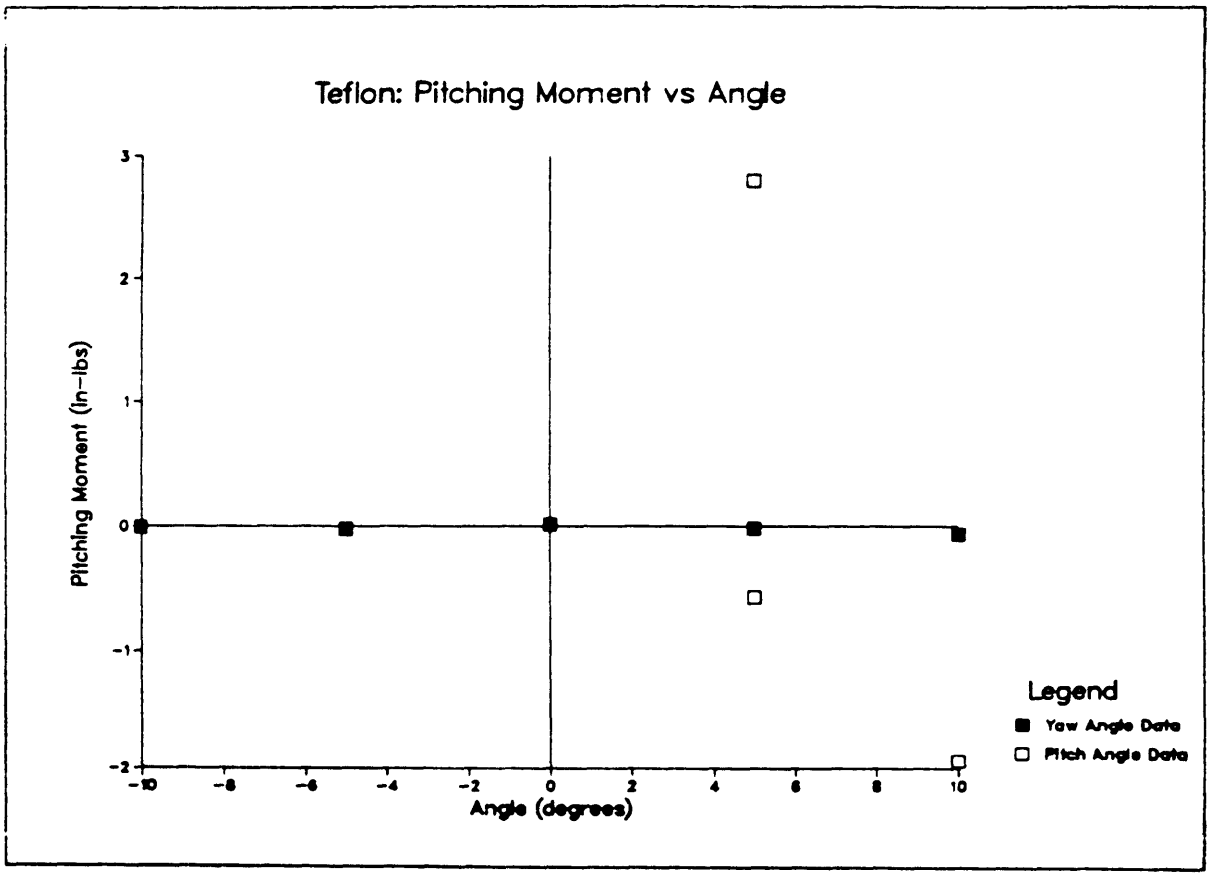

Figure F-10. Teflon — Pitching moment versus angle

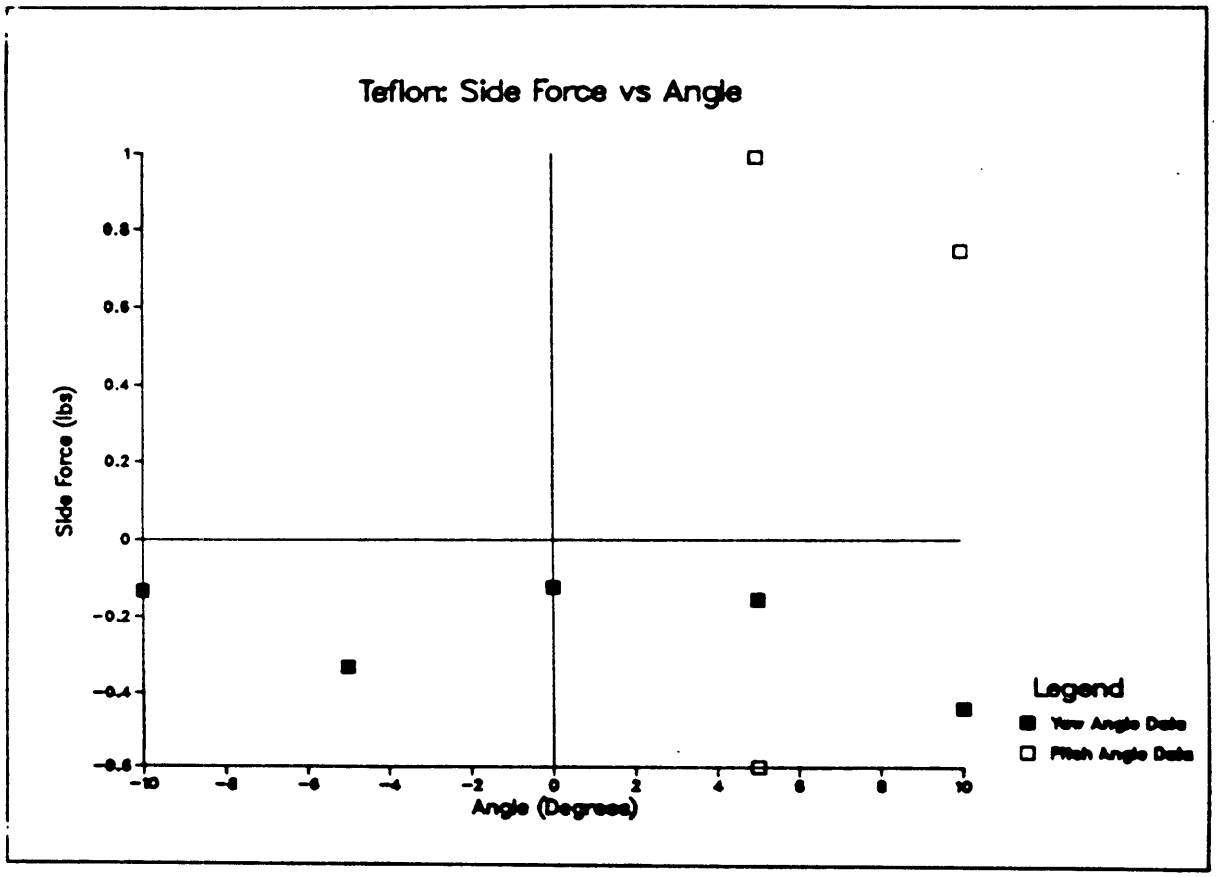

Figure F-11. Tefon — Side Force versus angle.

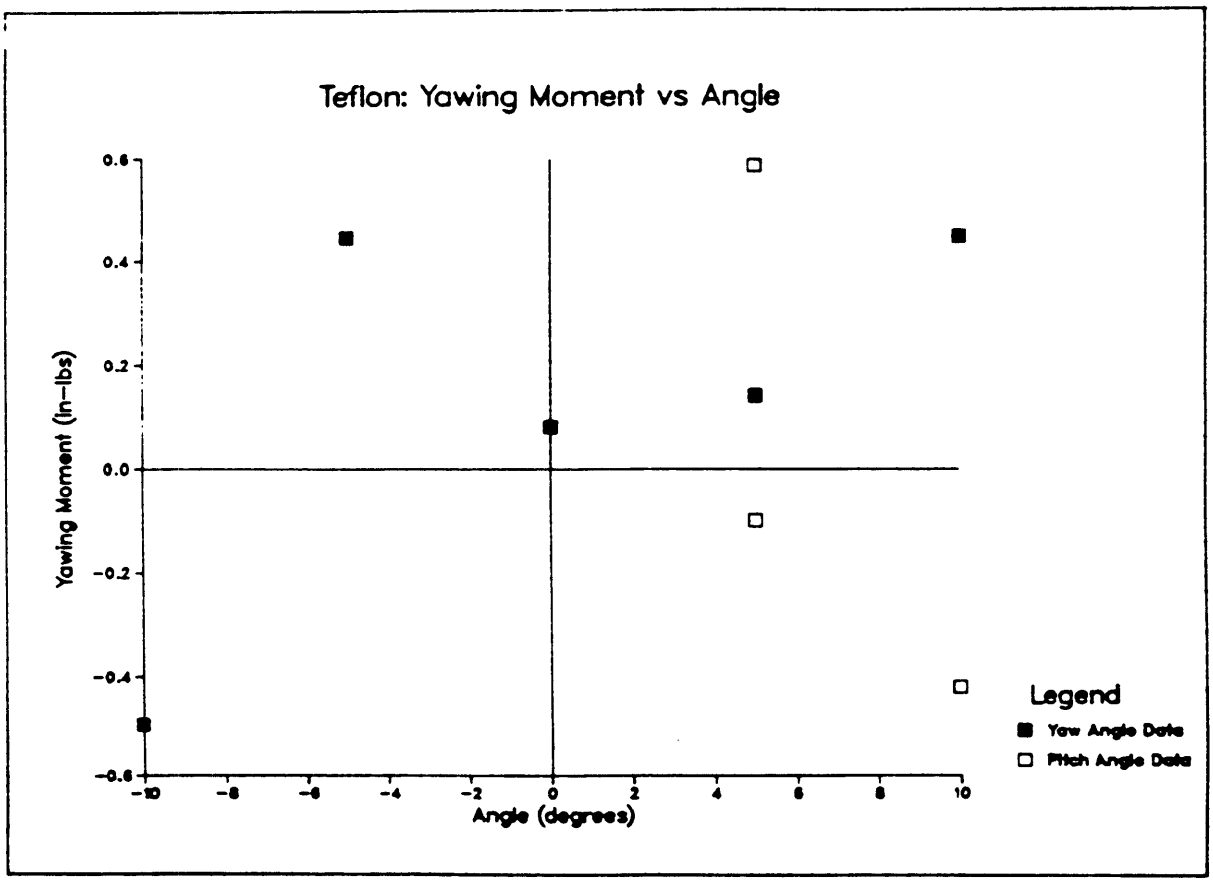

Figure F-12. Teflon — Yawing Moment versus angle.